Master's thesis

NTNU
Norwegian University of Science and Technology
Faculty of Engineering
Department of Mechanical and Industrial Engineering

Karoline Kjøle Olsen

The Influence of Under Ballast Mats on Railway Superstructure

A numerical study of static and dynamic responses

Master's thesis in Materials Science and Engineering
Supervisor: Seyed Mohammad Javad Razavi
Co-supervisor: Albert Lau

June 2022

NTNU
Norwegian University of
Science and Technology

Karoline Kjøle Olsen

The Influence of Under Ballast Mats on Railway Superstructure

A numerical study of static and dynamic responses

Master's thesis in Materials Science and Engineering
Supervisor: Seyed Mohammad Javad Razavi
Co-supervisor: Albert Lau
June 2022

Norwegian University of Science and Technology
Faculty of Engineering
Department of Mechanical and Industrial Engineering

NTNU
Norwegian University of
Science and Technology

Preface

This master's thesis is written in collaboration with Bane NOR and the Norwegian University of Science and Technology (NTNU) at the Department of Mechanical and Industrial Engineering. It is a continuation of the specialization project written in fall 2021 and is the concluding work of my Master of Science at the Department of Materials Science and Engineering.

I want to thank my advisor and co-advisor, Professor Seyed Mohammad Javad Razavi and Professor Albert Lau, for fruitful discussions and encouraging guidance concerning areas of interest in this thesis. Additionally, I would like to thank my advisors from Bane NOR, Céline Chapelier and Alf Helge Løhren, for their commitment to my thesis and for offering guidance related to railway constructions. Lastly, I would like to show my appreciation to friends and family for motivating and supporting me during my work.

Trondheim, June 10, 2022

Karoline Kjøle Olsen

"The most that can be expected from any model is that it can supply a useful approximation to reality: All models are wrong; some models are useful"
– George Edward Pelham Box

Abstract

The growing demand for railway transportation leads to a need for modernization and expansion of existing railway lines. Because the railway is experiencing changes, new trains are also becoming more advanced with higher axle loads and increased speeds. Most railway lines are constructed in tunnels in urban areas for easier passenger access. In such areas, there are strict regulations on emissions of vibrations and noise. A countermeasure to prevent such emissions is incorporating an additional elastic component in the railway track, namely the under ballast mat (UBM). Insertion of soft UBMs is desirable to mitigate ground-borne noise and vibrations. However, little attention is given on how ballast mats affect the overall response of the track construction.

Two numerical 3D models with different designs are modeled to evaluate which is the most optimal and efficient for performing static and dynamic analyses. A mesh convergence study is conducted to optimize the models. In addition, the CPU time required for each model is documented to observe their efficiency. The selected 3D model is then calibrated against a 2D model, which is based on the Zimmermann method, and validated with modal analysis. The model is further used as a benchmark to compare the static and dynamic responses when elastic parameters are varied and when ballast mats are included in the track construction. At the same time, the model is analyzed with different loading conditions; static point load, multiple point loads, and harmonic load for dynamic simulations.

The results showed that the UBMs affect the static and dynamic response of the track. The static analysis shows that the maximum deflection with the softest UBM does not exceed the maximum limit of 3 mm, set by Bane NOR. However, the recommended limit of 2 mm is exceeded by all UBMs. The UBMs also tend to increase the stress distribution in the ballast layer with decreasing stiffness. Changing the thickness of the ballast has a minor effect on the static and dynamic behavior of a railway track compared to varying the stiffness of the rail pad and the UBM. The effect of spacing between axles is also considered in the 3D model by simulating multiple axle loads from a Stadler FLIRT 75 train. This loading condition showed that adjacent axles do influence each other and increase the deflection of the rail even more than with individual point loads. The receptance curves obtained from the steady-state dynamic analysis show that the deflection increases, and the resonance frequencies are shifted towards lower frequencies with decreasing stiffness of the UBM. The receptance curves also show that the UBMs are more efficient below 200 Hz, which is within the range of ground-borne noise and vibrations.

Although the static response does not exceed the maximum deflection of the track, it can be more significant under dynamic loading conditions. For instance, the shifting of resonance frequencies due to the insertion of UBMs can make the railway tracks more susceptible to resonate at specific frequencies, such as the corrugation- and sleeper-passing frequencies. If numerous elastic parameters of a railway track are adjusted simultaneously, it would be necessary to evaluate the total response of the track to avoid the risk of failures.

Sammendrag

Den økende etterspørselen etter jernbanetransport, fører til et behov for modernisering og utvidelse av eksisterende jernbanelinjer. På grunn av at jernbanen opplever store endringer, blir togene også mer avanserte med høyere aksellast og økte hastigheter. De fleste jernbanelinjer bygges i tunneler i urbane områder for enklere tilgang for passasjerer. I slike områder er det også strenge reguleringer om utslipp av vibrasjoner og støy. Et mottiltak for å forhindre slike utslipp er å inkludere en ekstra elastisk komponent i jernbanesporet, nemlig ballastmatter (UBM). Innsetting av myke ballastmatter er ønskelig for å dempe strukturstøy og vibrasjoner. Imidlertid er det lite fokus på hvordan ballastmatter påvirker den generelle responsen til sporkonstruksjonen.

To numeriske 3D-modeller med forskjellige design er modellert for å evaluere hvilken som er mest optimal og effektiv for å utføre statiske og dynamiske analyser. En mesh-konvergensstudie er utført for å optimalisere modellene. I tillegg er CPU-tiden som kreves for simuleringer av hver modell dokumentert for å observere effektiviteten. Den valgte 3D-modellen er deretter kalibrert mot en 2D-modell, som er basert på Zimmermann-metoden, og validert med modal analyse. Modellen er videre brukt som standard for å sammenligne de statiske og dynamiske responsene når elastiske parametere varieres, samt når ballastmatter er inkludert i sporkonstruksjonen. Samtidig er modellen også analysert under ulike belastningsforhold; statisk punktbelastning, flere punktbelastninger og harmonisk belastning for dynamiske simuleringer.

Resultatene viser at ballastmattene påvirker den statiske og dynamiske responsen til sporet. De statiske analysene viser at nedbøyningen med den mykeste ballastmatten ikke overskrider kravet fra Bane NOR om maksimum nedbøyning av sporet på 3 mm. Imidlertid ble den anbefalte grensen på 2 mm overskredet av alle ballastmattene. Samtidig viser ballastmattene en tendens til å øke spenningsfordelingen i ballastlaget med avtagende stivhet. Endring av tykkelsen på ballasten har en mindre effekt på den statiske og dynamiske responsen til det modellerte jernbanesporet, sammenlignet med endring av stivheten til mellomlegget og ballastmattene. Påvirkningen av avstanden mellom aksler er også vurdert i 3D-modellen ved å simulere flere aksellaster fra et Stadler FLIRT 75-tog, noe som ytterligere øker nedbøyningen av skinnen. Reseptanskurvene fra de dynamiske analysene viser at nedbøyningen øker og resonansfrekvensene forskyves mot lavere frekvenser med avtagende stivhet av ballastmattene. Kurvene viser også at ballastmattene er mer effektive under 200 Hz, som er innenfor spekteret av strukturstøy og vibrasjoner.

Selv om den statiske responsen ikke overskrider sporets maksimale nedbøyning, kan den være mer betydelig under dynamiske belastningsforhold. For eksempel kan forskyvningen av resonansfrekvenser på grunn av ballastmattene gjøre sporet mer eksponert for resonans ved spesifikke frekvenser, slik som passeringsfrekvensen over korrugeringer og sviller. Dersom flere elastiske parametere for et jernbanespor justeres samtidig, vil det være nødvendig å evaluere den totale responsen til sporet for å unngå risiko for feil.

Contents

Preface **i**

Abstract **iii**

Contents **v**

List of Figures **viii**

List of Tables **xiv**

Nomenclature **xvii**

1 Introduction **1**
- 1.1 Background 1
- 1.2 Research Aim 3
- 1.3 Research Objectives 3
- 1.4 Structure 3

2 Track Structure **5**
- 2.1 Rail 5
- 2.2 Rail Pad 6
- 2.3 Fastening System and Sleeper 7
- 2.4 Ballast 9
- 2.5 Under Ballast Mat (UBM) 9

3 Track Forces and Design Concepts **11**
- 3.1 Track Stiffness 11
- 3.2 Static Track Design 12

3.3 Dynamic Track Design 15
3.3.1 Receptance 15
3.3.2 Resonance 17
3.3.3 Damping 18
3.4 Track Loads and Stresses 19
3.4.1 Stadler FLIRT 75 21

4 Numerical Modelling in Abaqus 23
4.1 Modules 23
4.2 Elements 24
4.3 Analysis type 25
4.3.1 Static Analysis 25
4.3.2 Natural Frequency Extraction 26
4.3.3 Steady-State Dynamic Analysis 26

5 Numerical Procedure 27
5.1 Assumptions and Track Design 28
5.2 Mesh Convergence Study 31
5.2.1 Study of 3D Beam Model 32
5.2.2 Study of 3D Solid Model 35
5.3 Calibration and Validation 38
5.3.1 Calibration of 2D Model against the Zimmerman Method 38
5.3.2 Calibration of 3D Beam Model against the 2D model 43
5.3.3 Validation of 3D Beam Model based on Modal Analysis 46
5.3.4 Comparison of 3D Models 48
5.4 Properties of UBMs 50

6 Results and Discussion 53
6.1 Beam on Discrete Support Model 53
6.1.1 Effect of Ballast Thickness 53
6.1.2 Effect of Rail Pad Stiffness 55
6.2 Beam on Discrete Support including UBM 57
6.2.1 Static Analysis 57
6.2.2 Dynamic Analysis 61
6.3 Further Discussion of Study Cases 63
6.3.1 Uncertainty of Numerical Modeling Procedure 64

7 Concluding Remarks and Future Research 67
7.1 Concluding Remarks 67
7.2 Future Research 68

Bibliography 71

Appendix I

A Stadler FLIRT 75 **I**
A.1 Layout of Stadler FLIRT 75 train I
A.2 Vehicle Dynamics of Stadler FLIRT 75 train III

B Numerical Procedure of 2D Model **V**
B.1 Track Design V
B.2 Mesh Convergence Study V

C Stress Distribution in the Ballast Layer **VII**

D Pressure Distribution in the Ballast Layer **IX**

E Approach in Abaqus **XI**

List of Figures

1.1 Passenger transport by railway in Norway from 2004 to 2019, showing an increase in number of passengers (histogram) and passenger kilometers (solid line) per year. The primary y-axis shows number of passengers in millions, while the secondary y-axis shows passenger kilometers in billions [40]. 1
1.2 Transmission paths of ground-borne vibration and noise. 2
1.3 Change in the number of noise exposed above 38 dB(A) indoors from 2005 to 2019. The vertical axis shows percentage change, while the horizontal axis is divided into transport sector in the order; in total, road, railway and aviation [41]. 2

2.1 Cross section of a ballasted track with its components. 5
2.2 Rail profile 60E1 with standard dimensions, given in mm [31]. 6
2.3 An overhead profile of a Pandrol 10 mm rail pad with standard dimensions, given in mm [35]. 7
2.4 Pandrol FE 1404 Fastclip with standard dimensions, given in mm [35]. . . 8
2.5 JBV 60 sleeper with standard dimensions, given in mm [35]. 8
2.6 Ballastprofile placed on a hard surface, such as in tunnels, with standard dimensions given in mm [32]. 9
2.7 Application of under ballast mat (UBM) in tunnel. UBM is illustrated as the shaded bottom area [34]. 10

3.1 Setup and equipment for hammer impact test on a railway track [37]. . . . 12
3.2 Continuously supported Euler-Bernoulli beam with Winklers elastic foundation according to the Zimmermann method [17]. 13
3.3 Modulus of receptance function of one degree of freedom system [14]. . . 16

3.4 Typical track receptance of model with discrete supports and sinusoidally varying force [10]. 17
3.5 Stress distribution through track structure from single wheel load [22] . . 20
3.6 Illustration of the Stadler FLIRT 75 train [12]. 21

4.1 Commonly used element families [44]. 24
4.2 Solid continuum element types. 25

5.1 Flowchart of the numerical procedure. 27
5.2 3D model created in Abaqus of a ballasted track with discrete support. . . 28
5.3 I-shaped profile available in Abaqus. 29
5.4 Comparison of the different rail profiles between the 3D models. 29
5.5 Comparison of rail pad profiles from the two 3D models. 30
5.6 Profile of modeled sleeper in Abaqus. 30
5.7 Modeled ballast and UBM connected together in Abaqus. 30
5.8 Boundary conditions applied to the 3D models with and without UBM. . 31
5.9 Mesh convergence of rail with B31 linear beam elements. 32
5.10 Mesh of sleeper with decreasing element size in a vertical and horizontal direction towards connection point of rail pad. 33
5.11 Comparison between mesh convergence of sleeper with C3D8I and C3D8 elements, and measured CPU time with increasing number of elements. The black curves indicate deflection of the sleeper with C3D8 (solid line) and C3D8I (dashed line) elements. The red lines indicate measured CPU time for sleeper with C3D8 (solid line) and C3D8I (dashed line) elements 34
5.12 Comparison between mesh convergence of ballast with C3D8R and C3D8 elements, and measured CPU time with increasing number of elements. The black curves indicate deflection of the ballast with C3D8 (solid line) and C3D8R (dashed line) elements. The red lines indicate measured CPU time for ballast with C3D8 (solid line) and C3D8R (dashed line) elements 34
5.13 Mesh convergence study of rail from 3D solid model, including measured CPU time against number of elements. 36
5.14 Mesh convergence study of sleeper from 3D solid model, including measured CPU time against number of elements. 36
5.15 Mesh convergence study of ballast from 3D solid model, including measured CPU time against number of elements. 37
5.16 2D model 38
5.17 Deflection and moment distribution along an assumed 20 meter long rail, according to Zimmermann method from Section 3.2. 39
5.18 Literature research of (a) Young's modulus and (b) Poisson's ratio performed by Rodrigues [36]. 40
5.19 Comparison of rail deflection between results from 2D model and the Zimmermann method. 41
5.20 Comparison of moment distribution between results from 2D model and the Zimmermann method. 41
5.21 Damping of ballast found from Rayleigh definition and damping of rail pad equal to 5E3 42

5.22 Receptance curve of the 2D model with alternated damping properties. . . 43
5.23 Comparison of deflection curves between results from 2D model and 3D model. 44
5.24 Comparison of moment distribution between results from 2D model and 3D model. 44
5.25 Comparison of receptance test between 2D model and 3D model. 45
5.26 Receptance of model without UBM mid-span and above sleeper. 46
5.27 The first modal shape showing the resonance where rails and sleepers bounce on top of the ballast, it is found at a frequency of 135.1 Hz. . . . 47
5.28 The second modal shape showing the resonance where rails vibrates on the rail pads, it is found at a frequency of 212.3 Hz. 47
5.29 The third modal shape showing the pin-pin resonance where the rails bend between the sleepers, is found at a frequency of 1058.2 Hz. 47
5.30 Comparison between deflection curve of 3D solid model and 3D beam model 48
5.31 Comparison between receptance curve of 3D solid model and 3D beam model 49
5.32 Stress versus strain curve for UBMs 50

6.1 Change of ballast thickness from 40 cm to 50 cm and 60 cm. 53
6.2 Deflection curves from changing the ballast thickness from 40 cm to 50 and 60 cm, with a point load of 110.4 kN. 54
6.3 Receptance curves obtained with different thicknesses of the ballast layer. 55
6.4 Deflection curves from changing the rail pad stiffness to 31 MN/m and 70 MN/m. 55
6.5 Receptance curves obtained with different stiffnesses of rail pad. 56
6.6 Cross section of the 3D model, including UBM6, from Abaqus. 57
6.7 Deflection curves from static analysis with all UBMs ranging from stiff (UBM1) to soft (UBM6), loaded with a static point load corresponding to the maximum axle load exerted by a Stadler FLIRT 75 train of 110.4 kN. 57
6.8 Critical part of FLIRT 75 train with highlighted axle loads and distances between wheels. Bogie MB4 is shown on the left hand side, while TB3 is shown on the right hand side. 58
6.9 Deflection curve with multiple loads from bogie MB4 and TB3 of a Stadler FLIRT 75 train, including all UBMs ranging from stiff (UBM1) to soft (UBM6) 59
6.10 Deflection curves of rail with UBM6. Dashed lines indicate a single point load from either bogie MB4 or TB3, while the red solid line is the total deflection when both bogies are loaded on the track. 60
6.11 Vertical stress distribution in the ballast layer. The measured stress are presented in Pascal, [Pa]. 61
6.12 Measured receptance curves of all UBMs ranging from stiff (UBM1) to soft (UBM6), loaded with a harmonic sinusoidal load with a circular frequency of 2π. 62

B.1 Profile of 2D model V

B.2 Mesh convergence study of rail from 2D model with B21 Timoshenko elements. The B21 elements is chosen due to allowable shear deformation of the beam. . . . VI
B.3 Mesh convergence study of sleeper from 2D model with CPS4I and CPS4 elements. . . . VI
B.4 Mesh convergence study of ballast from 2D model with CPS4, CPS4I and CPS4R elements. . . . VI

C.1 Stress distribution of the ballast layer without UBM. The dark blue areas show the highest measured compressive stress (located beneath a sleeper), while the highest measured tensile stress is presented in red areas (between sleepers and further away from the applied load). . . . VII
C.2 Stress distribution of the ballast layer with UBM1. . . . VII
C.3 Stress distribution of the ballast layer with UBM5. . . . VII
C.4 Stress distribution of the ballast layer with UBM6. . . . VII

D.1 Pressure distribution of the ballast layer without UBM. The red areas show the highest measured pressure (located beneath a sleeper), while the lowest measured pressure is presented in blue areas (between sleepers and further away from the applied load). . . . IX
D.2 Pressure distribution of the ballast layer with UBM1 . . . IX
D.3 Pressure distribution of the ballast layer with UBM5 . . . IX
D.4 Pressure distribution of the ballast layer with UBM6 . . . IX

E.1 Creating Part by choosing modeling space, type of part and shape. Parts can be created through extrusion, revolution or by sweep. Base extrusion is the most common type of base feature, in which you choose the depth of the part. . . . XI
E.2 Once a part is created, it is assigned material properties. Abaqus offers a variety of properties to define the behavior of the part. . . . XI
E.3 If a wire or shell feature is created, it can be assigned a profile in Abaqus. There are various profiles available, such as the I-profile. . . . XII
E.4 In the property module, a section is assigned to the part. It is possible to choose the type of section a part should have based on the available categories. In this module, the a profile and material properties can be assigned to the part. . . . XII
E.5 Various part can be created and assembled as instances in the assembly module. The same part can also be multiplied in this module. After assembly, it is possible to assign various interaction properties between each instance in the assembly in the interaction module. . . . XIII
E.6 Abaqus also offers to create springs and dashpots between instances in the assembly. This is done by connecting nodes from each part, and later choose the properties of the spring and dashpot. . . . XIII

E.7 A step must be created in Abaqus to run various analyses. The step can further be edited by choosing time period and incrementation. This is also where the NGLEOM can be turned on or off based on nonlinear or linear analyses, respectively. XIV
E.8 Abaqus offers various types of loading conditions, which is assigned to the created step. The load can be edited by choosing a custom amplitude and the magnitude of the load. XIV
E.9 The instances in the assembly can be assigned boundary conditions, which can also vary depending on the selected step. Abaqus offers different categories and types with specified directions. XV
E.10 The whole assembly must be meshed before running the analyses, which is done in the mesh module. Global or local seeds can be assigned to each instance, and the element type is chosen based on the family. It can further by specified to have hexahedral, tetrahedral or wedge shaped elements. . . XV

List of Tables

3.1 Proposed foundation modulus based on track quality [15]. 14

5.1 Input parameters for I-profile in Abaqus 29
5.2 Input parameters for calculations of the Zimmermann method. 39
5.3 Output parameters from the Zimmermann method. 39
5.4 Properties used for calibrating railpad stiffness. The properties of 60E1 rail are kept constant for all simulations. 40
5.5 Properties found and used for modeling a rail on discrete support in 3D beam model. 45
5.6 Frequency range of natural frequency extraction. 47
5.7 Number of elements meshed on each part in the 3D beam model and 3D solid model, including total number of elements in the whole model considering 2 rails, 128 rail pads and 64 sleepers. 49
5.8 Average CPU time, presented in seconds, for each analysis completed for 3D beam model and 3D solid model. 49
5.9 Secant modulus of measured stress-strain curves for different UBMs, including the input parameters, density and thickness, in Abaqus. 51

6.1 The resonance frequencies derived from the various receptance curves for each UBM. 62

Nomenclature

Abbreviations

BOEF	Beam on elastic foundation
CPU	Central processing unit
CWR	Continuously welded rails
Dof	Degrees of freedom
FEA	Finite Element Analysis
FEM	Finite Element Method
FP	Flat plate
GBP	Geometric ballast plate
NLGEOM	Non-linear geometry
UBM	Under ballast mat

Symbols

α	Mass proportional damping
β	Stiffness proportional damping
η	Loss factor

λ	Corrugation wavelength
ν	Poisson's ratio
ω	Radial vibration frequency
ω_e	Eigenfrequency
ρ	Mass density
ζ	Damping ratio
A	Area of sleeper
a	Sleeper spacing
b	Width of fictive sleeper
b_1	Width of sleeper
C	Ballast modulus
c	Viscous damping
E	Young's modulus
EI	Bending stiffness
F	Force
f	Vibration frequency
h	Height
I	Inertia of rail
L	Characteristic length
l	Length of sleeper
M	Bending moment
p	Ballast pressure
Q or q	Load
y	Deflection

1

Introduction

1.1 Background

The Norwegian Railway Administration is facing both expansions and modernization of the railway due to increased demand, as seen in Fig. 1.1. New lines will be developed with more tunnels and bridges to ensure accessibility and passenger growth. In parallel with an increased number of train lines, there must be an increase in capacity for both passenger and freight trains. This development creates a growing need for new trains that are both more sustainable and comfortable. However, modern trains introduce higher axle loads and speed, which gives rise to other important aspects of the railway traffic's impact on the surrounding environment.

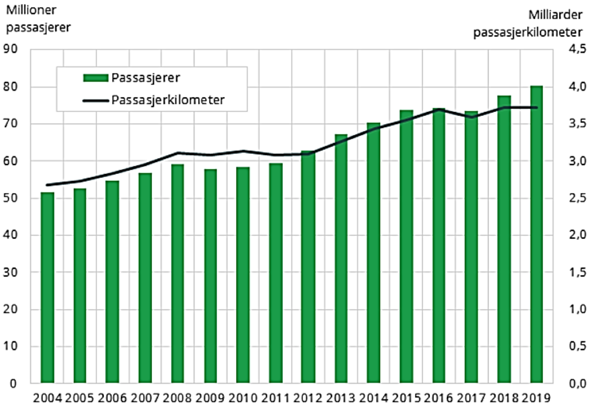

Fig. 1.1: Passenger transport by railway in Norway from 2004 to 2019, showing an increase in number of passengers (histogram) and passenger kilometers (solid line) per year. The primary y-axis shows number of passengers in millions, while the secondary y-axis shows passenger kilometers in billions [40].

One particular and important concern is the comprising noise and vibrations induced by the passage of trains. The vibration is often generated by the contact between the train wheel and the railway track, and is transferred through the super- and substructure. These vibrations then travels from the track, through the ground and into the surrounding environment, as illustrated in Fig. 1.2. Generally, the strength of these vibrations decreases away from the track, but they can also increase due to resonances. This can cause discomfort and annoyance to inhabitants or affect surrounding buildings. These effects are also more prone to occur for railway traffic in tunnel lines, were the noise and vibration can reach buildings when the tunnel alignment is directly below buildings [42].

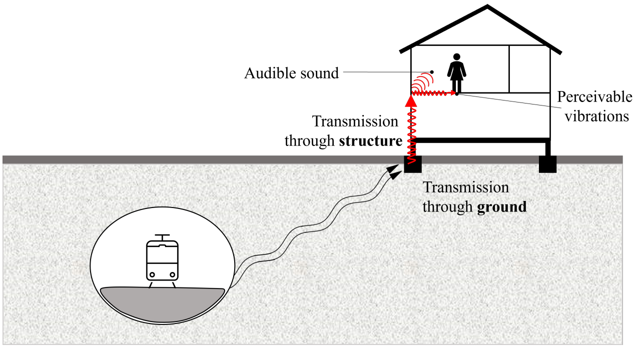
Audible sound
Perceivable vibrations
Transmission through **structure**
Transmission through **ground**

Fig. 1.2: Transmission paths of ground-borne vibration and noise.

A survey on noise exposure conducted by SSB [41] is presented in Fig. 1.3, and indicates a 42% increase in the number of persons experiencing noise above 38 dB(A) indoors from railway traffic. In order to meet the requirements set by national standards, such as NS 8175 and NS 8176 [8] with limitations set to 32 dB in tunnels, countermeasures to mitigate these emissions needs to be made. A proposed solution to reduce these emissions, is to incorporate additional elastic components into the track design, such as the under ballast mat (UBM).

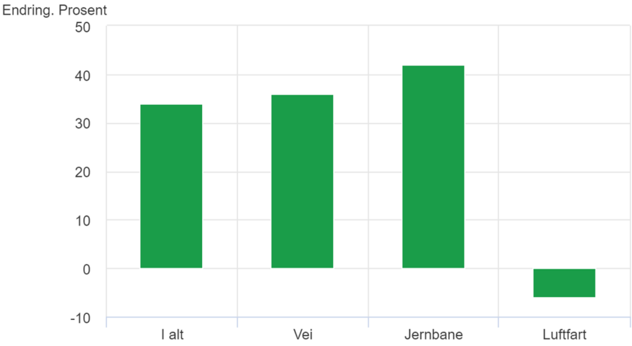

Fig. 1.3: Change in the number of noise exposed above 38 dB(A) indoors from 2005 to 2019. The vertical axis shows percentage change, while the horizontal axis is divided into transport sector in the order; in total, road, railway and aviation [41].

There are specific regulations regarding the properties of UBMs, which have to be considered while designing tracks in order to mitigate ground-borne vibration and noise, and to define a good quality track [33]. An essential property of the UBM is its stiffness. Research has been conducted to find the efficiency of using UBMs with varying stiffness to attenuate vibrations and noise, and to prevent degradation of ballast. Alves Costa et al. [7] found in their study that the mitigation of vibrations induced by railway traffic is dependent on the stiffness of the UBM, and that softer UBMs are required to obtain a reduction of vibrations. However, less attention has been given to the static and dynamic response of the vehicle-track-ground interactions with decreasing vertical track stiffness.

1.2 Research Aim

The static and dynamic responses of a ballasted railway track with UBMs has not been widely reported. Thus, the aim of this thesis is to gain an understanding of how the track respond to including an additional elastic component in the track structure, namely the UBM. Other elastic components of the track are also investigated to assess their effect on the overall static and dynamic track response, by altering their material properties. The static response of the track is investigated to ascertain if the rail deflection exceeds the limits set by Bane NOR, both with a concentrated point load and multiple wheel loads, while including UBM in the track. Additionally, the dynamic response of the track is analysed to observe how the UBMs can affect the resonance of the track structure. These resonances can coincide with known frequency ranges, and can potentially contribute to failure.

1.3 Research Objectives

It has been proposed in collaboration with Bane NOR to establish a numerical model to simulate the effects of introducing an additional elastic component in the track structure, the UBM. A proposed analytical solution is used as benchmark to develop advanced numerical models to analyse the response of the track. For this purpose, a finite element analysis (FEA) tool called Abaqus, is utilized to create two-dimensional (2D) models or complex three-dimensional (3D) models. A 2D model is created for calibration of two 3D models. The two 3D models are created to find the optimum track design for running efficient and predictable simulations. The chosen track design is further used to analyse the static and dynamic response when parameters of elastic components in the track is altered. The results will be compared to the validated 3D model. The static and dynamic responses will be provided in the form of deflection curves and receptance curves, respectively.

1.4 Structure

The following chapters are included in this thesis:

Chapter 1 - *Introduction*: Includes background regarding the research aim and research objectives.

Chapter 2 - *Track Structure*: Introduces specific railway terms and concepts, and explains the use and purpose of various track components.

Chapter 3 - *Track Forces and Design Concepts*: Explains important aspects influencing static and dynamic railway track design, including loading conditions of the track.

Chapter 4 - *Numerical Modelling in Abaqus*: Presents a brief overview of important concepts and functions offered in Abaqus.

Chapter 5 - *Numerical Procedure*: Concerns the modeling procedures of the 3D models in Abaqus. It includes track design of the analysed models, mesh convergence studies, and calibration and validation of the models based on analytical theory and a simplistic 2D model. A comparison of the two 3D models is also conducted to evaluate optimum and efficient design for subsequent simulations.

Chapter 6 - *Results and Discussion*: Presents the static and dynamic results obtained from the selected 3D model and discussions of the study cases, including uncertainties of the numerical modeling procedures.

Chapter 7 - *Concluding Remarks and Future Research*: Conclusions of obtained results and usability of the applied method is presented. Suggestions for future research is also presented.

2

Track Structure

This chapter addresses the different components of a track structure and introduces specific railway terms and concepts. Parts of the theory presented in this chapter is based on findings from Project Thesis, fall 2021. Track components are divided into the substructure, and superstructure [17]. There are different track configurations, and the most common is a ballasted railway track. For the scope of this thesis, the superstructure of a ballasted railway track with components related to the Norwegian standards is of interest. The components are rail, rail pads, fastening system, sleepers, ballast, and under ballast mat (UBM), shown in Fig. 2.1. These components are the main load-supporting elements of the track that react and transfer loads to the substructure [21].

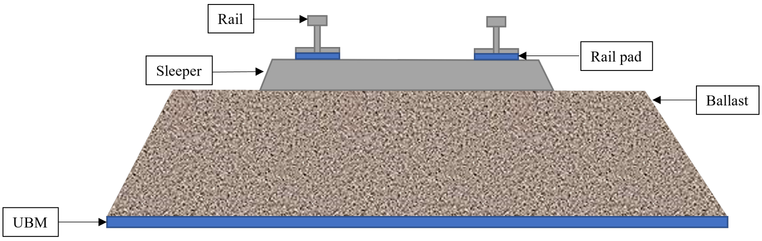

Fig. 2.1: Cross section of a ballasted track with its components.

2.1 Rail

For many years the standard railway construction practice was jointed rails until the introduction of continuously welded rails (CWR), the most common rail type on main lines today [21]. The benefit of CWR is the elimination of discontinuities generated from the joints, which lowers maintenance and costs. Over the years, the rail profile has also changed from smaller to larger cross-sections to withstand wear [21]. The rails are often high-strength steel and undergo head hardening to enhance durability and strength. The purpose of the rails is to transfer static and dynamic loads from the vehicle to the super-

and substructure and to steer the vehicle [17]. It is essential to have a smooth running surface to avoid corrugations on the rail, leading to degradation of the track structure [15]. The rail profile design varies with the superstructure class, and the rail profile of interest is called 60E1. The first number of rail profile 60E1 indicates the weight of the rail measured in kg/m, while E means that the profile name is made according to the European standard [31]. The rail profile is depicted in Fig. 2.2, and it has a flat bottom with a big railhead. When designing a track, it is important to consider the type of rail profile regarding speed, axle load, and sleeper spacing due to traffic load and desired lifetime of the rails [17].

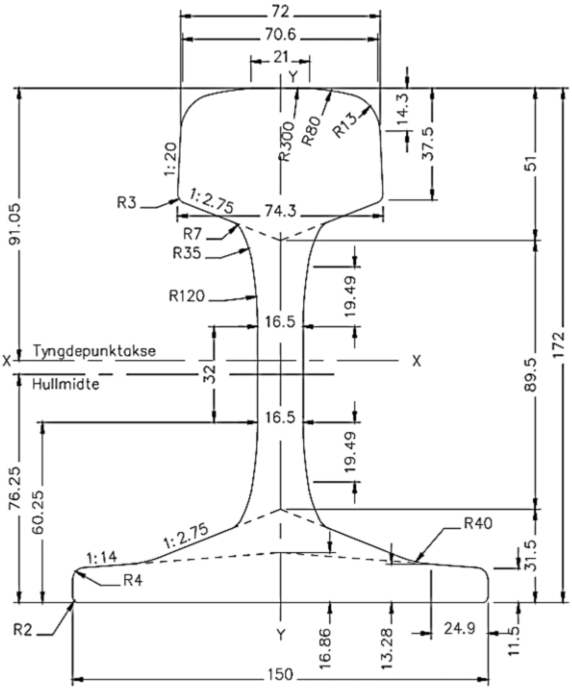
72
70.6
21
Y
R300
R80
R13
14.3
37.5
51
1:20
R3
1:2.75
74.3
R7
R35
R120
19.49
16.5
91.05
X
Tyngdepunktakse
Hullmidte
32
X
172
89.5
16.5
19.49
76.25
60.25
1:2.75
R40
1:14
R4
31.5
R2
Y
16.86
13.28
24.9
11.5
150

Fig. 2.2: Rail profile 60E1 with standard dimensions, given in mm [31].

2.2 Rail Pad

A rail pad is a conforming element of either plastic or rubber placed between the steel rail, and the concrete surface of the sleeper [17]. There are two types of classifications of rail pads; inelastic and elastic rail pads. The inelastic rail pads are produced of plastic material and dampen vibrations to some extent. In contrast, the elastic rail pads are made of rubber which dampens vibrations well and provides increased friction between sleeper and rail [35]. Thus, the type of rail pad varies with the design of the track, especially regarding the sleeper and rail type. The stiffness of the rail pad should be as low as possible and is determined due to wear and fatigue, dynamic gauge widening, and noise emissions [17].

Additionally, an important property of the rail pad is to transfer loads to the sleeper and filter out the high-frequency forces. The rail pad of interest is the most common in Norway, which is the studded Pandrol 10 mm shown in Fig. 2.3 [35].

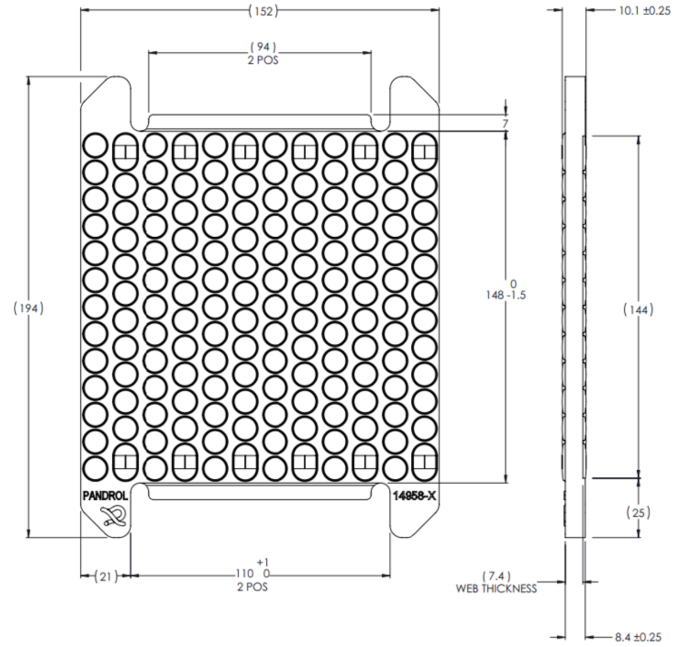

Fig. 2.3: An overhead profile of a Pandrol 10 mm rail pad with standard dimensions, given in mm [35].

2.3 Fastening System and Sleeper

The fastening system includes all the components which form the structural connection between the rail and sleeper [15]. The function of the fastening system is to keep the rail in place by restraining lateral, longitudinal, and vertical relative movement between the rail and sleeper. This function entails attenuation and dampening of vibrations caused by traffic, elastically absorption of rail forces, and transfer of these forces to the sleepers [17]. The fastening system affects the track's behavior and depends significantly on the type of sleepers used in the track design. Fasteners can be categorized into direct or indirect fastenings. Direct fastenings entail that the rail and the baseplate are fixed to the sleeper using the same fasteners [15]. A base plate is placed between the sleeper and rail to distribute the vertical load to a larger area and reduce the vehicle's overturning moment [15]. Indirect fastenings entail that the rail is connected to an intermediate component by other fasteners than those used to fix the intermediate component to the sleeper [15]. A typical direct fastener is shown in Fig. 2.4 and is called Pandrol FE 1404 Fastclip [35]. This type of fastener is often combined with concrete sleepers.

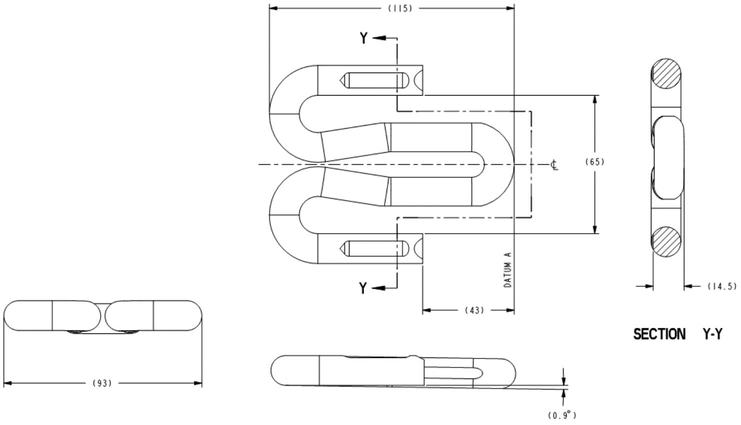
(115)
Y
Y
(65)
℄
DATUM A
(43)
(14.5)
SECTION Y-Y
(93)
(0.9°)

Fig. 2.4: Pandrol FE 1404 Fastclip with standard dimensions, given in mm [35].

The sleeper is placed between the rail and ballast in a ballasted track to establish track gauge and alignment. Its function is to distribute and transfer loads from the rails to the ballast bed, secure the track, and dampen rail vibrations [17]. There are different sleepers, and the most common types are wooden and prestressed concrete sleepers. Specifications for sleepers depend mainly on the dimensional accuracy and resistance to weathering, and low maintenance costs [15]. The sleeper of interest is a JBV 60 concrete sleeper, shown in Fig. 2.5, which is a prestressed concrete monoblock and is widely used in Norway [35]. The advantages of this type of sleeper are its long lifetime, easy surface for maintenance, and how it distributes the loads. It has a greater weight than other sleepers, resulting in enhanced track stability. This type of sleeper also requires elastic fasteners since it is more prone to damage from impacts due to its high stiffness [17].

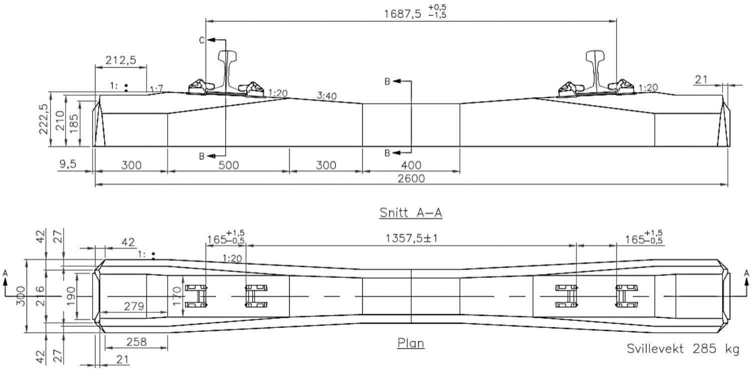
1687,5 +0,5 −1,5
C
212,5
1: :
1:7
1:20
3:40
B
1:20
21
222,5
210
185
B
B
9,5
300
500
300
400
2600
Snitt A–A
42
27
42
165+1,5 −0,5
1357,5±1
165+1,5 −0,5
1: :
1:20
A
A
300
216
190
170
279
258
21
42
27
Plan
Svillevekt 285 kg

Fig. 2.5: JBV 60 sleeper with standard dimensions, given in mm [35].

2.4 Ballast

Ballast consists of coarse-grained material and is placed beneath and around the sleepers. The purpose of the ballast is to distribute stresses, and vertical loads from sleepers to the subgrade [17]. This part of the track structure is also responsible for stabilizing the track by ensuring lateral and longitudinal resistance. The ballast should be well-graded and compact to ensure good track stability. On the other hand, an essential function of the ballast is its ability to facilitate rainwater drainage, which will not be possible if the ballast is too compact [21]. Proper gradation of the ballast layer is also necessary to store fouling material in void spaces. Fouling materials are small particles that accumulate in void spaces within the ballast layer and can originate from abraded or broken ballast [21]. The thickness of the ballast should be based on the structural capacity of the track to withstand and distribute the loads at a stress level that will not deform the subgrade [15]. The ballast design depends on the type of sleeper used, applied axle load, and train speed. If the resistance against plastic deformation and elastic deflection is small and uniform along the track during loading, the ballast support can be categorized as good. Based on requirements set by Bane NOR, the ballast height must be at least 30 cm and should not exceed 70 cm [33]. For this study, the ballast is assumed to be clean and dry with a thickness of 40 cm with uniformly graded rocks having fractions between 31.5 to 63 mm [33]. The ballast profile shown in Fig. 2.6 applies to tracks with speeds up to 200 km/h [33].

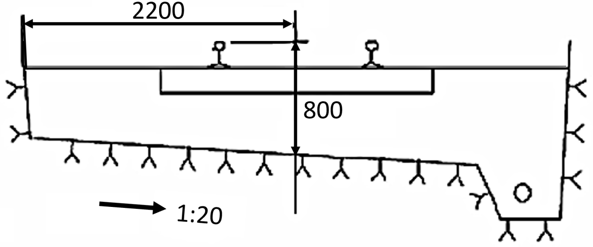

Fig. 2.6: Ballastprofile placed on a hard surface, such as in tunnels, with standard dimensions given in mm [32].

2.5 Under Ballast Mat (UBM)

Under ballast mats (UBMs) are resilient elements incorporated in the track structure to mitigate noise and vibration and to protect track components [17]. UBMs act as protection layers by improving the load distribution in the track structure. They are mainly applied in rocky areas, such as tunnels or bridges, due to the limited thickness and width of the substructure. According to Muller [24], the application area of UBMs has also been proven, through experimental tests, to be more effective if the support is stiffer than in open lines. UBMs are usually 15 to 80 mm thick and are designed with two layers, whereby the top layer consists of a rugged protection layer to prevent penetration of ballast grains and abrasive wear [15]. The elastic layer of the UBM does not necessarily absorb the transferred energy itself but somewhat dampens the motion of the ballast layer. Therefore, the UBM generates a mass-spring effect that transfers energy away from the structure, which will decrease with the stiffness of the UBM [15]. However, decreasing the stiffness of the UBM may cause other issues, such as increased rail deflection and destabilization of the ballast [15]. Therefore, Bane NOR suggests limiting track deflection to less than 2 mm and never exceeding 3 mm [34]. The UBM is placed between the tunnel floor and ballast layer, as shown in Fig. 2.7.

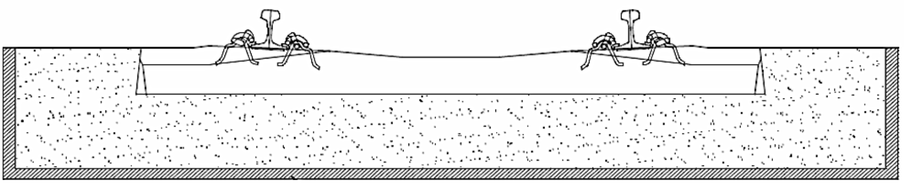

Fig. 2.7: Application of under ballast mat (UBM) in tunnel. UBM is illustrated as the shaded bottom area [34].

3

Track Forces and Design Concepts

The subject of this chapter is how design concepts are essential for the analysis of the track components and how track forces affect their response. An important parameter regarding track design is the track stiffness, which is fundamental in static and dynamic design. Parts of the theory presented in this chapter is based on findings from Project Thesis, fall 2021.

3.1 Track Stiffness

Track stiffness is a fundamental parameter of track design and is the load required to produce a unit displacement of the rail at the point of loading in the vertical direction. This parameter influences the bearing capacity of the track, static and dynamic behavior, and the quality of track geometry [17]. It is often referred to as global stiffness and depends significantly on the effective stiffness of all components in the structure [13]. The railway track is rarely built on a homogeneous ground, which leads to changes in track stiffness along the track and variations in vehicle-track interaction forces [48].

Vertical track stiffness is the ratio between track load and track deflection. The track load originate from axle loads and it can be analyzed either statically or dynamically. Static stiffness is the resistance against deformation in the track structure, while dynamic stiffness is the resistance against deformations under specific dynamic excitations, which is determined by the natural frequencies of the track [47]. The static stiffness of the track can be found by measuring resulting rail deflections caused by exerted loads of the vehicle. The analysis of dynamic stiffness can be conducted by using Fourier transform and associated transfer functions. The transfer function between force and displacement is called receptance or dynamic flexibility [9]. Receptance is the inverse of the dynamic stiffness and is a complex quantity [9].

Vertical track stiffness can be measured in different ways, but the most important ones are standstill and moving measurements. The standstill measurement is widely used for research purposes, whereas moving measurement is more useful for production measurements [9]. The most common type of standstill measurement is the impact hammer test, which is a handheld device as shown in Fig. 3.1. A force transducer is placed on the hammerhead to measure the excited impulse from hitting the rail [9]. Then the transfer function between the impulse force of the hammer and acceleration of the rail is calculated. This type of test is most suited for noise, vibration, and wheel-rail contact forces problems [9]. The rolling measurement is mainly done by measuring the displacement under one or two axles from the rolling stock. Thus, the track stiffness can be calculated if the static axle load of the rolling stock is known [9]. Track stiffness is also a function of frequency. The static and low-frequency dynamics of the track are related to geotechnical measurements, which are beneficial for analyzing the bearing capacity of the track and ground-borne vibrations [9]. High-frequency measurements relate to problems associated with noise and train-track interaction forces.

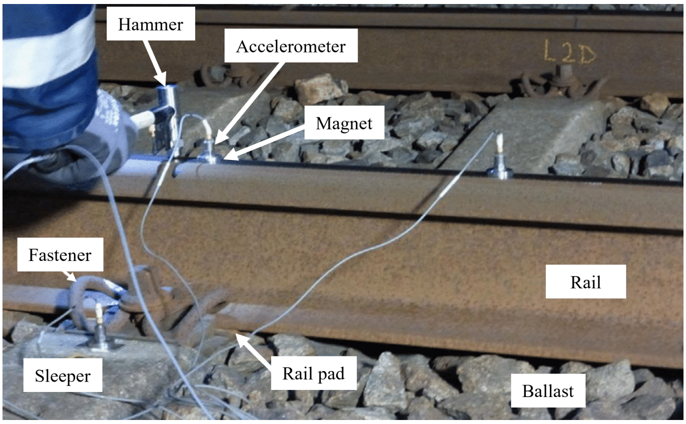

Fig. 3.1: Setup and equipment for hammer impact test on a railway track [37].

Track stiffness also influences the spreading of loads through the structure. A rail on a track with low global stiffness will experience large displacements and bending moments as more sleepers share the load, leading to lower forces on each sleeper [9]. However, a track with high global stiffness will induce small displacement and bending moments of the rail. Fewer sleepers will also share the load and therefore increase the forces exerted on each sleeper [9]. Generally, it is beneficial with high track stiffness because it results in higher resistance against the applied load and reduces the track deflection. Even so, a high track stiffness can also lead to increased wear and dynamic responses of track components [9]. A countermeasure is to include elastic components in the structure, such as the UBM.

3.2 Static Track Design

In 1888 Herman Zimmermann proposed a theoretical solution to determine the forces and deflections occurring in a single supported track loaded by rolling stock [28]. The method is based on Winkler´s theory from 1867 of elasticity and strength [28]. Winkler created a support model where the elements of the track are modeled as two continuous beams fixed at regular intervals of sleepers [15]. The sleepers are assumed to be supported from below and on each side by the non-deformable ballast bed. Winkler´s support model is based on a hypothesis that each point of the support has compressive stress proportional to the local compression [15]. In the Zimmermann method, the rail is considered an Euler-Bernoulli beam continuously supported on a Winkler foundation, as expressed in Fig. 3.2.

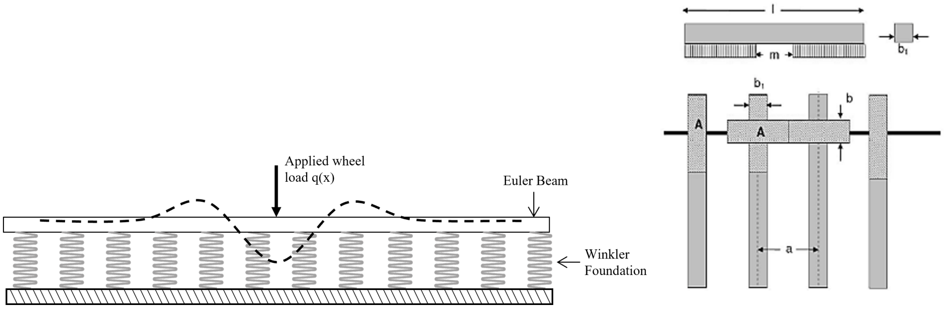

Fig. 3.2: Continuously supported Euler-Bernoulli beam with Winklers elastic foundation according to the Zimmermann method [17].

From Zimmermanns method, the rail deflection and bending moment can be found. It assumes that the bending stiffness and Winkler spring stiffness are constant. Thus, the deflection of the beam from equilibrium conditions can be expressed as

$$EI\frac{d^4y}{dx^4} + ky(x) = q(x), \tag{3.1}$$

where

EI = bending stiffness of the rail [Nm^2]
k = foundation coefficient [N/m]
$y(x)$ = vertical deflection of the rail [m]
$q(x)$ = applied wheel load [N]

The general solution of the fourth-order differential equation for a beam of infinite length, in the case of a point load, can be expressed as

$$y(x) = e^{-\frac{x}{L}}\left(A \cdot sin(\frac{x}{L}) + B \cdot cos(\frac{x}{L})\right) + e^{\frac{x}{L}}\left(C \cdot sin(\frac{x}{L}) + D \cdot cos(\frac{x}{L})\right), \tag{3.2}$$

where L is the characteristic length. The characteristic length depends on the relationship between bending stiffness and foundation coefficient and is an indication of how the loads are distributed in the track [15]. The characteristic length is expressed as

$$L = \sqrt[4]{\frac{4 \cdot EI}{b \cdot C}}, \tag{3.3}$$

where b is the width of the transformed area of the sleeper [m], as seen in Fig. 3.2, and C is the ballast modulus of the track [N/m^3]. The width of the transformed area can be found from

$$b = \frac{(l - m) \cdot b_1}{2 \cdot a}, \tag{3.4}$$

where

l = length of sleeper [m]
m = length of unsupported area [m]
b_1 = width of sleeper [m]
a = sleeper spacing [m]

The ballast modulus is a very important parameter which can influence the overall behavior of the track, especially with regards to track design. The ballast modulus can be expressed by the following relation

$$C = tan(\beta) = \frac{p}{y}, \tag{3.5}$$

where

p = ballast pressure from loading of rolling stock [N/mm^2]
y = deflection of rail [mm]

The ballast modulus can vary from 0.01 N/mm^3 to 0.4 N/mm^3 depending on the location of the track [19]. From experimental measurements, the ballast modulus is very often influenced by other components. Therefore, according to Esveld [15] the ballast modulus can be based on experienced numbers. As shown in Table 3.1, it can be classified as poor, moderate or good.

Table 3.1: Proposed foundation modulus based on track quality [15].

Classification	**C [N/mm^3]**
Poor	0.03
	0.04
Moderate	0.07
Good	0.09
	0.11

Further, by implementing $y(\infty) = 0$ and $y(0) = 0$ as boundary conditions in Equation 3.2, the following expression for the deflection distribution is obtained by

$$y(x) = \frac{Q}{2 \cdot b \cdot C \cdot L} \cdot e^{-\frac{x}{L}} \left(sin(\frac{x}{L}) + cos(\frac{x}{L}) \right) = \frac{Q}{2 \cdot b \cdot C \cdot L} \cdot \eta(\frac{x}{L}), \tag{3.6}$$

Equation 3.6 can be derived twice to get the expression for the bending moment distribution, given by

$$M(x) = \frac{Q \cdot L}{4} \cdot e^{-\frac{x}{L}} \left(cos(\frac{x}{L}) - sin(\frac{x}{L}) \right) = \frac{Q \cdot L}{4} \cdot \mu(\frac{x}{L}), \tag{3.7}$$

where

x = distance from the applied load Q [m]
$\eta(\frac{x}{L})$ = deflection at any given point from the applied load Q
$\mu(\frac{x}{L})$ = bending moment at any given point from the applied load Q

3.3 Dynamic Track Design

3.3.1 Receptance

Receptance, also known as dynamic flexibility, is the ratio of the track deflection and the applied load. It is a function describing the dynamic properties of a railway track. If the track is loaded with a sinusoidal force, the receptance can be found. Receptance is the inverse of the track stiffness and shows the vibration amplitudes of a track as a function of vibration frequencies [14]. The receptance function is one function in a set of three frequency response functions, which is a type of transfer function [14]. The receptance function is given by the following expression

$$H^2_{wF}(f) = \frac{S_{ww}(f)}{S_{FF}(f)}, \tag{3.8}$$

where

$H_{wF}(f)$ = complex transfer function from force to displacement [m/N]
$S_{ww}(f)$ = autospectrum of the displacement [m^{2}s]
$S_{FF}(f)$ = autospectrum of the force [N^{2}s]
f = vibration frequency [Hz]

Fig. 3.3 shows a basic receptance function defined for a system with one degree of freedom, such as a mass hanging on a linear spring and damper.

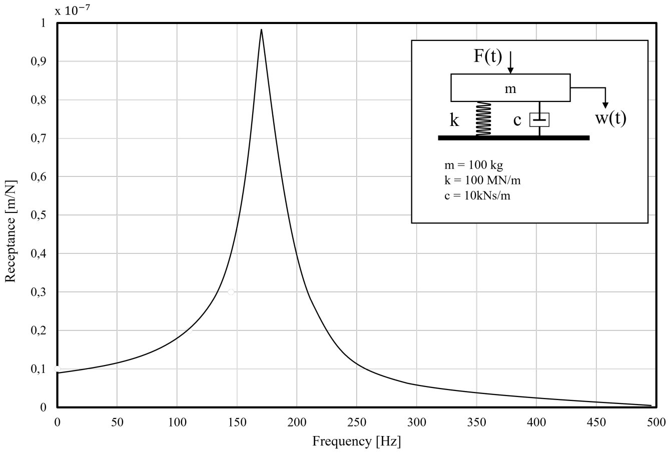

Fig. 3.3: Modulus of receptance function of one degree of freedom system [14].

The dynamic equilibrium equation for this system yields

$$C\frac{dw(t)}{dt} + Kw(t) = -M\frac{d^2w(t)}{dt^2} + F(t), \tag{3.9}$$

and by assuming a displacement function given by the following expression

$$w(t) = A_x e^{-i\omega t}, \tag{3.10}$$

the equilibrium equation can be transformed into

$$w(t)(-i\omega C + K - \omega^2 M) = F(t). \tag{3.11}$$

The solution of this equation relates only to frequency if the mass, spring, and damper properties are constant with respect to time and linear with respect to force and displacement [14]. Therefore, it can be called the receptance function and is given by the following equation

$$\frac{w(t)}{F(t)} = \frac{1}{K - \omega^2 M - i\omega C}. \tag{3.12}$$

The receptance function expressed as a modulus, H(ω), can further be deduced from the latter expression

$$H_{wF}(\omega) = \frac{1}{K}\sqrt{\frac{1}{\left(1 - \frac{\omega^2}{\omega_e^2}\right)^2 + \left(4\zeta^2\frac{\omega^2}{\omega_e^2}\right)^2}}, \tag{3.13}$$

where

$\omega \;= 2\pi f =$ radial vibration frequency [rad/s]

$\omega_e = \sqrt{\frac{K}{M}} =$ eigenfrequency [rad/s]

$\zeta \;= \frac{C}{2\sqrt{KM}} =$ damping ratio [-]

The receptance function refers to a position because it is a transfer function, making it possible to find the direct receptance applying to a single position where the loading and displacement coincide [14].

3.3.2 Resonance

Resonance is a phenomenon resulting in an increased amplitude when the frequency of a periodically applied force is equal to or close to the natural frequency of the system [10]. Several resonances can be found for a railway track. From Fig. 3.4, the peaks indicate resonance frequencies at different locations of the track.

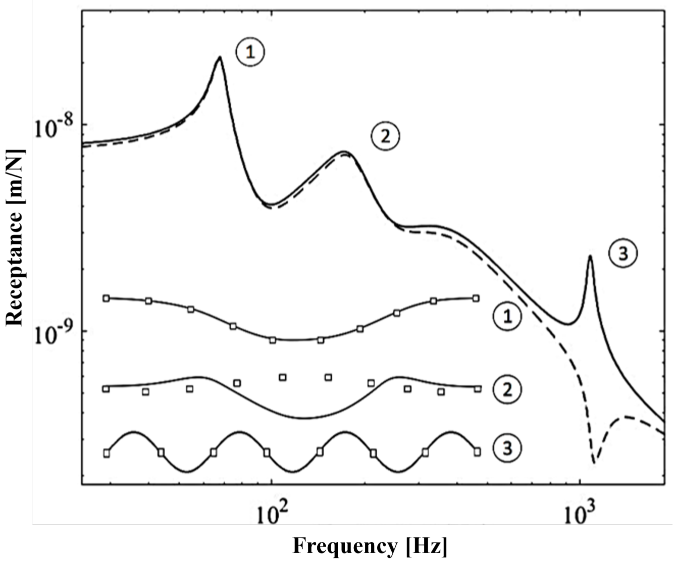

Fig. 3.4: Typical track receptance of model with discrete supports and sinusoidally varying force [10].

There are particularly three vertical resonance frequencies of interest. From Fig. 3.4, the first resonance indicates that the sleepers and rail are vibrating in phase [14]. At this resonance, the rail and sleepers move like one mass elastically connected to the ballast and occur in a frequency range of 50 to 300 Hz [10]. This is also in the frequency range of ground-borne noise and vibration [27]. The second point indicates that the sleepers and rail vibrate out of phase, thus acting as independent masses connected by spring-like rail pads. This resonance typically occurs in the range of 200 to 600 Hz and depends on the rail pad stiffness [10].

The third point in Fig. 3.4 is the pin-pin resonance frequency, which is the most significant preferred vibration mode of beams [14]. The vibrating mode consists of movement located in the rail, while the support resembles discrete points or pins. This resonance occurs when the wavelength of the rail bending waves are twice the sleeper spacing and is found at frequencies slightly less than 1000 Hz [10]. Pin-pin resonance appears in one primary mode and several higher modes, in which the mode has the highest amplitudes. The displacement occurring due to this vibration mode is poorly damped since only the rail's internal damping influences the response[10]. It also depends on the excitation position, as it generates a maximum between sleepers and a minimum above the sleeper, therefore called resonance and anti-resonance, respectively [14].

The railway track is exposed to multiple dynamic excitations, especially from irregularities and parametric excitation [29]. Typical irregularities can be unevenness or roughness in the contact surfaces between wheel and rail. Especially corrugation, which is a wave-type of wear on the rail, can cause excitation of the corrugation-passing frequency [26]. There are regulations set by Bane NOR regarding the maintenance limit of such damages, which is 0.06 mm when corrugations have a wavelength of 0 to 300 mm [31]. Parametric excitation is another essential dynamic excitation mechanism causing vibrations from the variations of support stiffness during the passage of each sleeper [29]. This results in periodic excitations at the sleeper passing frequency. The sleeper passing frequency is closely related to the train's speed and is relevant for ground-borne noise for high-speed trains and relevant to vibrations at lower speeds [29]. The track's resonance frequency should not coincide with these frequencies. The relation of corrugation- and sleeper-passing frequencies are given by the following equations

$$f = \frac{v}{\lambda}, \tag{3.14}$$

and

$$f = \frac{v}{d}, \tag{3.15}$$

where

f = frequency [Hz]
v = speed [m/s]
d = sleeper spacing [m]
λ = corrugation wavelength [m]

3.3.3 Damping

Damping is the effect of reducing or preventing a systems dynamic movements, and occurs in physical systems that dissipate energy during a process [16]. There are several sources from which damping can originate from, such as energy loss during hysteretic loading, viscoelastic material properties or contact friction [16]. It can also result from material non-linearity resulting in inelastic dissipation or internal friction of a system [16]. The main reason damping is important, is to avoid infinite oscillations of a system when it is exposed to dynamic loading conditions. Different mathematical formulations use various approaches to express the viscous damping. The most widely used numerical method to express viscous damping is Rayleigh damping, given by the following expression

$$C = \alpha M + \beta K, \tag{3.16}$$

in which C is the damping matrix, and is a linear combination of the mass and stiffness matrices, given by M and K respectively [39]. For each matrices an inherent Rayleigh damping coefficient must be defined, namely α for mass proportional damping and β for stiffness proportional damping [39]. These coefficients contribute to dampen lower and higher frequency behavior respectively, and is given by the following expressions

$$\alpha = \zeta \frac{2\omega_1 \omega_2}{\omega_1 + \omega_2} \tag{3.17}$$

and

$$\beta = \zeta \frac{2}{\omega_1 + \omega_2}, \tag{3.18}$$

where ζ is the damping ratio, defined in Equation 3.13, and ω_1 and ω_2 indicates a frequency range of interest. Some materials have damping properties defined with loss a factor, η, which is related to the damping ratio as $\eta = 2\zeta$ [39].

3.4 Track Loads and Stresses

The increasing demand for train passage has led to a focus on modernization and expansion of current and new railroads. As a consequence of this development, the track structure will experience higher train speeds and increased axle loads, which will lead to larger forces exerted on the track.

The track structure is frequently exposed to static and dynamic loads from rolling stock, which results in vertical, longitudinal, and lateral forces on the track. The static loading on the track structure includes two components, the live load, the train weight, and the dead load, which is the weight of track and subgrade [21]. In general, train weight is the dominant component of static loading, but the weight of track and subgrade is also significant when designing and analyzing the track. The dynamic loads occurring during train operations are generally different from the static loads in magnitude, as they can be significantly higher or lower [21]. A common method for selecting a dynamic wheel load during track design is to augment the static wheel load with a dynamic load or impact load factor [15].

The dynamic load can be divided into two categories. They are either short duration forces in which the vehicle suspension plays little or no role or longer duration forces that depend on vehicle suspension response [21]. Short duration forces are high-frequency impact loads arising from the wheel or rail discontinuities [20]. A rail discontinuity occurs over a short track length. Therefore it produces a short duration load pulse with no time for the vehicle suspension and the track foundation to react to the corresponding dynamic load [20]. This response results in locally confined damage to the wheel, rail, and sleeper. Longer wave-length track geometry irregularities produce an increased duration response. This makes time for the dynamic wheel loads to be influenced by the vehicle suspension and further transmitted into the track substructure, including ballast and subgrade [20]. Consequently, it results in downward movement of the unsprung mass, rail, and sleeper mass and affects the compression of ballast.

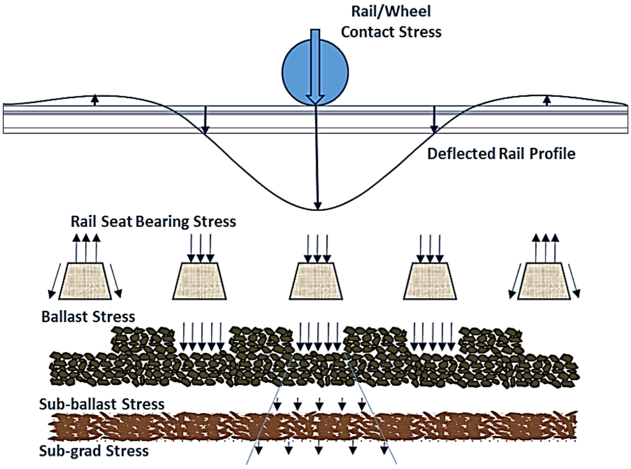

Fig. 3.5: Stress distribution through track structure from single wheel load [22]

Static and dynamic loads generate stresses in the track structure which is distributed through each part of the track, as shown in Fig. 3.5. It is also important to distinguish stresses induced by load from rolling stock and those due to the weight of track and subgrade [21]. Stresses caused by rolling stock are concentrated point loads at the wheel-rail interface, which decreases with increasing depth due to load-spreading capabilities through each part of the track. Conversely, stresses due to the weight of track and subgrade will increase with depth [21].

Understanding and quantifying how loads are transmitted from the wheel-rail interface is essential for the design of the track. Especially the vertical and lateral forces exerted on the rail will lead to bending and contact stresses in the railhead. The estimation of inflicted stresses and use of correct material for the rail must be considered to sustain tensile and bending stresses and excessive deflection [17]. During the design of sleepers, the resulting pressure exerted on the ballast should not exceed the admissible stress of 0.3 MPa [15]. The spreading of pressure loads from sleeper to ballast depends on the design of the sleeper. Because length and width are the most important parameters in designing sleepers, they are usually tapered with a wider bottom to distribute loads onto a larger area and reduce pressure loads on the ballast layer [17].

The ballast layer plays an essential role in a conventional railway track, as it provides lateral and longitudinal resistance to track movement. Ballasted tracks show excellent performance under a variety of loading conditions and can be the most cost-effective track structure if it is maintained and built with proper techniques [21]. One of the main functions of the ballast is to prevent the transmission of damaging stress changes to the underlying ground or subgrade [49]. The stress distribution in the ballast layer is not equal at all points as it consists of nonuniform rocks. This creates load chains where the exerted forces are transformed from one rock to another, which results in high load peaks, and strong impact impulses at these points [43]. If the ballast bed is overloaded, it can cause rapid deterioration of the quality of the track geometry.

3.4.1 Stadler FLIRT 75

Stadler FLIRT 75 is a local train designed by Nose and is delivered by Stadler Rail, Switzerland, and is shown in Fig. 3.6 [12]. A layout of the train and the dynamic properties are presented in Section A.1. The train consists of five wagons with seven different bogies. A bogie is the framework that carries a wheelset. This train can reach speeds up to 200 km/h and has a mean axle load of 185 kN. It will be used to simulate the axle load applied to the modeled track structures.

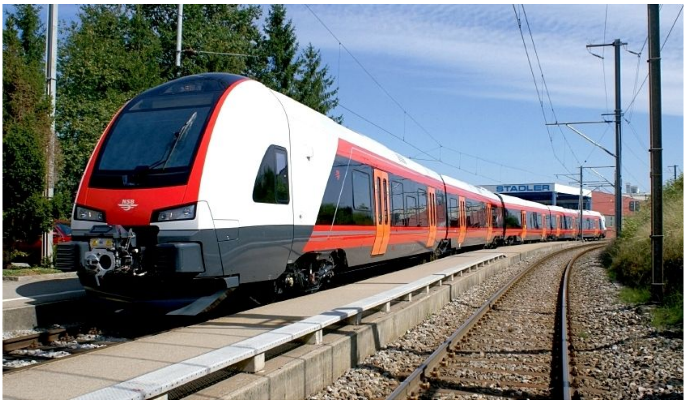

Fig. 3.6: Illustration of the Stadler FLIRT 75 train [12].

4

Numerical Modelling in Abaqus

The subject of this chapter is the routines available in the commercial software Abaqus for numerical modeling. Parts of the theory presented in this chapter is based on findings from Project Thesis, fall 2021. Abaqus is a non-linear finite element analysis software that offers a wide range of material definitions and complex assemblies. The software also provides pre-processing and post-processing capabilities [50]. Abaqus has an advanced user-interface to visualize all modeling procedures, including analysis results. Parallelization is also available in Abaqus, meaning that multiple processors can be used during analyses, which enhances the computational efficiency [50].

Abaqus is based on the finite element method (FEM), a numerical method that involves subdividing a structure into an assembly of non-overlapping subregions, referred to as finite elements [11]. The approach is to interconnect the elements at nodes by enforcing compatibility, then construct and apply boundary conditions. The mathematical model is approximated with a discrete model having a number of degrees of freedom (dof) [11]. When all the individual elements are identified by nodes, dof, and the local stiffness matrix, it can be assembled to a global domain with applied mechanical loads [11].

4.1 Modules

The Abaqus software is divided into different modules which define important aspects of the final structure [45]. The first module is based on creating parts for the complete structure, with specific geometries and assigned material properties, as seen in Fig. E.1a and Fig. E.2a. Several material properties in Abaqus can be assigned to a part in the property module, such as elastic and plastic behavior. The structure is then assembled in the assembly module by combining and translating parts, as seen in Fig. E.5a. If needed, the parts become multiple instances in the assembly.

For the instances to interact, it is necessary to connect them in the interaction module, as seen in Fig. E.5b. Abaqus offers a variety of interactions between the instances, such as constraints and connectors. After applying interactions, the load acting on the model and associated boundary conditions are defined in the load module, shown in Fig. E.8a. Before the model is analyzed, it has to be meshed, which is done in the mesh module, shown in Fig. E.10b. In this module, the instances are meshed either independently or dependent of the whole assembly. Firstly, seeding is applied to each part or section where the mesh size is determined, and then a mesh control will be performed before choosing the specific element type. Thus, the meshing technique varies with element type and the geometry of the model.

Further, in the step module, the analysis of the model is divided into different steps, such as static and dynamic procedures. In this module, the time period and increments of the analysis are determined, as seen in Fig. E.7a. The different steps also offer a variety of outputs, such as displacement and stress. Finally, a job file is created to monitor the models during analysis.

4.2 Elements

Abaqus offers an extensive library of elements to solve many different problems. Five aspects of an element will characterize its behavior; family, degrees of freedom, the number of nodes, formulation, and integration [44]. Fig. 4.1 shows the element families that are commonly used in analyses. Each element type depends on the modeling space, 2D planar space, 3D space, or axisymmetric space. Different element shapes are available in each case, such as beam, shell, rigid, solid spring, and dashpot elements.

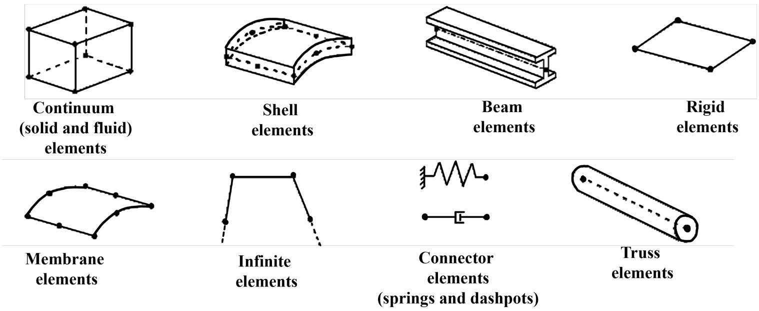

Fig. 4.1: Commonly used element families [44].

The number of degrees of freedom (dof) is the fundamental variable calculated during the analysis, and in stress/displacement simulation, the degrees of freedom are the translations [1]. The displacements or other degrees of freedom are calculated at the nodes of the element. The number of nodes determines the order of interpolation, such as linear or quadratic interpolation [1]. Most of the stress/displacement elements in Abaqus are based on a Lagrangian formulation, which is the mathematical theory used to define the behavior of the elements [1]. Then, Abaqus use numerical techniques to integrate quantities over the volume of each element, which allows for a complete generality in material behavior.

The most common mesh element in Abaqus is the solid continuum elements. These elements are classified as hexahedral, tetrahedral, or wedge, as illustrated in Fig. 4.2. Abaqus also supports three different types of hexahedral elements: linear fully integrated bricks (C3D8), reduced-integration bricks (C3D8R), and incompatible mode bricks (C3D8I) [46].

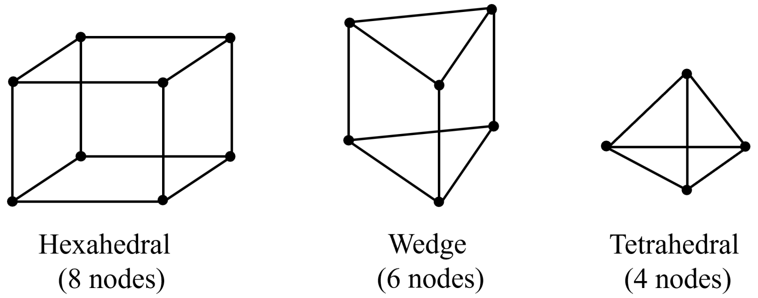

Fig. 4.2: Solid continuum element types.

C3D8R elements are the default element type in Abaqus, mainly due to their efficiency and a high tolerance for distortion. However, the primary issue with C3D8R elements is the occurrence of hour-glassing, which can result in mesh instability and necessitates a finer mesh [38]. While the C3D8 elements are highly efficient, they can be excessively stiff in bending applications, resulting in shear-locking difficulties [38]. C3D8I elements, on the other hand, were developed in Abaqus to avoid the artificial stress caused by pure bending and to be more accurate than the C3D8 elements [38]. Despite this, the C3D8I element type is susceptible to element distortions.

4.3 Analysis type

As mentioned previously, there are various step-options in Abaqus. It is possible to divide an analysis into steps, in which you assign different analysis procedures. In each step, different boundary conditions or loading conditions can be specified.

4.3.1 Static Analysis

A general static analysis step can be conducted in Abaqus as either linear or non-linear. In both cases, the load and boundary conditions must be specified. If non-linearities are included in the model, the NLGEOM function must be turned on. The NLGEOM function will account for large-displacement effects, material nonlinearity, or boundary nonlinearities[5]. This step uses a series of increments as a fraction of the applied load with a default period of 1.0 units. This function will correlate to the chosen amplitude of the applied load, such that 100% load is applied at 1.0 units of time. A criterion for the analysis to be possible is to have a stable model to avoid buckling or collapse [5].

4.3.2 Natural Frequency Extraction

The frequency extraction process calculates a system's inherent frequencies and related mode shapes using eigenvalue extraction [4]. This method is a linear perturbation procedure, and Abaqus provides three eigenvalue extraction methods; Lanczos, automatic multi-level substructuring (AMS), and subspace iteration [4]. In this case, the Lanczos method and subspace method are of interest. The Lanczos method is faster if many eigenmodes are required, while the subspace method is faster for smaller systems [4]. The subspace method is limited to the maximum eigenvalue of interest, while the Lanczos method requires a range of eigenvalues of interest.

4.3.3 Steady-State Dynamic Analysis

Steady-state dynamic analysis is used to calculate the steady-state response of a system due to harmonic excitation. It calculates the response based on the system's eigenfrequencies and modes, which requires an eigenfrequency extraction procedure before the steady-state dynamic analysis. Abaqus offers two types of steady-state dynamic analyses, namely modal-based and direct-solution [3]. For the modal-based solution, the eigenfrequencies must be extracted before running the analysis, and the frequency ranges of interest must be specified [3]. For the direct-solution steady-state dynamic analysis, a frequency sweep is done by applying the loading at different frequencies and then recording the response. A frequency range is given as input, ranging from a lower- to high-frequency value, as well as a number of points measured during the analysis [2].

5

Numerical Procedure

This chapter presents the numerical procedure for the constructed 3D models in Abaqus. The steps in the adopted numerical procedure are summarized in the flowchart, shown in Fig. 5.1.

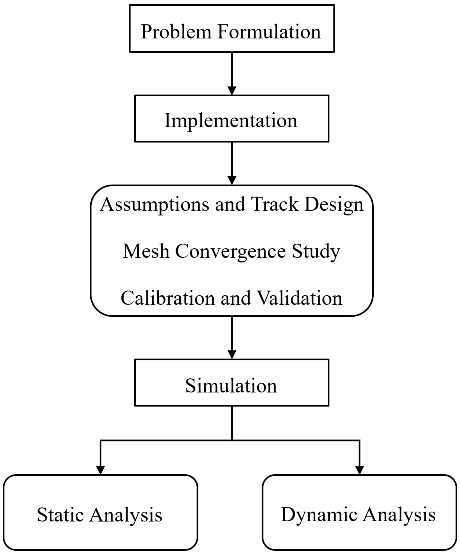
Problem Formulation
Implementation
Assumptions and Track Design
Mesh Convergence Study
Calibration and Validation
Simulation
Static Analysis
Dynamic Analysis

Fig. 5.1: Flowchart of the numerical procedure.

The numerical procedure includes three main steps: problem formulation, implementation, and simulation. The problem formulation is to create a numerical model that can predict the track system's response when including an additional elastic component, the UBM. In the implementation step, four sub-steps must be conducted before simulations of the models. Stated assumptions must limit the numerical modeling due to complexity and capacity. These limitations will further contribute to a final track design, including the type of geometry, interactions, loading conditions, and what type of analysis should be run. Other essential steps in the implementation phase are mesh convergence study and calibration and validation. These steps must be conducted to achieve a more reliable track design and simulations. The simulations will consist of static and dynamic analyses, which will be post-processed and interpreted.

5.1 Assumptions and Track Design

Two 3D models are modeled to evaluate the optimum track design for analyzing static and dynamic responses while introducing an additional elastic component, the UBM. Henceforth, the models will be referred to as the 3D beam model and the 3D solid model. The overall design of the 3D models is presented in Fig. 5.2 without the UBM. The assumptions below apply to the models and will be the foundation for the track design.

- The track is located in a tunnel, which implies hard underground and walls that will prevent ballast flow.
- A straight track will be considered and therefore neglect any curvature.
- The study is limited to one type of train, which is the passenger train Stadler FLIRT 75, mentioned in Subsection 3.4.1.
- The model will only include one additional elastic component, namely under ballast mat (UBM).

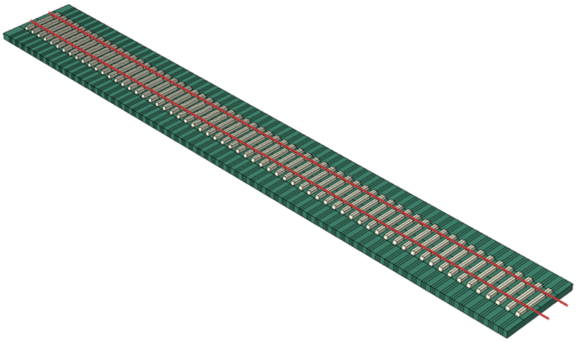

Fig. 5.2: 3D model created in Abaqus of a ballasted track with discrete support.

The modeled track structures consist of rails, rail pads, sleepers, ballast, and UBM. The tracks are 40 meters long and 5 meters wide, with a track gauge of 1.435 meters. For the 3D beam model, the rails are represented as wires. A wire feature in Abaqus can be assigned different profiles, and in this case, the I-profile is the most suitable profile, as shown in Fig. 5.3. Further, the dimensions of the 60E1 profile, from Section 2.1, can be approximated with the input parameters, given in Table 5.1.

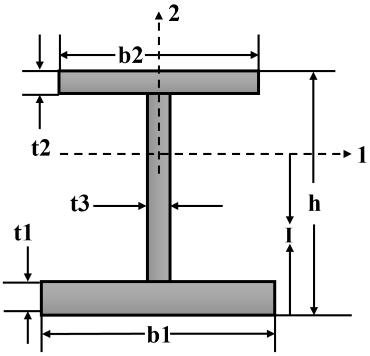

Fig. 5.3: I-shaped profile available in Abaqus.

Table 5.1: Input parameters for I-profile in Abaqus

Parameter	Value [m]
I	0.084
h	0.159
b1	0.15
b2	0.07
t1	0.0145
t2	0.363
t3	0.016

The rendered wire profile of the rail is shown in Fig. 5.4a. The 3D solid model consists of rails with solid features, where the profile of the rail is created in the part module, as shown in Fig. E.1a. The profile is designed according to the parameters set for the I-profile in the 3D beam model, as shown in Fig. 5.4b.

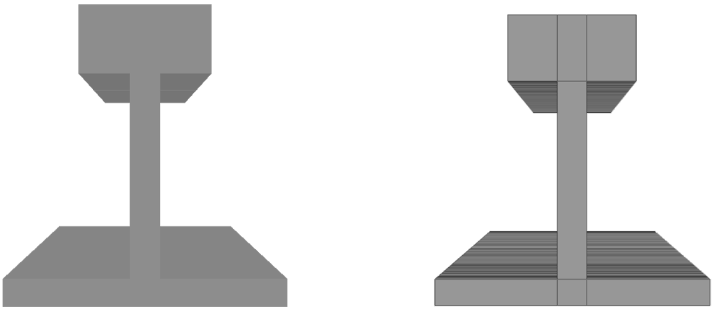

(a) Rail profile in 3D beam model.

(b) Rail profile in 3D solid model

Fig. 5.4: Comparison of the different rail profiles between the 3D models.

Because the rails are wire features in the 3D beam model, they are connected to the remaining structure with springs and dampers in parallel, as shown in Fig. 5.5a. The spring-damper system represents the rail pads and is fixed with two dofs to the center of each sleeper. Unlike the 3D beam model, the 3D solid model is not connected to the remaining structure with a spring-damper system but is tied to the structure with solid featured rail pads. The rail pads are dimensioned according to the Pandrol 10 mm Studded rail pad from Section 2.2, shown in Fig. 5.5b. They are also represented with solid features and placed on the center-line of each sleeper. A surface-based tie contact is established between the rails and rail pads and between the rail pads and sleepers. This contact feature ensures interaction between the rails and the remaining structure. A master and slave surface is chosen for this type of interaction, where the slave surface has a finer mesh than the master surface. In both models, there are in total 128 rail pads.

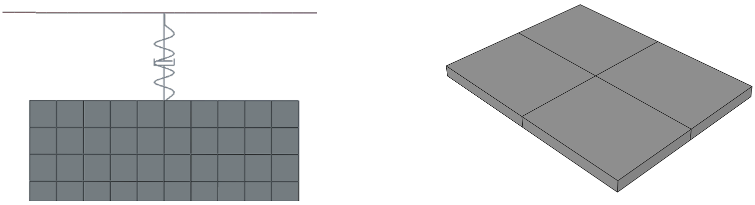

(a) Rail pad in 3D beam model.
(b) Rail pad in 3D solid model

Fig. 5.5: Comparison of rail pad profiles from the two 3D models.

Besides the models having different representations of rails and rail pads, the rest of the superstructure is similar for the 3D beam model and the 3D solid model. There are, in total, 64 sleepers with the profile shown in Fig. 5.6, and is derived from the JBV60 sleeper in Section 2.3. The sleepers are represented as 3D solid features in Abaqus and are 2.6 m long, 0.25 m wide, and have a height of 0.2 m. A slope of 10°is applied on each side of the sleeper. The sleepers are placed onto the ballast with a sleeper distance of 0.6 m. The sleepers are connected to the ballast layer with a surface-based tie connection.

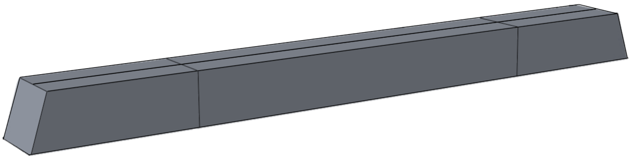

Fig. 5.6: Profile of modeled sleeper in Abaqus.

The ballast is a 40 cm thick solid featured layer with a width of 5 m and length of 40 m. As seen in Fig. 5.7, the ballast layer is partitioned at the surface interacting with the sleepers. This procedure is done to limit the slave- and master-surface interaction between the sleepers and the ballast layer. The UBM is a solid featured layer placed beneath the ballast, with a varying thickness of 18 mm and 20 mm. The UBMs are connected to the ballast layer with a surface-based tie connection, as shown in Fig. 5.7.

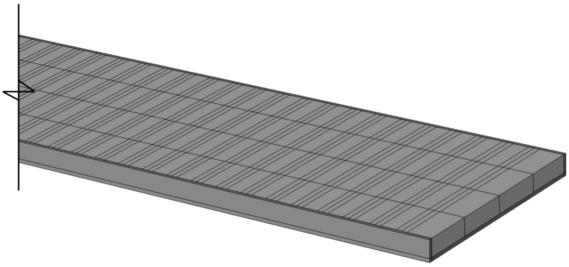

Fig. 5.7: Modeled ballast and UBM connected together in Abaqus.

Because the track is located in a tunnel, the superstructure is confined to a stiff substructure. Therefore, boundary conditions in the vertical and lateral directions are applied to the lowest part of the model to simulate this situation. The lowest part of the model could either be the ballast or the UBM, as shown in Fig. 5.8a and Fig. 5.8b, respectively. There are several types of boundary conditions available in Abaqus, such as symmetry or displacement boundary conditions, as shown in Fig. E.9a. Since there are no symmetry conditions related to the ballast in the vertical direction, a displacement boundary condition constraining three dofs at the bottom of the ballasted layer is applied.

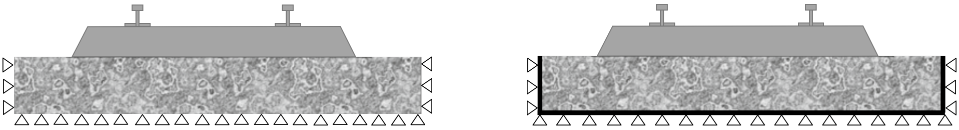

(a) Boundary condition without UBM.

(b) Boundary condition with UBM.

Fig. 5.8: Boundary conditions applied to the 3D models with and without UBM.

From Fig. 5.2, the sleepers are placed on top of the ballast and not embedded in it. The reason for this is that the responsiveness of the track in the vertical direction is of interest. Thus, displacement boundary conditions are applied to simulate the restrained movements in the lateral and longitudinal direction exerted on the sleepers from the ballast, by constraining three dofs at each side of the sleepers. In addition to symmetry and displacement boundary conditions, Abaqus offers a type called ENCASTRE, which constrains motion in all directions. This boundary condition is applied to each end of the rails in the longitudinal direction for both models.

5.2 Mesh Convergence Study

The accuracy of FEM analyses depends significantly on how complex the modeling procedures are. As mentioned previously in Section 4.2, each part in a model has several points or nodes with specific degrees of freedom (dof). If a model consists of a substantial number of dofs, the model will become more accurate as Abaqus uses a series of discrete points to calculate the responses of the model. A more complex model will better capture the structural behavior of the model but can lead to increased CPU time (Central processing unit time), which can take hours or even days. Therefore, it is necessary to balance the complexity of the model against the CPU time by conducting a mesh convergence study. Mesh convergence will determine how many elements are required in a model to ensure that the result is not affected by changing the mesh size [6].

The system response, such as stress or deformation, will converge to a repeatable solution with decreasing element size. If the model shows a tendency of convergence, it will be independent of the mesh and further refinements of the mesh will not affect the results. The procedure is done through an iterative process by increasing the number of elements of each part in the model independently and recording the maximum vertical deflection. A size control of the elements is performed to apply seeds to the parts, as shown in Fig. E.10a, which determines the size of the elements. The deflection and CPU time is then plotted against the number of elements applied to each part. Further refinement of the mesh is inefficient beyond the intersecting point of the curves, as more elements increase the CPU time without improving the solution.

5.2.1 Study of 3D Beam Model

This section presents the outcome of the mesh convergence study of the 3D beam model. The 3D beam model is meshed structurally, and the applied load is a point load corresponding to maximum axle load of a Stadler FLIRT 75 train of 110.4 kN. The mesh convergence study is measured as deflection versus number of elements.

Rails

The rails have default mesh elements, which is the B31 linear beam elements. This element type is recognized as Timoshenko beam elements. Additionally, Abaqus offers B33 elements, referred to as Euler-Bernoulli beam elements. According to a study conducted by Mosavi et al. [23], the Euler-Bernoulli beam theory is incapable of considering the transverse shear stresses, whereas the Timoshenko theory is. Therefore, the Timoshenko beam elements (B31) are more suitable for investigating the track dynamics than Euler-Bernoulli and are chosen as beam elements for further analyses.

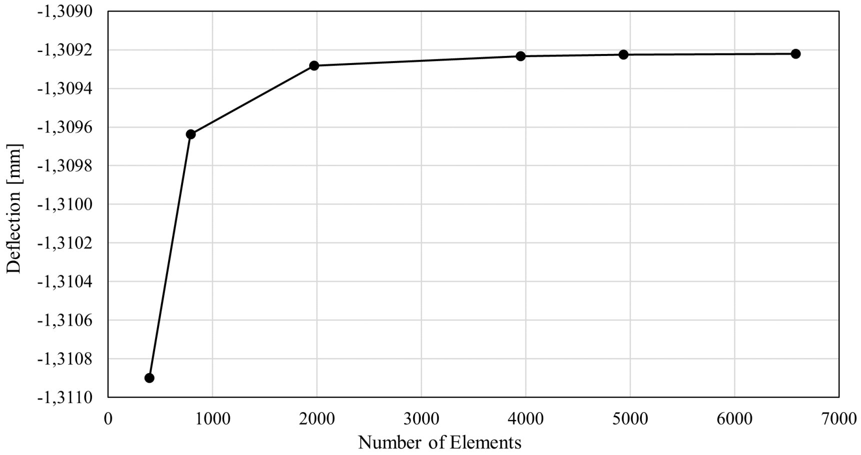

Fig. 5.9: Mesh convergence of rail with B31 linear beam elements.

The rails are analyzed by decreasing the global element size from 0.1 to 0.006, resulting in 395 to 6585 elements, respectively, as illustrated in Fig. 5.9. Because the rails are based on two-node beam elements, they will only idealize solid elements and will not require a large amount of solver time. After completing all iterations with smaller element sizes, an average CPU time of 30 seconds was recorded. The solver time is reasonably rapid and is ignored as it does not affect the solver time of the overall model. As illustrated in Fig. 5.9, the rails converges with a deflection of approximately 1.31 mm. At the selected point of convergence, the element size is 0.01 resulting in 3950 elements.

Sleeper

The sleepers are constructed using three-dimensional continuum solid elements with hexahedral geometry. Due to their hexahedral shape, they will be regarded as linear bricks with eight nodes. As previously stated in Section 4.2, hexahedral elements are classified into three types: C3D8, C3D8R, and C3D8I. Because the sleepers are composed of concrete, they should be free of the hour-glassing effect.

When C3D8R elements are used, the stiffness is first order, which is very low. As a result, they are more prone to abnormal deformation, such as hour-glassing. This effect results in significant deformations at the structure's center or near the site of application of the load. As a result, only C3D8 and C3D8I elements are of interest. The sleepers have a unique size control compared to the rest of the model's components. Rather than a global mesh size, it utilizes local seeding. Thus, as seen in Fig. 5.10, the mesh density increases towards the loading point and decreases away from it.

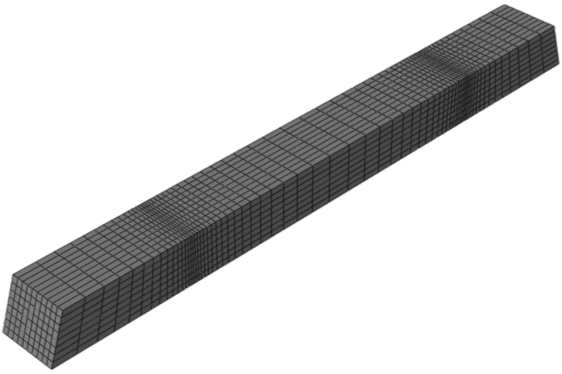

Fig. 5.10: Mesh of sleeper with decreasing element size in a vertical and horizontal direction towards connection point of rail pad.

As seen in Fig. 5.11, the sleepers do not converge regardless of the element type. Because the rail pads are modeled as springs and dashpots and directly connected to the sleepers, the transmitted force from the rail can act as a point load on the sleepers. This could lead to excessive deformation at the connected elements, rather than the load being distributed to the remaining elements of the sleeper. Nonetheless, as seen in Fig. 5.11, CPU time increases dramatically as the number of elements increases, regardless of the element type, and it is evident that the C3D8 components are stiffer than the C3D8I elements. Thus, the C3D8I elements are chosen due to their higher efficiency in terms of CPU time, resulting in a number of 5360 elements at a CPU time of 55.6 seconds.

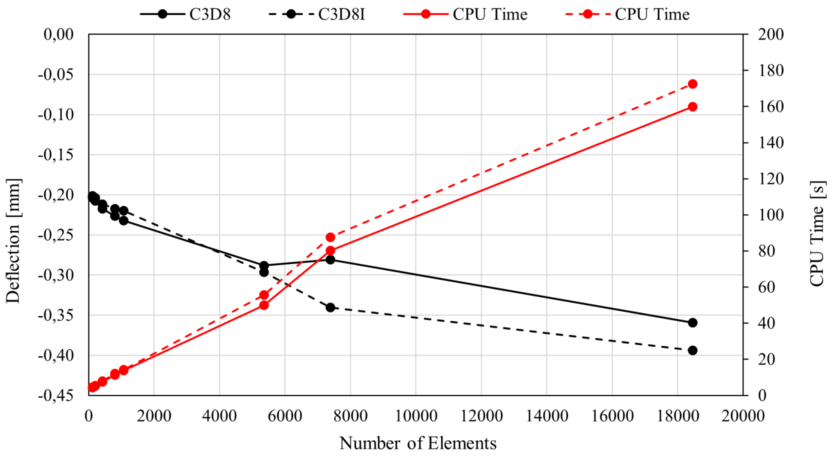

Fig. 5.11: Comparison between mesh convergence of sleeper with C3D8I and C3D8 elements, and measured CPU time with increasing number of elements. The black curves indicate deflection of the sleeper with C3D8 (solid line) and C3D8I (dashed line) elements. The red lines indicate measured CPU time for sleeper with C3D8 (solid line) and C3D8I (dashed line) elements

Ballast

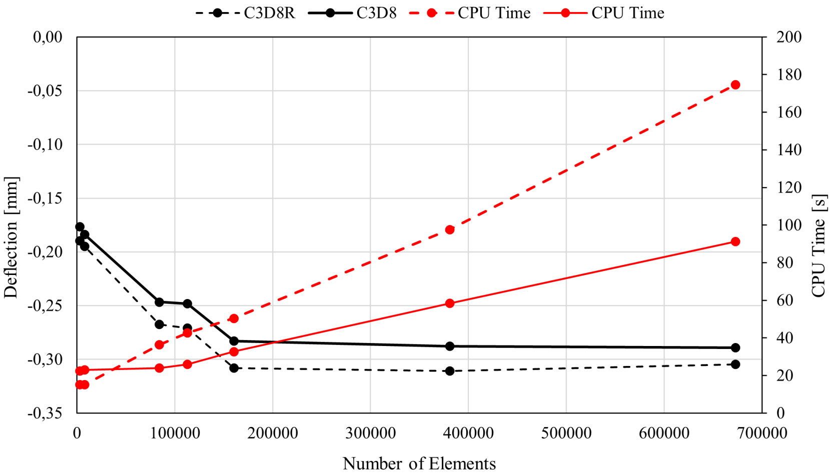

Fig. 5.12: Comparison between mesh convergence of ballast with C3D8R and C3D8 elements, and measured CPU time with increasing number of elements. The black curves indicate deflection of the ballast with C3D8 (solid line) and C3D8R (dashed line) elements. The red lines indicate measured CPU time for ballast with C3D8 (solid line) and C3D8R (dashed line) elements

The ballast is also modeled with three-dimensional solid elements having hexahedral eight-node linear bricks. Because the ballast's behavior is less known than the other components in the model, it was analyzed using both C3D8R and C3D8 elements. The global element size ranged between 0.3 and 0.05 in both cases, resulting in a range of 3104 to 672800 elements. According to Fig. 5.12, the C3D8R elements exhibit more deflection than the C3D8 elements due to significant element distortion. Although the C3D8R elements might be employed, a finer mesh would be necessary, leading to increased CPU time. As a result, the C3D8 elements are applied to the ballast layer with an element size of 0.08, with a CPU time of 32.7 seconds.

UBM

The UBMs are modeled as 3D solid elements with hexahedral eight-node linear bricks. The element type chosen for the UBM is C3D8 to remove the hour-glassing effect. A mesh convergence study of the UBM is not conducted as it must have greater mesh size than the ballast, due to default rules of their surface interaction in Abaqus. Because the UBM is chosen as master surface and ballast is slave surface, it must have a coarser mesh than the ballast layer. Therefore, since the element size of the ballast is 0.08, the UBM is applied an element size of 0.12 resulting in 16200 elements.

5.2.2 Study of 3D Solid Model

This section presents the outcome of the mesh convergence study of the 3D solid model. In this model, all instances, except the rail and rail pad, are assigned the same element types and meshing technique as the ones from Subsection 5.2.1. The same loading condition is also applied in the 3D solid model, with a maximum axle load of a Stadler FLIRT 75 train corresponding to 110.4 kN. The mesh convergence study is measured as deflection versus number of elements.

Rails

The rails are assigned 3D continuum solid elements. Because the C3D8I element type in Abaqus is less prone to experiencing hour-glassing, this element type is assigned to the rails. The rails are analyzed by decreasing the global element size from 1 to 0.007, generating 711016 and 1990 elements, respectively. From Fig. 5.13, the rail shows a clear tendency of convergence beyond a total number of elements equal to 91224, which results in a element size of 0.016. At this point, the CPU time is fairly high, reaching a time of 105.6 seconds. Even so, it is relatively low compared to the linear growth in CPU time as the number of elements increases.

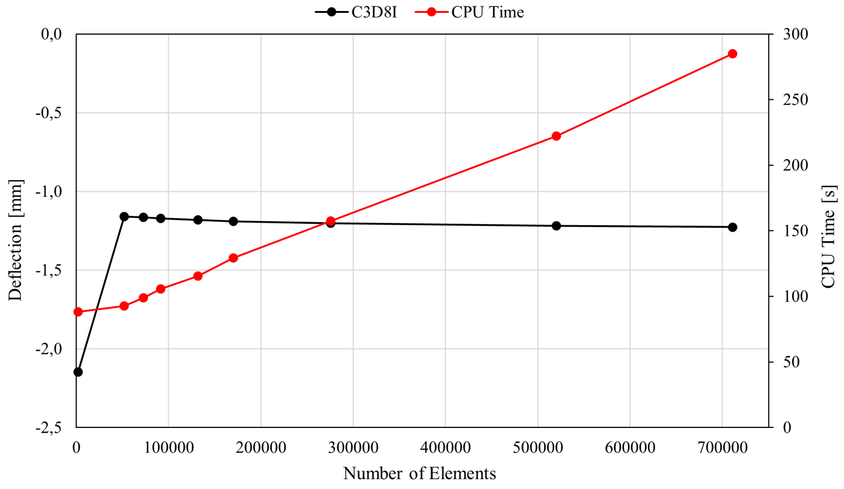

Fig. 5.13: Mesh convergence study of rail from 3D solid model, including measured CPU time against number of elements.

Sleeper

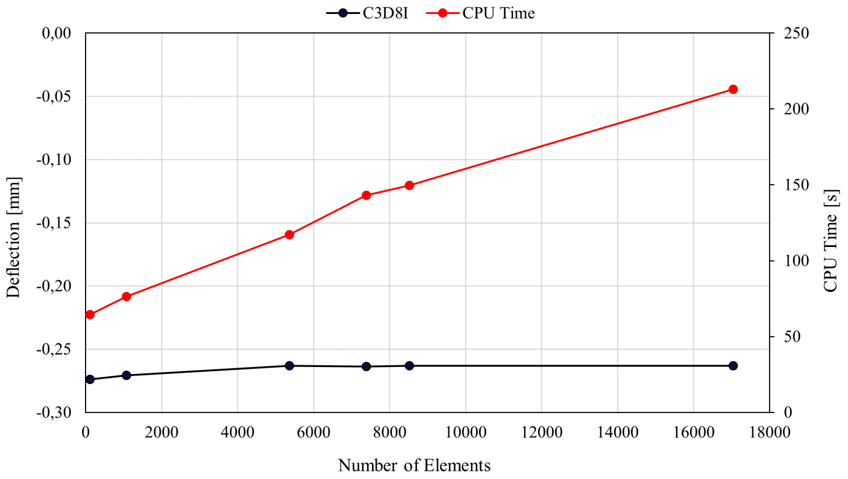

Fig. 5.14: Mesh convergence study of sleeper from 3D solid model, including measured CPU time against number of elements.

The same meshing technique of the sleepers in the 3D beam model are applied to the 3D solid model with the C3D8I element type. From Fig. 5.14, it is evident that the sleeper converges to an average deflection of 0.26 mm. However, the CPU time is overall very high, and increases linearly with number of elements. Therefore, the number of elements chosen for the sleeper is also 5360, but with an increased CPU time of 117.1 seconds.

Ballast

The C3D8 elements are also applied to the ballast in the 3D solid model. A global element size ranging from 0.3 to 0.05 is utilized and generated a total of 3104 and 672800 elements, respectively. From Fig. 5.15, the deflection curve of the ballast converges at an element size of 0.09 yielding a total number of elements of 84024. The number of elements on the ballast layer is therefore reduced compared to the 3D beam model, but because of the increasing CPU time it will be more efficient to have as few elements as possible.

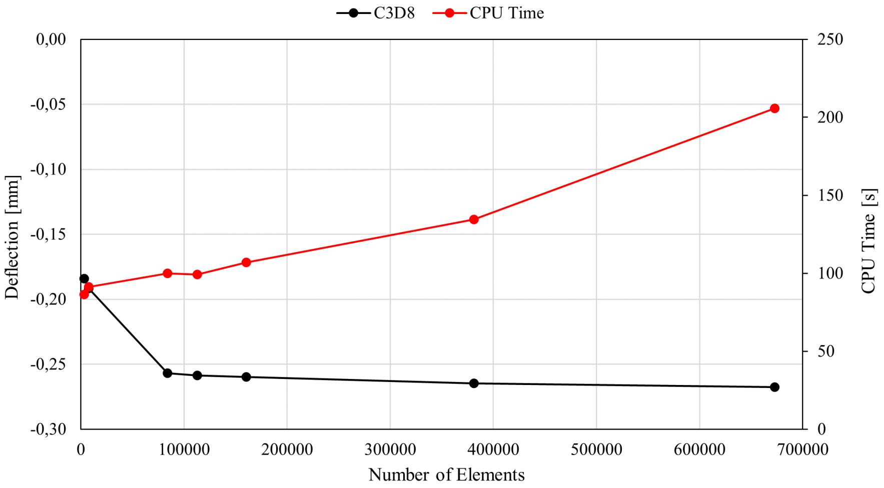

Fig. 5.15: Mesh convergence study of ballast from 3D solid model, including measured CPU time against number of elements.

Rail Pads and UBM

A mesh convergence study was not conducted for the rail pad or the UBM in the 3D solid model. Because the rail pad is placed between the rail and sleeper, its element size is determined based on its surface interaction with these components. The rail acts as a slave surface relative to the rail pad, while the rail pad act as slave surface relative to the sleepers. Therefore, it needs to have a finer mesh than the sleepers and a coarser mesh than the rail. Since the rail have an element size of 0.016 and the sleeper have an element size of 0.025 at the top, the rail pad's element size must lie within this range. Thus, the chosen element size for the rail pad is 0.02 yielding a total of 80 elements. The same procedure as in 5.2.1 is applied to the UBMs in the 3D solid model, which is an element size of 0.12 yielding a total number of elements equal to 16200.

5.3 Calibration and Validation

This section presents the calibration and validation of the 3D beam model. A 2D model calibrated against the Zimmermann method will be used as benchmark for calibration of the 3D beam model. It is mainly used to calibrate the 3D beam model due to having similar rail and rail pad, as opposed to the 3D solid model. However, the 3D solid model is compared to the calibrated 3D beam model to evaluate which design is the most efficient.

5.3.1 Calibration of 2D Model against the Zimmerman Method

The Zimmermann method from Section 3.2, is a one-dimensional analysis of a beam on an elastic foundation (BOEF). Even though the method simplifies a beam on continuous support, it is still beneficial for analyzing a simple design. Therefore, the results from the Zimmermann method will be used to calibrate a 2D model, shown in Fig. 5.16, to find appropriate material properties. The track design and mesh convergence study of the 2D model is presented in Section B.1 and Section B.2, respectively.

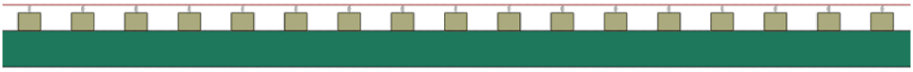

Fig. 5.16: 2D model

The Zimmermann method necessitates determining the ballast modulus, the applied load and the characteristic length. From Table 3.1 in Section 3.2, a ballast modulus of 0.09 N/mm^3 is utilized to calibrate the 2D model, yielding a track quality *good*. By assuming a 20.5-ton axle load, based on the maximum load exerted by a Stadler FLIRT 75 train, the static point load is found by multiplying the weight with the gravity constant. Since the method only considers one rail, the static point load must be divided by two. Additionally, a quasi-static factor is added to the static point load to simplify the non-linear system into a linear system. The quasi-static factor is found by multiplying the static point load with 0.1, yielding a total static point load of 110.4 kN.

The width of the transformed area must be determined to find the characteristic length, according to Equation 3.4. The length of a JBV60 sleeper is 2.6 m, which is divided by two concerning a single rail, and the average width is 0.25 m. The sleeper spacing is 0.6 m, and it is assumed that the length of the unsupported area is equal to zero. Since the bending stiffness of the 60E1 rail is known, the characteristic length can be determined according to Equation 3.3. All input parameters for the calculation of Zimmermanns formulation are presented in Table 5.2.

Table 5.2: Input parameters for calculations of the Zimmermann method.

Parameter	Value
Foundation modulus, C [N/mm^3]	0.09
Bending stiffness, EI [kNm^2]	6380
Sleeper spacing, a [m]	0.6
Length of sleeper, l [m]	2.6
Width of sleeper, b_1 [m]	0.25
Static point load, Q [kN]	110.4

The output parameters, based on the values from Table 5.2, are presented in Table 5.3. The maximum vertical deflection and the maximum bending moment are found when the distance along the rail is equal to zero, from Equation 3.6 and Equation 3.7.

Table 5.3: Output parameters from the Zimmermann method.

Parameter	Value
Width of transformed sleeper, b [m]	0.54
Characteristic length, L [m]	0.85
Vertical deflection, y_0 [mm]	1.33
Bending moment, M_0 [kNm]	23.5

These output parameters are further used to create deflection and moment distributions along the rail by using Equation 3.6 and Equation 3.7, as seen in Fig. 5.17. The point load is applied in the ordinate of x=0. These curves will further be used as benchmarks for calibrating the 2D model.

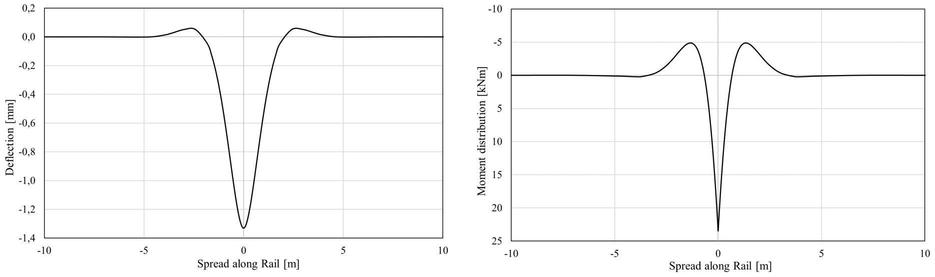

(a) Deflection distribution.

(b) Moment distribution.

Fig. 5.17: Deflection and moment distribution along an assumed 20 meter long rail, according to Zimmermann method from Section 3.2.

Specific components in the 2D model, such as rail and sleeper, already have defined properties, as presented in Table 5.4. All components in the model are considered to be linear elastic. Therefore, the calibration is primarily done to ascertain the material properties of the rail pad and ballast. The material properties that must be determined are density, damping, Young's modulus and Poisson's ratio for the ballast, and stiffness and damping of the rail pad. A literature review of typical values was undertaken to determine optimal values for these attributes.

Table 5.4: Properties used for calibrating railpad stiffness. The properties of 60E1 rail are kept constant for all simulations.

Material Property	**60E1 Rail**	**JBV60 Sleeper**
Young's Modulus, E [GPa]	210	30
Mass density, ρ [kg/m^3]	7800	2500
Poisson's ratio, ν	0.3	0.2
Moment of inertia, I$_{x-x}$ [m^4]	3.0383$\cdot$10^{-4}	-

An extensive literature review was performed by Rodrigues [36] to evaluate Young's modulus and Poisson's ratio of the ballast. The results from their research are presented in histograms, shown in Fig. 5.18, which shows that the value of Young's modulus usually lies between 100 to 150 MPa and Poisson's ratio between 0.3 to 0.35. The literature review also showed that the density of the ballast usually lies between 1800 and 2000 kg/m^3. An experimental analysis of the studded Prandrol 10 mm rail pad was conducted by Railcorp and Remennikov [30], showing that the rail pad has a stiffness ranging from 45 MN/m to 65 MN/m. Additionally, Bane NOR states that elastic rail pads, such as the studded Pandrol 10 mm rail pad, should have a stiffness ranging from 40 MN/m to 60 MN/m when used with concrete sleepers [35]. The damping property of the rail pad is suggested and provided by Bane NOR, with a value of 5 kNs/m.

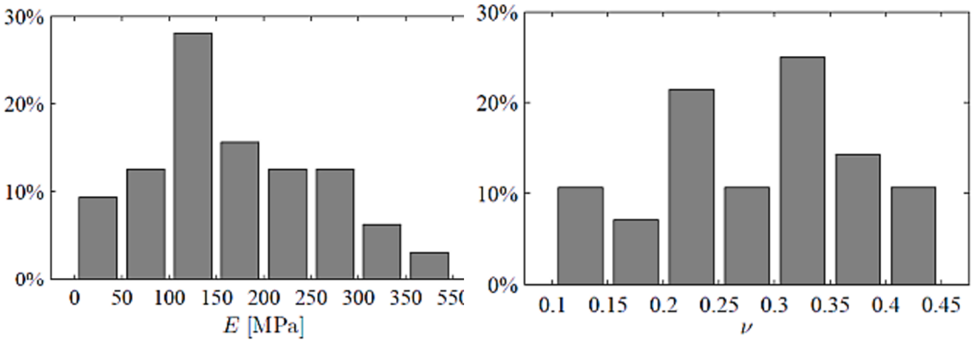

(a) Range of values for Young's modulus.

(b) Range of values for Poisson's ratio

Fig. 5.18: Literature research of (a) Young's modulus and (b) Poisson's ratio performed by Rodrigues [36].

Considering the suggested ranges of values for the necessary parameters of both rail pad and ballast, the 2D model was parameterized to match the results of the Zimmermann method. The density and Poisson's ratio of the ballast was determined to be 1800 kg/m3 and 0.35, respectively. Young's modulus of the ballast and the stiffness of the rail pad are determined by altering the values between the suggested ranges. After a series of tests, the optimal rail pad stiffness equaled 51 MN/m, and the Young's modulus of the ballast equaled 100 MPa. Fig. 5.23 and Fig. 5.24 shows the final curve fitting of the 2D model against the Zimmermann method.

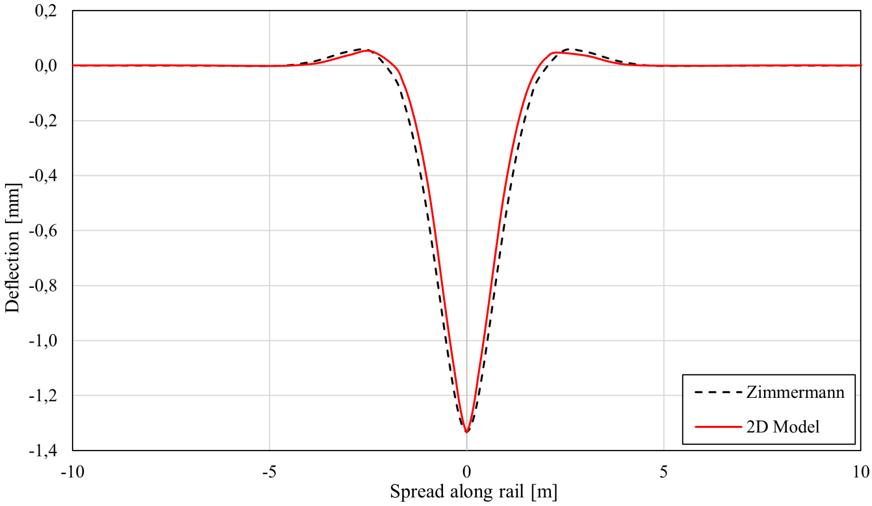

Fig. 5.19: Comparison of rail deflection between results from 2D model and the Zimmermann method.

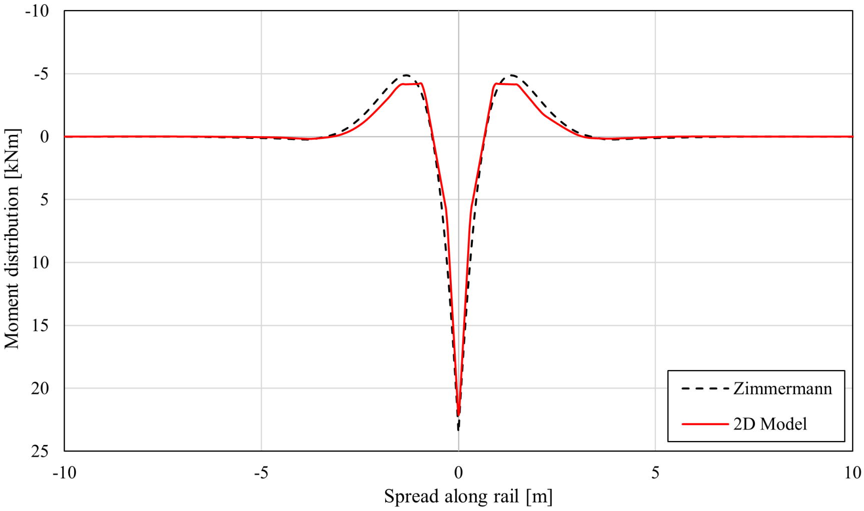

Fig. 5.20: Comparison of moment distribution between results from 2D model and the Zimmermann method.

As seen by the deflection curves, there is a good correlation between the 2D model and the Zimmermann method. The 2D model yielded a maximum deflection value of 1.334 mm, whereas the Zimmermann method yielded a maximum deflection of 1.332 mm. The moment distribution curves from the 2D model deviate more from the Zimmermann method. The 2D model yielded a maximum moment of 22.1 kNm, whereas the Zimmermann method yielded a maximum moment of 23.5 kNm. Nonetheless, the moment distribution measured from the 2D model exhibits the same tendency as the Zimmermann method, particularly in terms of the uplifting of the rail.

The damping properties of the ballast and the rail pad must be determined. The best way to verify the dynamic properties of a numerical model, particularly in terms of damping, is to compare its dynamic response in the form of a receptance curve, as mentioned in Subsection 3.3.1. This is done by conducting a steady-state dynamic analysis in Abaqus. The damping properties of the ballast is defined by Rayleigh damping in Abaqus due to its solid elements.

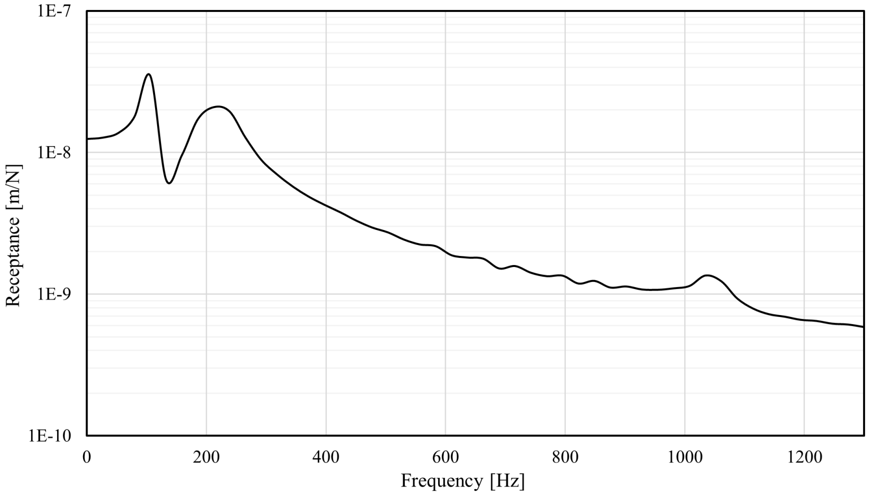

Fig. 5.21: Damping of ballast found from Rayleigh definition and damping of rail pad equal to 5E3

As mentioned in Subsection 3.3.3, two coefficients must be specified to define Rayleigh damping in Abaqus, namely α and β. Based on a numerical study done by Nguyen et al. [25], the ballast, with a damping factor of 10%, have strong effects on the track dynamics in the frequency range [125, 1885] rad/s. Thus, with the proposed input parameters, Equation 3.17 and Equation 3.18 are utilized to calculate the Rayleigh damping coefficients, resulting in α = 23.445 and β = 9.9502x10^{-5}. Including the Rayleigh damping coefficients for ballast and damping coefficient for rail pad corresponding to 5 kNs/m in the 2D model, yields the receptance curve presented in Fig. 5.21.

From the receptance curve, it is evident that there is much disturbance occurring, which likely originates from the rail pad. The rail pad mainly affects the medium-frequency and the low-frequency vibrations and makes the vibration frequency within this range higher. It may change the amplitude of the pin-pin resonance, but not necessarily the position. Therefore the damping of the rail pad is increased to 15 kNs/m. The increased damping of the rail pad yielded a smoother receptance function, as depicted in Fig. 5.22, and is comparable to the results obtained in the literature [18].

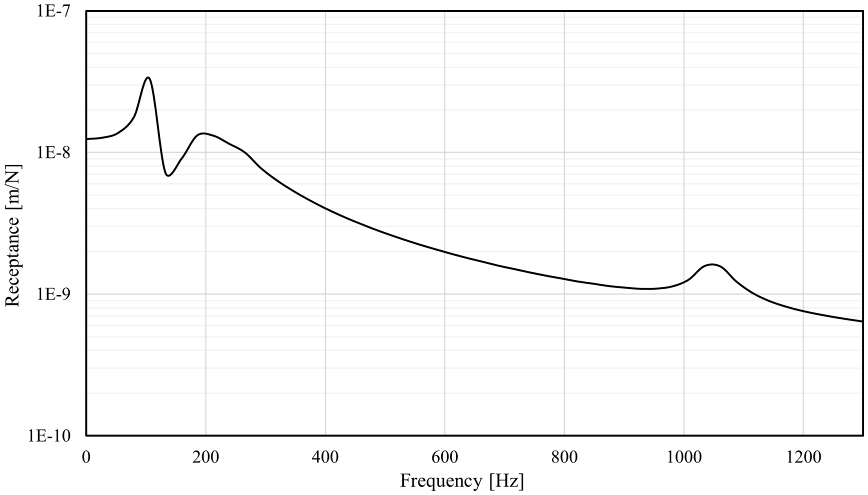

Fig. 5.22: Receptance curve of the 2D model with alternated damping properties.

5.3.2 Calibration of 3D Beam Model against the 2D model

Because Zimmermann's method only considers the static response of a track, the 2D model will be utilized to calibrate the damping properties of the 3D beam model. The material properties found from Subsection 5.3.1 are applied as material properties for rail, rail pad, sleepers, and ballast in the 3D beam model. First, the 3D beam model is subjected to static loading to validate the input attributes. It showed a more significant deflection than the 2D model. Thus, Young's modulus of the ballast layer was increased to 115 MPa to fit the deflection and moment distribution curves of the 2D model, as shown in Fig. 5.23 and Fig. 5.24 respectively.

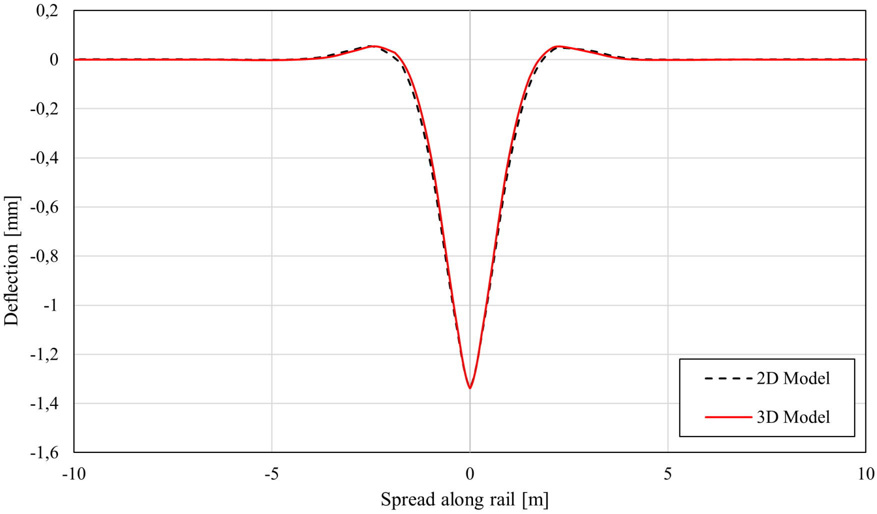

Fig. 5.23: Comparison of deflection curves between results from 2D model and 3D model.

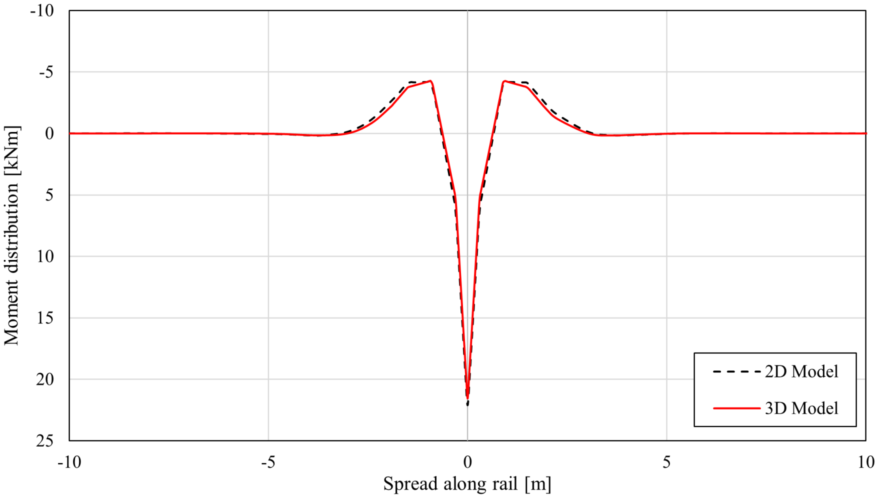

Fig. 5.24: Comparison of moment distribution between results from 2D model and 3D model.

There is a strong correlation between the static analysis of the 2D model and the 3D model. It is also possible to adjust the stiffness of the rail pad, but through trial and error, it became evident that the rail pad had a greater impact on the response than the elasticity of the ballast. Further, a dynamic receptance test is undertaken to determine the dynamic properties of the 3D beam model. First, the dynamic properties found from analyzing the 2D model are applied to the 3D model. Then a steady-state dynamic analysis with a sinusoidal load is conducted. The resulting receptance function from the 3D beam model is compared with the results from the 2D model, as shown in Fig. 5.25.

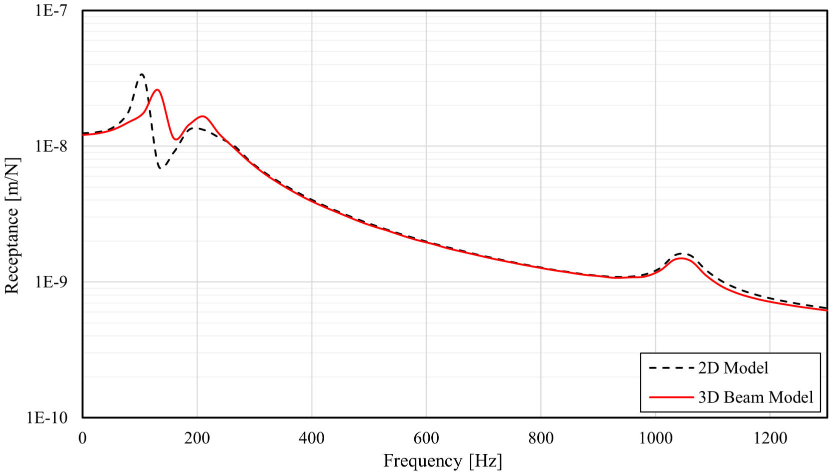

Fig. 5.25: Comparison of receptance test between 2D model and 3D model.

The receptance curve of the 3D beam model and the 2D model show similarities at frequencies above 260 Hz. This compliance between the receptance curves originates from the models having the same rail and rail pad features. On the other hand, there are variances in the receptance curves for frequencies below 260 Hz. Through an iterative process, the damping qualities of the ballast and rail pad are altered to fit the 2D curve. However, modifying the parameters did not affect the position of the amplitudes. Finally, the resulting material properties of the 3D beam model are shown in table Table 5.5.

Table 5.5: Properties found and used for modeling a rail on discrete support in 3D beam model.

Material Property	**60E1 Rail**	**JBV60 Sleeper**	**Ballast**	**Rail pad**
Moment of inertia, I_{xx} [m^4]	$3.0383 \cdot 10^{-4}$	-	-	-
Young's Modulus, E [GPa]	210	30	0.115	-
Mass density, ρ [kg/m^3]	7800	2500	1800	-
Poisson's ratio, ν	0.3	0.2	0.35	-
Rayleigh damping, α	-	-	23.445	-
Rayleigh damping, β	-	-	$9.9502 \cdot 10^{-5}$	-
Stiffness, k [MN/m]	-	-	-	51
Damping, c [kNs/m]	-	-	-	15

5.3.3 Validation of 3D Beam Model based on Modal Analysis

A modal analysis is performed to validate the dynamic behavior of the 3D beam model, by conducting a natural frequency extraction in Abaqus. Abaqus sweeps the whole model during natural frequency extraction, and since the model is composed of several components, multiple vertical vibration modes are observed during analysis. It is unclear from the analysis to which parts of the model the natural frequencies belong. Therefore, a direct steady-state dynamic analysis makes monitoring the response and identifying the eigenmodes easier. As shown in Fig. 5.26, the receptance curves with sinusoidal load acting between two sleepers and above a sleeper are found. These curves also demonstrate that the response of the track is consistent with theory from Subsection 3.3.2 since resonance and anti-resonance amplitudes are observed when the load is placed above the sleeper.

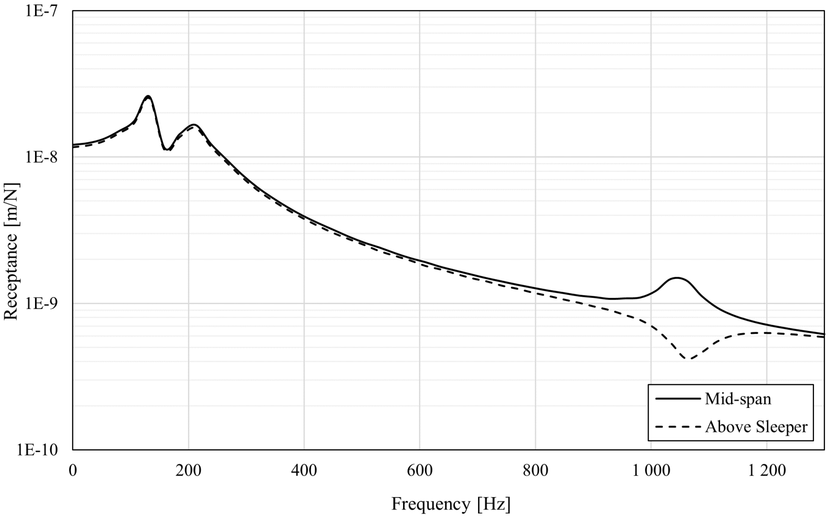

Fig. 5.26: Receptance of model without UBM mid-span and above sleeper.

There are three fundamental vibration modes of a railway track, as shown in Fig. 3.4 from Subsection 3.3.2. A natural frequency extraction step is conducted to extract those modal shapes of the track structure. As mentioned in Subsection 4.3.2, there are two eigensolvers of interest for this type of step, namely Lanczos and subspace. Due to the size of the model, the Lanczos method is chosen. It requires a frequency range of interest, which is chosen based on the resonance frequencies found from Fig. 5.26. Each resonance frequency indicates a modal shape of interest, and therefore minimum and maximum frequency are determined by the ranges presented in Table 5.6.

Table 5.6: Frequency range of natural frequency extraction.

Vibration Mode	Frequency Range [Hz]
Mode 1	130 - 133
Mode 2	211 - 213
Mode 3	1060 - 1062

The mode shapes from the natural frequency extraction are presented in Fig. 5.27, Fig. 5.28 and Fig. 5.29. The mode shapes coincide well with the principal resonance frequencies found from the receptance test, and the ones presented in the literature Subsection 3.3.2.

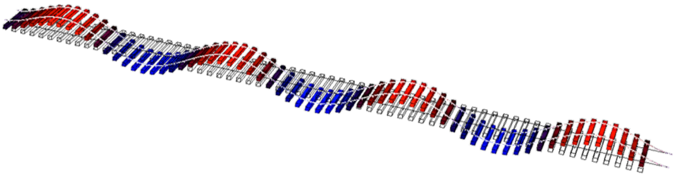

Fig. 5.27: The first modal shape showing the resonance where rails and sleepers bounce on top of the ballast, it is found at a frequency of 135.1 Hz.

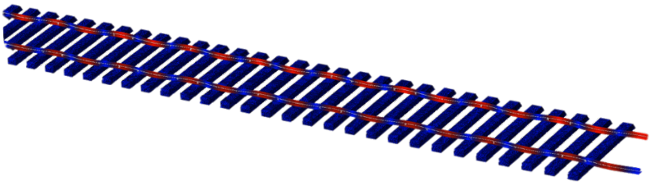

Fig. 5.28: The second modal shape showing the resonance where rails vibrates on the rail pads, it is found at a frequency of 212.3 Hz.

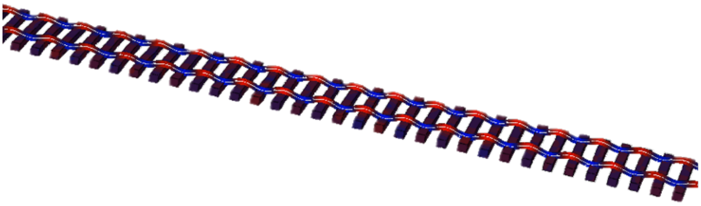

Fig. 5.29: The third modal shape showing the pin-pin resonance where the rails bend between the sleepers, is found at a frequency of 1058.2 Hz.

5.3.4 Comparison of 3D Models

In this section, a comparison between the two 3D models is conducted. This comparison is to study the effect of utilizing solid elements for both rail and rail pad instead of beam elements and spring/dashpot features. To compare the models, they need to have the same features

The properties found in Subsection 5.3.2 are also employed in the 3D solid model. However, the rail pad has different properties in the 3D solid model than the 3D beam model. Thus, the properties of the solid rail pad must be defined. It is assumed in the 3D solid model that the rail pad exhibits linear elastic properties, in which the density, damping, Young's modulus, and Poisson's ratio must be found. Based on the Pandrol 10 mm studded rail pad, the density and Poisson's ratio are 400 kg/m^3 and 0.4, respectively. Young's modulus and the damping properties of the rail pad are found through an iterative process to fit the static and dynamic properties of the 3D beam model, presented in Fig. 5.30 and Fig. 5.31, respectively.

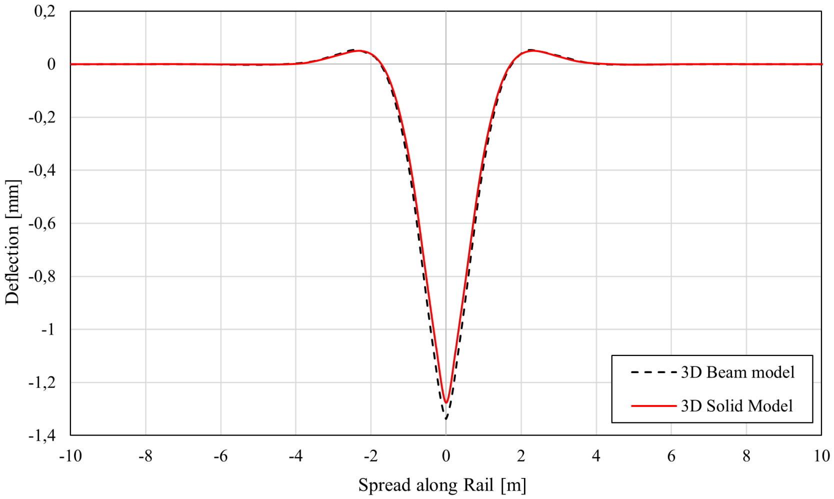

Fig. 5.30: Comparison between deflection curve of 3D solid model and 3D beam model

The Young's modulus was found to be 7.5 MPa, resulting in a deflection of 1.28 mm. The damping properties of the rail pad are found by altering the Rayleigh damping coefficients in Abaqus and comparing the receptance curves of the 3D beam model with the 3D solid model. Because the damping properties of the rail pad influence the dynamic response in the mid-frequency and high-frequency range, the dominant Rayleigh coefficient is β. Some disturbance in the frequency range of 400 to 1000 Hz was observed. Therefore, after some trial and errors, the Rayleigh coefficients are equal to α = 21 and β = 0.00023.

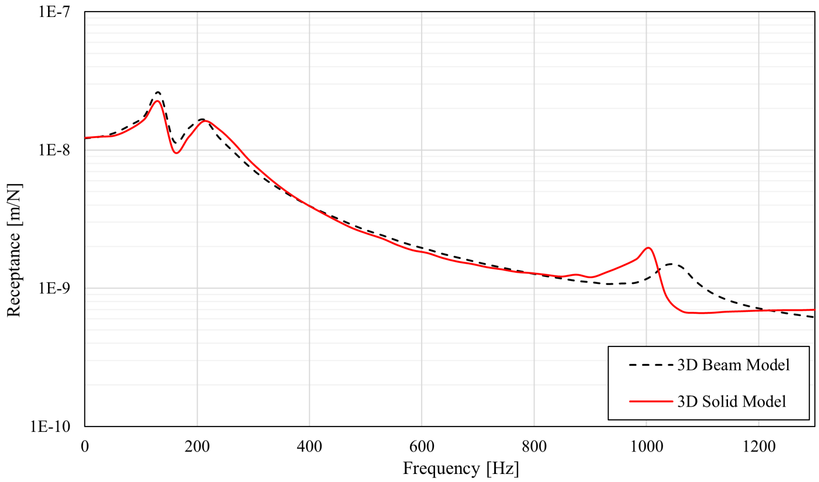

Fig. 5.31: Comparison between receptance curve of 3D solid model and 3D beam model

From the mesh convergence study, described in Subsection 5.2.2, the total number of elements found for the 3D solid model is compared with the 3D beam model, as shown in Table 5.7.

Table 5.7: Number of elements meshed on each part in the 3D beam model and 3D solid model, including total number of elements in the whole model considering 2 rails, 128 rail pads and 64 sleepers.

	Number of Elements	
Part	**3D Beam Model**	**3D Solid Model**
Rail	3951	91224
Rail Pad	-	80
Sleeper	5360	5360
Ballast	160580	160580
UBM	16200	16200
Total in Model	527722	712508

Thus, the static and dynamic analyses of both models showed a significant increase in CPU time for the solid model, shown in Table 5.8. This behavior is expected as it has more elements than the 3D beam model. Thus, because the 3D beam model has a lower CPU time compared to the 3D solid model, it will be used for further analyses.

Table 5.8: Average CPU time, presented in seconds, for each analysis completed for 3D beam model and 3D solid model.

Analysis	**3D Beam Model**	**3D Solid Model**
Static	2763.7	2770.9
Dynamic	40878	70181

5.4 Properties of UBMs

The material properties of the UBMs must be determined to analyze their effect on the track response. Based on data sheets provided by Bane NOR, the stress-strain curves of each UBM are found, as shown in Fig. 5.32.

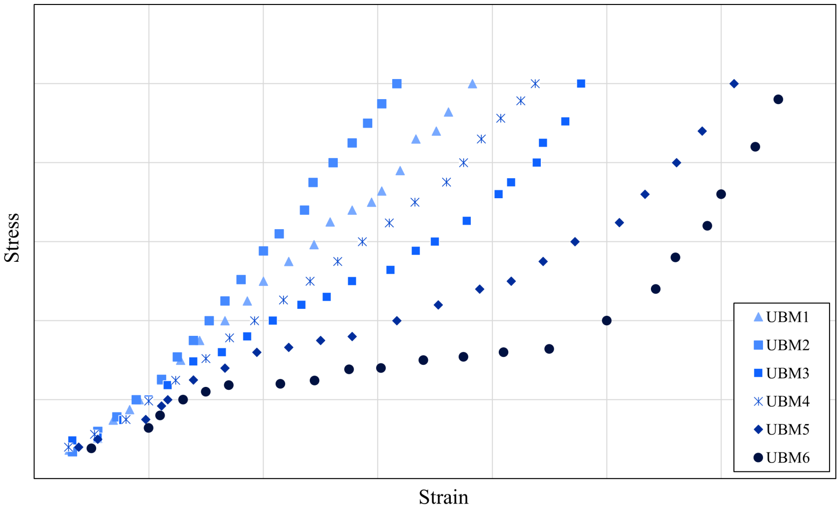

Fig. 5.32: Stress versus strain curve for UBMs

The stress-strain curves are obtained from compression tests of UBMs with specified geometrical dimensions. Previously it was common to conduct such tests with flat plates (FP) according to EN standards, but presently tests are performed using a geometric ballast plate (GBP). The GBP is a profiled steel plate with several raised nodes arranged in a symmetric grid to replicate the contact between ballast particles and the UBM.

The shape of the stress-strain curves demonstrates that the behavior of the UBMs are non-linear and resembles that of hyperelastic materials. The hyperelastic behavior depends on the type of strain energy potential, and the types available in Abaqus are Arruda-Boyce, Mooney-Rivlin, Marlow, Neo Hooke, Ogden, Polynomial, Reduced Polynomial, and Yeoh. Abaqus permits the evaluation of the optimal fit between the mentioned definitions and the input data. The evaluation determines which strain energy potential definition results in a stable solution; the Marlow definition is the most stable.

Further, the thickness and density were determined based on dimensions and weight provided in the datasheets. Since Poisson's ratio of the UBMs are not specified, it is determined to be 0.35. The damping properties of the UBMs are determined based on the Rayleigh damping definition, in which the lower frequency range is chosen. The damping ratio is determined based on the loss factor of one UBM and is found to be 6%. The frequency range is equal to that of the ballast; [125,1885] (rad/s), from Table 5.5 in Subsection 5.3.2. Thus, utilizing Equation 3.17 and Equation 3.18, the damping coefficients were found to be α = 14.07 and β = 5.97·10^{-5}. The secant modulus of the stress-strain curves, density, and thickness of each UBM are presented in Table 5.9.

Table 5.9: Secant modulus of measured stress-strain curves for different UBMs, including the input parameters, density and thickness, in Abaqus.

Name	**C [N/mm^3]**	**ρ [kg/m^3]**	**t [mm]**
UBM1	0.035	372	18
UBM2	0.047	372	18
UBM3	0.026	339	18
UBM4	0.028	325	20
UBM5	0.019	350	18
UBM6	0.0085	215	83

6

Results and Discussion

The results from the static and dynamic analyses are presented in this chapter. The analyses were carried out to observe the response of the 3D beam model by altering parameters of the rail pads and the ballast layer. Further, the main objective is to analyze statically and dynamically how an additional elastic component, the UBM, affects the response. The validated 3D beam model from Subsection 5.3.2 is utilized as a benchmark for all analyses in this section, and will henceforth be referred to as the 3D model.

6.1 Beam on Discrete Support Model

Two analyses were conducted to examine the response of the 3D model: Static analysis with a single axle loading condition, and steady-state dynamic analysis. The ballast thickness and rail pad stiffness were altered to assess the influence on the static and dynamic response of the track.

6.1.1 Effect of Ballast Thickness

There are regulations governing the thickness of the ballast, which varies depending on the track's location. From Section 2.4, the ballast height must be at least 30 cm and should not exceed 70 cm. The 3D model was modeled with a ballast thickness of 40 cm, which is the standard when utilizing 60E1 rails and concrete sleepers. The thickness of the ballast was increased to 50 and 60 cm to observe the effect, as seen in Fig. 6.1.

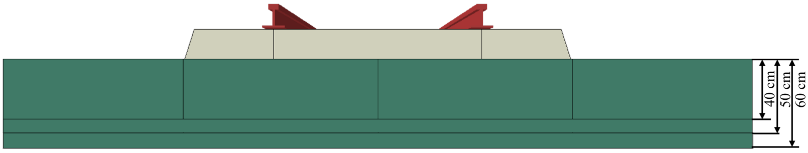

Fig. 6.1: Change of ballast thickness from 40 cm to 50 cm and 60 cm.

It is evident from the deflection curve, shown in Fig. 6.2 that there is not a significant increase in the deflection of the rail as the thickness of the ballast layer increases. The original track, with a ballast thickness of 40 cm, showed a rail deflection of 1.338 mm. With 50 cm and 60 cm thick ballast, the deflection becomes 1.355 mm and 1.381 mm, corresponding to 1.93% and 3.21% increased deflection, respectively. It is also observed that the upward-lifting of the rails increases with increased ballast thickness, yielding 7.64% and 12.3% increase in uplift with 50 cm and 60 cm, respectively.

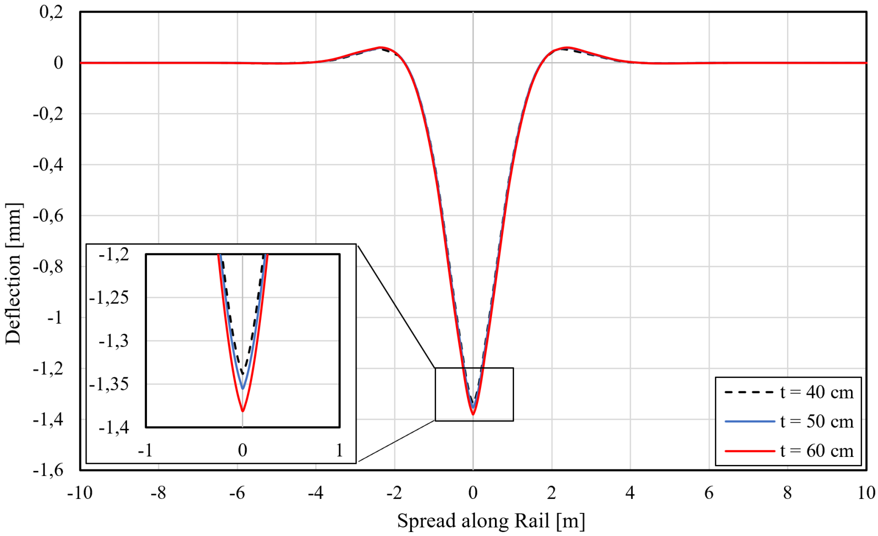

Fig. 6.2: Deflection curves from changing the ballast thickness from 40 cm to 50 and 60 cm, with a point load of 110.4 kN.

Even though the deflection of the rail appears to be minor, these changes in the ballast thickness could still affect the dynamic response of the track. As observed in Fig. 6.3, the first resonance is shifted towards the left, which indicates that the overall track stiffness is reduced in both cases. The receptance curves shows a shift of the first peak from 132.65 Hz to 106.12 Hz, while the second peak is shifted from 212.24 Hz to 185.71 Hz. The third peak remains the same regardless of an increase in ballast thickness.

Therefore, the first and second resonance peaks are shifted by the same amount towards lower frequencies, but the amplitudes of the resonance peaks are different in the two cases. It is observed that the first peak has a lower amplitude when the ballast thickness is 60 cm than 50 cm but has a higher amplitude on the second peak. This implies a lowered damping of the second resonance frequency. Because the stiffness of the ballast layer is reduced due to increased thickness, the second vibration mode is amplified. From Subsection 5.3.3, this means that the sleepers will vibrate more freely on top of the ballast layer.

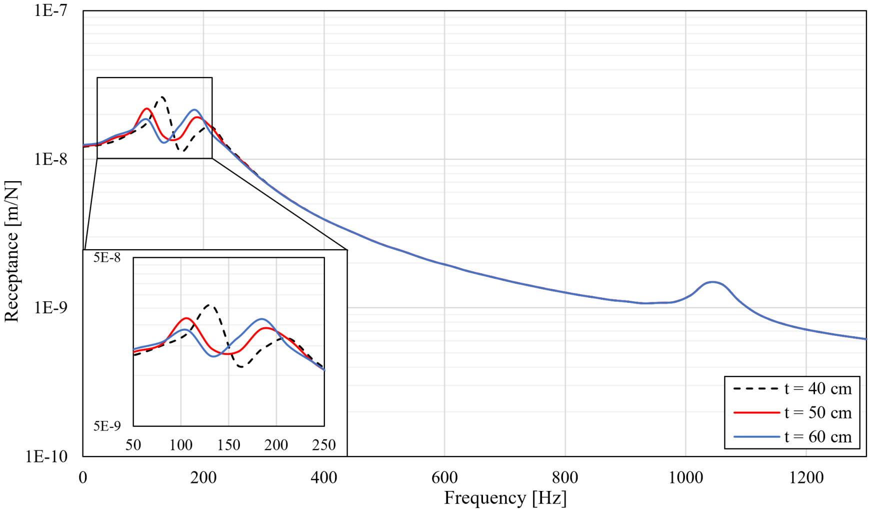

Fig. 6.3: Receptance curves obtained with different thicknesses of the ballast layer.

6.1.2 Effect of Rail Pad Stiffness

The rail pad stiffness were increased and decreased with ± 19 MN/m. The static analysis, presented in Fig. 6.4, shows that increasing the rail pad stiffness affects the overall stiffness more than when the stiffness is reduced. According to the deflection curve, the maximum deflection with a stiffness of 70 MN/m resulted in a deflection of 1.147mm. In contrast, the maximum deflection with a stiffness of 31 MN/m resulted in a deflection of 1.731 mm.

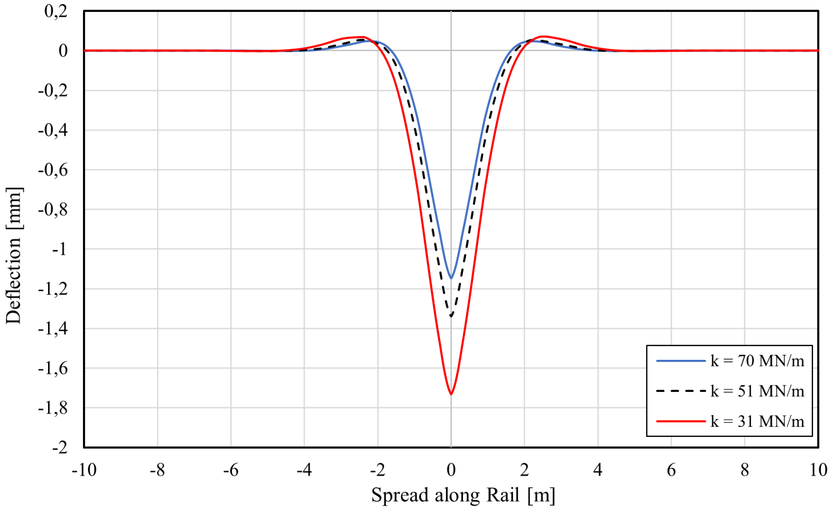

Fig. 6.4: Deflection curves from changing the rail pad stiffness to 31 MN/m and 70 MN/m.

The curves indicate a 14.3% decrease and 29% increase in rail deflection with a rail pad stiffness of 70 MN/m and 31 MN/m, respectively. Therefore, it is reasonable to state that reducing the rail pad stiffness has a higher effect on the overall track stiffness than increasing it. The rail also experiences an uplift as the stiffness decreases, indicating that the rail experiences increased bending due to more flexible rail pad while being constrained to the sleepers. The deflection curves also become broader with decreasing rail pad stiffness, indicating that the load will be distributed onto more sleepers.

In addition, a dynamic analysis was undertaken with the various rail pad stiffnesses. The results are presented as receptance curves in Fig. 6.5. The variation of rail pad stiffness affects the amplitude of the resonances. It is especially an increased amplitude at the first resonance frequency when the stiffness is reduced to 31 MN/m at 132 Hz. It also shows that the second resonance peak is almost diminished at 185 Hz, while when the stiffness is increased to 70 MN/m, the second peak is amplified and broader. This indicates that the soft rail will have a dominating damping effect as the stiffness is reduced, which prevents transferring of anti-phased vibrations between the rail and the constrained sleeper. Conversely, the first resonance frequency is increased due to in-phase movement of the rail and sleeper, and the dampening effect of the rail pad becomes less efficient.

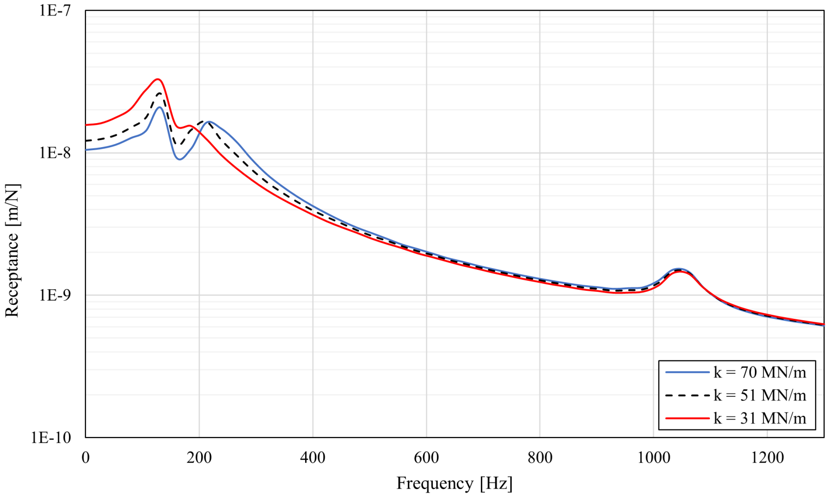

Fig. 6.5: Receptance curves obtained with different stiffnesses of rail pad.

The pin-pin resonance frequency is not significantly affected by the variation of the rail pad stiffness. Although, it is observed that the amplitude of the pin-pin resonance increases with increasing rail pad stiffness. This is the frequency at which the rail becomes decoupled from the supports, and with higher track stiffness, the dynamic response of the track will become more prominent.

6.2 Beam on Discrete Support including UBM

In this section, the main objective is to incorporate an additional elastic component in the 3D model. The properties of the UBMs were found in Section 5.4. The following analyses with various UBMs were conducted: static analysis with single and multiple loading conditions, stress analysis of ballast and steady-state dynamic analysis.

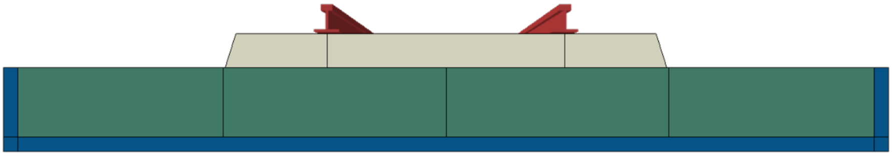

Fig. 6.6: Cross section of the 3D model, including UBM6, from Abaqus.

6.2.1 Static Analysis

The resulting deflection curves of the rail with various UBMs included in the 3D model, are presented in Fig. 6.7. The overall stiffness of the track reduces significantly when the stiffness of the UBMs reduces. The maximum deflection is found with UBM6 yielding a deflection of 2.58 mm, which is a great increase compared to the deflection without UBM of 1.33 mm. The track stiffness including UBM6 is therefore considerably reduced compared to the situation without any UBM.

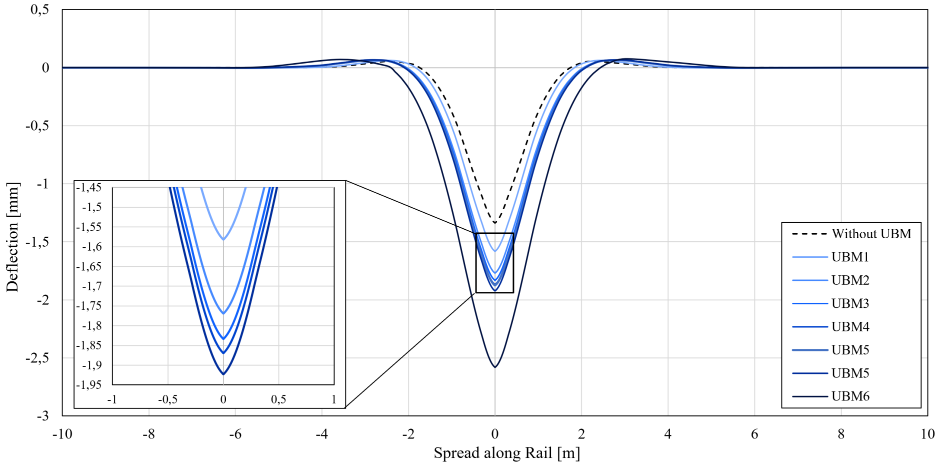

Fig. 6.7: Deflection curves from static analysis with all UBMs ranging from stiff (UBM1) to soft (UBM6), loaded with a static point load corresponding to the maximum axle load exerted by a Stadler FLIRT 75 train of 110.4 kN.

From Section 2.5, Bane NOR recommends that the rail deflection is less than 2 mm and never more than 3 mm. The majority of the analyzed UBMs were within the limit of 2 mm, but UBM6 stands out with its 0.58 mm excessive deflection. It is also observed from UBM3 and UBM4 that even though UBM4 has a higher secant modulus than UBM3, the increased thickness can still contribute to increased deflection. Thus, the thickness of the UBMs also influences the resulting rail deflection. The deflection curves also show that the rail experiences some increased upward lift with decreasing stiffness of the UBMs. In addition, they show the same tendency of increased breadth with decreasing stiffness, indicating that the load will be transferred onto more sleepers as the stiffness decreases.

Multiple Axle Loads

The rail deflection depends not only on the stiffness of the track but also on the spacing between axles. Thus, it was essential to consider the response of the rail with multiple axle loads. the train is often composed of one or more locomotives and several wagons, leading to several wheel loads being loaded on the rail during passage. The wagons are placed on multiple bogies, which carry a wheelset. The wheelset creates the contact between the vehicle and the rail, which will further transfer loads through the super- and substructure.

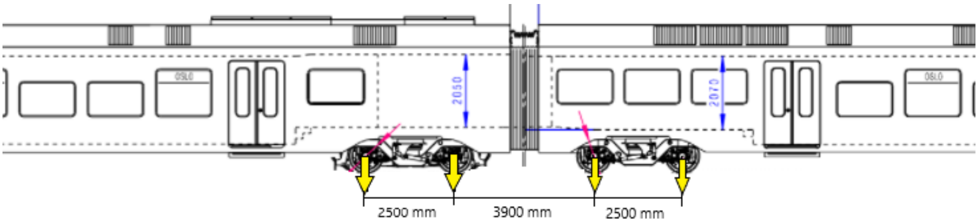

Fig. 6.8: Critical part of FLIRT 75 train with highlighted axle loads and distances between wheels. Bogie MB4 is shown on the left hand side, while TB3 is shown on the right hand side.

Multiple loads from a Stadler FLIRT 75 train, from Subsection 3.4.1, were used to investigate the response. A comprehensive layout of the FLIRT 75 train is presented in Section A.1. For this purpose, the most critical section of the train was modeled in Abaqus, which is the section including the MB4 and TB3 bogies. It was considered the most critical part due to less spacing between the bogies compared to the other ones. The wheel-base, which is the distance from the centre of each wheel on a bogie, was fixed at 2.5 m for both MB4 and TB3. The distance between the adjacent wheels (front axle on MB4 and back axle on TB3) on each bogie was 3.9 m. The axle load from each bogie is given in Section A.2, and was divided by two since only half of the track was considered. The system being investigated is illustrated in Fig. 6.8.

The applied load was found to be 95 kN and 80 kN for each wheel load on MB4 and TB3, respectively. The static response with multiple axle loads were analyzed with and without UBMs. By applying these loads with the specified distances, the resulting maximum deflections with various UBMs are presented in Fig. 6.9.

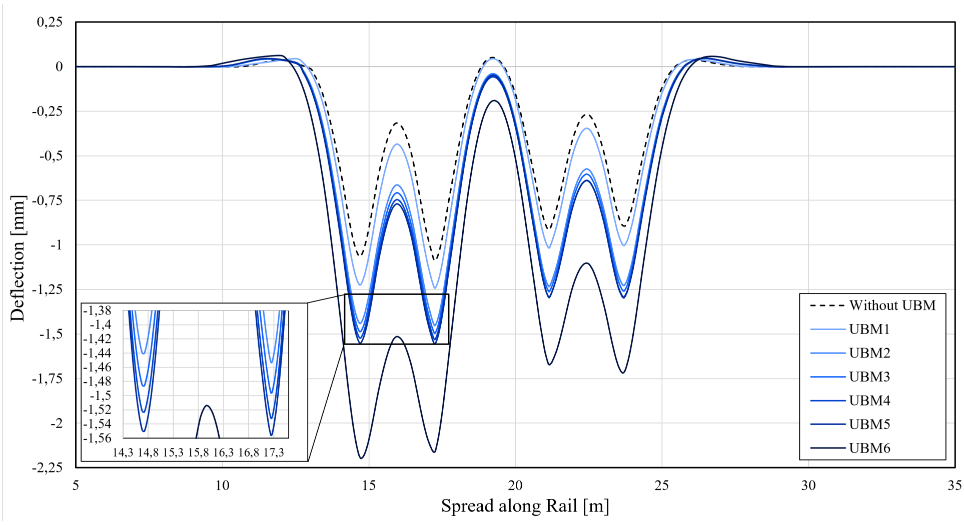

Fig. 6.9: Deflection curve with multiple loads from bogie MB4 and TB3 of a Stadler FLIRT 75 train, including all UBMs ranging from stiff (UBM1) to soft (UBM6)

The results showed that the softer UBM, UBM6, causes an overall deflection of the rail when both bogies are used, which indicates that the rail deflection between each wheelbase will not fully recover to its at-rest state. It was also evident that the upward lift between adjacent wheels on each bogie decreases with decreasing stiffness of the UBM. This behavior can also lead to decreased recovery of the rail and increased interaction between adjacent wheels on each bogie. The deflection curve of the UBM6 was also much broader than the rest, indicating that the load will be distributed over more sleepers.

It is highly likely that the adjacent wheels will influence each other, which is evident from the deflection curve, shown in Fig. 6.10. In this case, UBM6 were chosen due to its impact on the reduced track stiffness. The deflection curves from the individual axle loads tend to overlap, which indicates that the loads influence each other. It is seen from the deflection curve that the front axle of TB3 does not affect the back axle of MB4. However, the back axle of TB3 has minor effects on the back axle of MB4. This can be seen by the increased deflection of the front MB4 axle compared to the back axle of MB4. In addition, the overall deflection of the rail with UBM6 indicates that each axle load generates less rail deflection compared to both bogies being loaded onto the track. Such effects should be taken into account when evaluating the track stiffness.

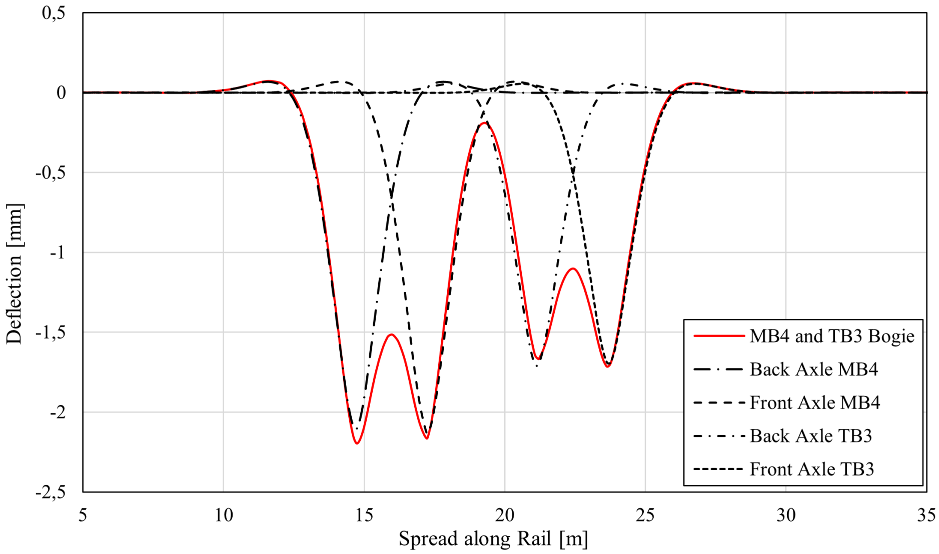

Fig. 6.10: Deflection curves of rail with UBM6. Dashed lines indicate a single point load from either bogie MB4 or TB3, while the red solid line is the total deflection when both bogies are loaded on the track.

Stress Analysis of Ballast

The ballast layer was subjected to a stress analysis to determine how the transmitted load was distributed when various UBMs were included in the model. For this analysis, three UBMs varying from stiff to soft were utilized. The selected UBMs were UBM1, UBM5, and UBM6. A cross-section of the ballast layer, including the sleeper, were analyzed to examine the track's stress distribution. The extracted cross-section was located beneath the position of the applied load to impose maximum pressure on the interface between the sleeper and the ballast. The cross-section of the ballast with various UBMs is depicted in Fig. 6.11. The situation without any UBM were used as a benchmark.

It is evident from Figures 6.11a to 6.11d that the decreasing stiffness of the UBMs lead to an increased stress distribution. This tendency indicates that the loads are more distributed throughout a greater area of the ballast layer. As mentioned in Section 3.4, the measured pressure exerted on the ballast does not exceed the limit of 0.3 MPa, regardless of the type of UBM included in the track model, as seen in Figures D.1 to D.4. It is also observed that the increased stress distribution angle results in an increased overlap of the stresses from each sleeper, which indicates that the spacing between the sleepers also will experience less stress, as seen in Figures C.1 to C.4. Additionally, when the track stiffness decreases, the adjacent sleepers experiences an increase in edge stress. This can originate from the increased flexibility of the track inflicting the sleepers to rotate.

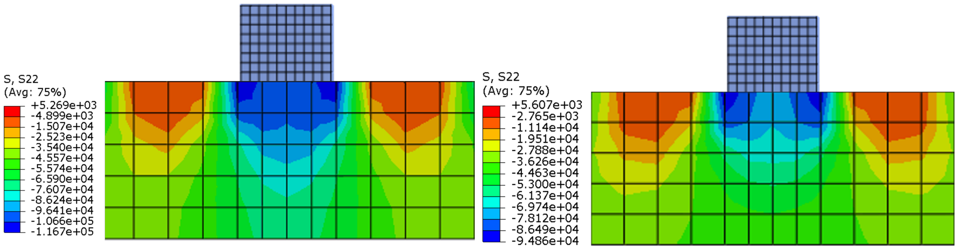

(a) Without UBM **(b)** UBM1

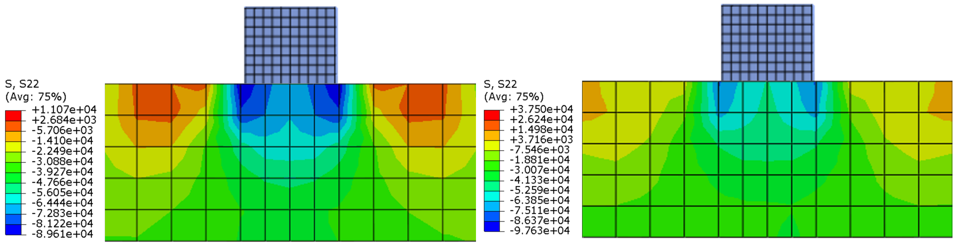

(c) UBM5 **(d)** UBM6

Fig. 6.11: Vertical stress distribution in the ballast layer. The measured stress are presented in Pascal, [Pa].

6.2.2 Dynamic Analysis

Dynamic analyses of the 3D model with different UBMs are presented in this section to understand how the they affects the dynamic response of the track. The receptance curves of the model with different UBMs, ranging from stiff (UBM1) to soft (UBM6), are presented in Fig. 6.12. The receptance curves, including UBMs, were extracted with harmonic excitation of the rail, as explained in Subsection 4.3.3, and compared with the receptance curve without UBM, shown in Fig. 5.25. Because the model consists of non-linear elements, a preload step was superimposed to the dynamic load in Abaqus. The preload was applied statically and then dynamically of the same magnitude, corresponding to the maximum axle load of the Stadler FLIRT 75 train of 110.4 kN.

As observed in Fig. 6.12, three prominent peaks indicate different resonance frequencies. The resonance frequencies extracted from the curves are presented in Table 6.1. It is evident from the results that the modal response of the track is shifted towards lower frequencies as a result of decreased stiffness. The curves also tend to shift towards higher receptance values due to the increased dynamic flexibility of the track. This behavior verifies that the resonance frequencies are enhanced vibration modes owing to compliance with the inherent frequencies of the structure. From the receptance curves, it is observed that the first and second resonance frequency of the track is significantly shifted towards lower frequencies compared to the situation without UBM. It is also observed that the receptance increases with decreasing stiffness of the track structure below the first resonance frequency, which is the region where stiffness affects the system's response.

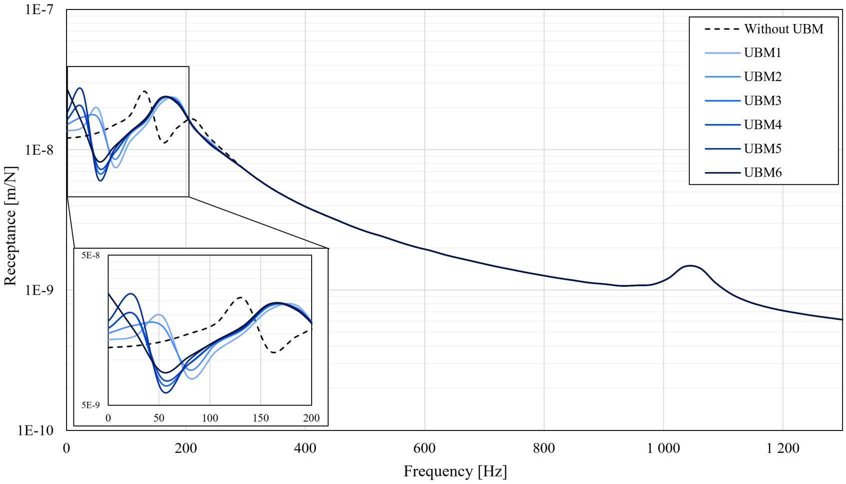

Fig. 6.12: Measured receptance curves of all UBMs ranging from stiff (UBM1) to soft (UBM6), loaded with a harmonic sinusoidal load with a circular frequency of 2π.

Table 6.1: The resonance frequencies derived from the various receptance curves for each UBM.

Type of UBM	Mode 1 [Hz]	Mode 2 [Hz]	Mode 3 [Hz]
Without UBM	132.7	212.4	1034.7
UBM1	53.1	185.7	1034.7
UBM2	53.1	174.3	1034.7
UBM3	25.4	173.7	1034.7
UBM4	25.4	173.7	1034.7
UBM5	25.4	173.7	1034.7
UBM6	10.2	173.7	1034.7

The various UBMs generate different magnitudes and shapes of the first resonance frequency. At this resonance frequency, the rail and sleepers are vibrating in phase, as discovered in Subsection 5.3.3, and the track structure below these components of the track determines the response. Therefore, it is clear that the UBM will have the greatest influence on the overall track response in this frequency range. According to the receptance curves, the first resonance frequency amplitude decreases with UBM1 and UBM2 while increasing with UBM3, UBM4, UBM5, and UBM6. This behavior indicates that UBM1 and UBM2 have a more damped amplitude than the other UBMs. UBM5 and UBM6 are less damped, which may originate from the track becoming too soft, causing the ballast to vibrate on top of the UBM.

The receptance curve for UBM3 and UBM4 has resonance frequencies that coincide, except at the anti-resonance frequency. The anti-resonance between the first and second resonance frequency results from the sleeper mass and rail pad stiffness forming a resonant system in which the energy is absorbed from the rail. This behavior increases with decreasing stiffness of the UBMs, except for UBM6, which is the softest UBM. Another aspect that can influence this behavior is the thickness of the UBMs. The thickness of both UBM4 and UBM6 differ from the remaining UBMs. The anti-resonance may further exemplify this tendency between UBM3 and UBM4, which have almost identical properties and behave similarly in their static and dynamic response, except for their thickness.

Further, the second and third resonant frequency is an explicit function of the rail and rail pad characteristics and depends on the track components' damping properties and masses. It is evident from the curves that the UBMs dampen the second resonance peak by its increase in breadth and lowered amplitude, indicating that the resonance will have an effect over a more extensive range of frequencies. All simulations with various UBMs tend to attain the pin-pin resonance frequency of around 1034.7 Hz. This behavior is reasonable due to the origin of this type of resonance. It mainly depends on the mass and damping of the rail, which is independent of the remaining structure. Therefore it is clear that the UBMs influence the dynamic properties of the track predominately below 200 Hz, which is within the spectrum of emerged ground-borne noise from train traffic. The effectiveness of the UBMs is important in this range as these low-frequency vibrations can strongly stimulate the surrounding environment. However, the results also show that high deflections are generated in this range as the resonance frequency amplitude increases with decreasing stiffness of the UBM.

6.3 Further Discussion of Study Cases

The static response of the track, from Fig. 6.7, is also closely related to the dynamic response, presented in Fig. 6.12. The section of the curves before the first peak is the range which is dependent of the stiffness of the track. Because the receptance curves are the inverse of track stiffness, the receptance measured at zero frequency will be the experienced deflection under static loading. Therefore, it is clear from Fig. 6.12 that the track will experience an even greater deflection under dynamic loading conditions if a resonant frequency is excited.

It is known that a railway track is not perfect. There will be variations in the track, especially regarding the stiffness. The sleepers will, most likely, not be placed perfectly with a spacing distance of 0.6 m. In addition, the rails will experience some degradation over time, especially from the wheel-rail contact. Consequently, the rail can develop corrugation on the railhead or have vertical irregularities. The frequency of such corrugations can be found by Equation 3.14. Considering the maximum speed of a Stadler FLIRT 75 train of 200 km/h and the corrugations having a wavelength of 300 mm, the corrugation-passing frequency is equal to 185.3 Hz. From Fig. 6.12, it is evident that the second resonance frequency of the track can easily be excited with a soft UBM (UBM6) while having such irregularities in the track.

The sleeper distance is also an important factor, as this determines the motion of the moving vehicle. This stiffness variation can cause the train to oscillate vertically as it travels over the track at a certain speed, thus passing the sleepers at a particular frequency. This motion will be enhanced if the track stiffness is reduced and can affect the so-called sleeper passing frequency, mentioned in Subsection 3.3.1. Utilizing Equation 3.15 with the maximum train speed of a Stadler FLIRT 75 train of 200 km/h, the sleeper-passing frequency equals 92.6 Hz. From Fig. 6.12, this frequency lies between the first and second resonance frequency when the UBMs are included in the model. Even though the sleeper-passing frequency differs from the second resonance frequency of the 3D model, including UBMs, it can still affect the overall response of the track. This effect originates from the track having a more significant fluctuation in stiffness between the anti-resonance frequency and the second resonance frequency. Consequently, the track can experience excessive oscillation if excited close to the resonance frequency. The dominating vertical vibration mode of the track could then amplify the anti-phase vibrations of the sleepers and rails.

Multiple factors can affect the dynamic response of the track. For instance, multiple axle loads from a moving train will cause waves of vibrations to propagate along the track. If the track stiffness is low, as seen in Subsection 4.3.1, the track can experience non-recoverable deflection, such as the case with UBM6. The subsequent passing bogie or axle load could then be exposed to an even greater dynamic impact due to non-alignment. This effect can enhance the possibility of exciting one of the resonant frequencies of the track.

Additionally, all materials have natural frequencies, also the ones included in the railway track. Therefore, it is imperative to be aware of their natural frequencies to avoid situations where these can be excited. If the frequency of a component's oscillation occurs at its natural frequency without sufficient damping of the amplitude, it might, over time, surpass the component's fatigue limit. Detrimental components, such as the fastening system, can be more vulnerable under such circumstances and should be avoided.

6.3.1 Uncertainty of Numerical Modeling Procedure

The boundary conditions were applied the in horizontal and vertical directions assuming that the railway track was located on a tunnel floor consisting of concrete walls. In reality, the superstructure of the track will be confined to a concrete ground whose properties can act differently than the ones defined in Abaqus. Thus, the structural absorption of dynamic loading conditions can be more present if defining proper ground properties.

There are uncertainties regarding utilizing a 2D model as a benchmark for validation of the 3D beam model. For instance, numerical models are usually calibrated based on experimental or field data. Additionally, due to the lower complexity and solver time associated with 2D modeling, they are often calibrated against more complex and accurate 3D models. Because there was a dearth of experimental or field data for the models created in Abaqus, a 2D model was calibrated based on the Zimmermann method and then utilized as a benchmark for the 3D beam model. As previously stated in Section 3.2, the Zimmermann method is an analytical technique that is still commonly used for simple analyses and calibrations. Even though the 3D beam model is more complex than the proposed 2D model, it was still beneficial to calibrate and validate it against a 2D model rather than the Zimmermann method. This was mainly done because the Zimmermann method does not consider the dynamic responses of a track structure.

Several factors can account for the disparities between the 3D beam model and the 2D model, presented in Subsection 5.3.2. The assumptions made during calibration of the 2D model against the Zimmermann method can cause ripple effects. For instance, the type of elements and boundary conditions applied in the 2D model is different from the ones assumed in the Zimmermann method. Poisson's ratio was also considered in the 2D model, which is not included in the Zimmermann method. Zimmermann's method also considers a rail on continuous support, while the rail rests on discrete support in the 2D model. The discrete support was also in contact with solid elements, which can influence the contact stiffness differently than assumed in Zimmermann's method.

The ballast and sleepers in the 3D beam model had different dimensions, geometry, and element types than the ones in the 2D model. In the 2D model, the ballast and sleeper have a plane stress/strain thickness equal to 1, while they have out-of-plane dimensions in the 3D beam model. This can cause increased stiffness in the elements as they have advanced degrees of freedom and can experience rotation in the 3D beam model. These differences between the models can also cause the damping properties and the masses of the track components to be not practically the same, which can change the amplitude and frequency of the indicated peaks.

There are also some uncertainties regarding the convergence study of the 3D beam model, as the sleepers did not converge. It is assumed that the rail pads act as point loads, in which the transferred load is maximized onto one node of the sleeper. This behavior leads to penetration of the elements on sleepers, rather than spreading the transferred load. Therefore, it is uncertain if some of the measured deflections could originate from mesh deformation. This behavior was not observed in the 3D solid model, which can confirm the assumption of the rail pad penetrating the elements of the sleepers. The sleepers did experience convergence in the 3D solid model, possibly due to having solid rail pads which distributes the transferred load more evenly.

Further, the 3D solid model showed compliance with the 3D beam model from the static analysis, with minor differences. However, the 3D solid model shows some deviation in the dynamic response compared to the 3D beam model. From the receptance curve of the 3D solid model, it is observed that the first resonance frequency has a lower amplitude than the 3D beam model. The second resonance frequency seems to reach the same amplitude as the 3D beam model, but the peak is broader for the 3D solid model. The first resonance frequency is closely linked to the overall track behavior. By utilizing solid elements, it is possible that the solid elements of the rail dampen more than the beam elements. The pin-pin resonance clearly shows different behavior for the 3D solid model than for the 3D beam model. This difference can originate from the fact that this frequency range is mainly influenced by the properties and masses of the rail. Since the rail design is different from the 3D solid model, this will significantly impact the response.

All parts in the model are simplified compared to a realistic track design to reduce the complexity and run time. Abaqus is very sensitive to complex geometry which can lead to failed analysis checks and aborted simulations. For instance, the ballast layer is modeled as a continuous layer, but in reality, it contains discontinuities caused by nonuniform rocks, as mentioned in Section 2.4. This causes significant uncertainty regarding the behavior of the ballast layer. To capture a more precise behavior, the mesh size of the ballast layer could be altered to achieve a stress distribution corresponding to experimental measurements compared to the distribution found in 6.2.1. Additionally, the material properties of the UBMs are defined as hyperelastic materials, which is an approximate solution to their actual behavior. It is possible to define the material properties of the UBM as hyperelastic or as a hyperfoam in Abaqus. The best definition of the UBM would be hyperfoam due to their high tolerance during compression. However, the necessary input data for assigning hyperfoam behavior to the UBMs were unavailable. Thus, the generated stress-strain graphs were used as hyperelastic uniaxial test data for each UBM in Abaqus.

7

Concluding Remarks and Future Research

The aim of this thesis was to analyse the static and dynamic response of including UBMs in a ballasted railway track, by utilizing a numerical approach in Abaqus. Conclusions based on the results and suggestions for future research are presented in this chapter.

7.1 Concluding Remarks

Two different models were created for the problem studied in this thesis, one with only solid elements and another with rails having beam elements and rail pad as spring and dashpots. Each model underwent a mesh convergence study, including recordings of measured CPU time. All parts in both models tended to converge, except the sleepers in the 3D beam model. It was found that springs and dashpots connected between rail and sleeper induce a concentrated point load onto the sleeper. Thus, some of the transferred load becomes absorbed at the connecting node rather than transmitted further into the structure. Conversely, the sleepers in the 3D solid model reached convergence when the rail pad was modeled with solid elements. Additionally, both models required almost the same CPU time when running static analysis, but the 3D solid model demanded approximately 70% more CPU time than the 3D beam model during dynamic analysis. The simulations are time-consuming, and therefore the 3D beam model was chosen as the primary model for further static and dynamic analyses.

The calibration method used for the 3D beam model is based on analytical solutions of the Zimmermann method. Usually, calibration is done based on experimental or field data, which was unavailable for the modeling procedures. Therefore, some of the assumptions made in the models can cause uncertainty, especially regarding boundary conditions, interactions, and material properties. This applies especially to the material properties of the ballast and the UBMs.

The UBMs are soft and contribute to reducing noise and vibrations, but they increase the deflection of the rail. From the regulations set by Bane NOR, the deflection of the rails should not exceed 2 mm, and the maximum deflection limit is 3 mm. None of the simulations with UBMs resulted in a deflection of 3 mm, but UBM6 (the softest UBM) showed a deflection of 2.58 mm, which is excessive deflection according to the recommendations. It was also found that multiple axle loads from bogies contribute to an increased deflection compared to single axle loads. Including UBMs in the track structure with multiple axle loads also showed that the axles from adjacent bogies (MB4 and TB3) will influence each other and lead to non-recovery of the original position of the rail.

A stress analysis was also conducted on the ballast to observe the stress distribution of the ballast. It was found that the maximum pressure exerted from the sleeper onto the ballast layer does not exceed the admissible limit of 0.3 MPa. Stress distribution of the railway track is essential, as smaller sections of the ballast will be susceptible to high stress if no distribution is present. However, from the stress analysis, the distribution does increase with decreasing stiffness of the UBM. Therefore, this behavior should be accounted for when resolving numerical and analytical solutions of track design.

Even though the static response does not exceed the maximum limits from regulations of Bane NOR, the dynamic response clearly shows that the rail deflection can be even more significant than the one found during static analysis. The track structure including UBMs mainly affected the first and second resonance frequencies compared to the benchmark without UBM. In particular, the UBMs shifted the resonance frequencies of the track towards lower frequencies, with the most prominent effect occurring below 200 Hz. This frequency is also within the frequency range of ground-borne noise and vibration. The shift of resonance frequencies can make the track more prone to resonate at known frequencies, such as corrugation- and sleeper-passing frequencies. A railway track is not perfect, making it even more exposed to resonate by external factors. It was found that the corrugation-passing frequency and the sleeper-passing frequency were within the first and second resonance frequency of the track when UBMs were included. This behavior can significantly impact both wear and fatigue limits of track components. Additionally, all parts of a track structure have natural frequencies, and if these are close to the resonance frequencies of the track, it could lead to failures if excited.

In conclusion, altering the elastic properties of track components or incorporating additional elastic components, such as the UBM, in a track structure will result in reduced track stiffness. Changing the ballast thickness has a minor effect on the static and dynamic behavior of the track compared to the rail pad and UBM. An assessment of the overall track response should be considered if multiple elastic parameters of a railway track are simultaneously modified, especially while considering loading conditions with multiple axle loads.

7.2 Future Research

- It would be advantageous to examine the influence of speed on the dynamic response. An explicit dynamic analysis can be undertaken in Abaqus by simulating moving loads to analyze the influence of train speed. This type of procedure enables the rail displacement to be analyzed and compared to the requirements for stiffness of the UBM at specific speed limits.

- Including imperfections in the model, such as corrugations or changes in sleeper spacing, should be performed to observe the amplifying effect of the vibration modes of the track structure while including UBM. Then it will be possible to compare the actual corrugation- and sleeper-passing frequency with the modeled track.

- Calibration of the numerical models should be based on acquired data from field measurements. These measurements can provide more accurate behavior of the track and should be performed with and without the UBM. In addition, experimental measurements should be conducted to acquire more material properties of the UBMs.

- An experimental study of the natural frequencies of the different components should be performed. If the track inhibits resonance frequencies coinciding with any of the components' natural frequencies, it could lead to failure.

- It would be more beneficial to conduct analyses of a 3D model with solid elements with a more complex design, as it could enhance the quality of the results. Increased complexity is time-consuming, and it would be more efficient to employ a supercomputer.

Bibliography

[1] Abaqus. About the element library, 2017. URL `https://abaqus-docs.mit.edu/2017/English/SIMACAEELMRefMap/simaelm-c-general.htm`.

[2] Abaqus. Direct-solution steady-state dynamic analysis, 2017. URL `https://abaqus-docs.mit.edu/2017/English/SIMACAEANLRefMap/simaanl-c-steadystdyndirect.htm`.

[3] Abaqus. Mode-based steady-state dynamic analysis, 2017. URL `https://abaqus-docs.mit.edu/2017/English/SIMACAEANLRefMap/simaanl-c-steadystdyn.htm`.

[4] Abaqus. Natural frequency extraction, 2021. URL `https://abaqus-docs.mit.edu/2017/English/SIMACAEANLRefMap/simaanl-c-freqextraction.htm`.

[5] Abaqus. Static stress analysis, 2021. URL `https://abaqus-docs.mit.edu/2017/English/SIMACAEANLRefMap/simaanl-c-static.htm`.

[6] C. Allison. Meshing in FEA: Mesh convergence — OnScale, 2020. URL `https://onscale.com/blog/meshing-in-fea-mesh-convergence/`.

[7] P. Alves Costa, R. Calçada, and A. Silva Cardoso. Ballast mats for the reduction of railway traffic vibrations. Numerical study. *Soil Dynamics and Earthquake Engineering*, 42:137–150, 2012. ISSN 02677261. doi: 10.1016/j.soildyn.2012.06.014.

[8] Bane NOR. KU Fagrapport Vibrasjoner og strukturstøy. Technical report, 2019.

[9] E. Berggren. *Railway Track Stiffness*. PhD thesis, Royal Institute of Technology (KTH), 2009.

[10] B. Blanco. *Railway track dynamic modelling*. PhD thesis, Royal Institute of Technology (KTH), 2017.

[11] T. Dagdelen and S. Ruhani. *Finite Element Analysis of the Dynamic Effect of Soil-Structure Interaction of Portal Frame Bridges-A Parametric Study TURGAY DAGDELEN SHAHO RUHANI KTH ROYAL INSTITUTE OF TECHNOLOGY SCHOOL OF ARCHITECTURE AND THE BUILT ENVIRONMENT*. PhD thesis, Royal Institute of Technology (KTH), 2018.

[12] P. E. Dalløkken. NSBs nye Flirt-tog i Norge - Tu.no, 3 2011. URL `https://www.tu.no/artikler/nsbs-nye-flirt-tog-i-norge/249823`.

[13] A. Damisie. *Analysis of Railway Track Stiffness Variation and Its Influence*. PhD thesis, Addis Ababa, 2015.

[14] A. P. De Man. Dynatrack: A survey of dynamic railway track properties. *Delft University of Technology, Delft, the Netherlands*, 2002.

[15] C. Esveld. *Modern railway track*. MRT-Productions, Duisburg, 2001. ISBN 9080032417.

[16] W. O. C. A. Group. Material Damping in Abaqus - CAE Assistant, 2020. URL `https://caeassistant.com/blog/material-damping-in-abaqus/`.

[17] J. Hjortland, M. Husum Malvik, and A. Lau. *Railway Engineering*. NTNU, Trondheim, 1 edition, 2021.

[18] S. Iwnicki. *Handbook of Railway Vehicle Dynamics*. CRC PRESS, 2006. ISBN 0-8493-3321-0.

[19] Jernbanekompetanse. Dimensjoneringsmetoder – Lærebøker i jernbaneteknikk, 2015. URL `https://www.jernbanekompetanse.no/wiki/Dimensjoneringsmetoder#Ballastsifferet`.

[20] S. . Kaewunruen, Chiengson, and Chatpong. Railway track inspection and maintenance priorities due to dynamic coupling effects of dipped rails and differential track settlements. *Engineering Failure Analysis*, 93(1350-6307):157–171, 2018. doi: https://doi.org/10.1016/j.engfailanal.2018.07.009. URL `https://doi.org/10.1016/j.engfailanal.2018.07.009`.

[21] D. Li, J. P. Hyslip, T. R. Sussmann, and S. M. S. M. Chrismer. *RAILWAY GEOTECHNICS*. CRC PRESS, 2019. ISBN 9780367866594. URL `https://www.routledge.com/Railway-Geotechnics/Li-Hyslip-Sussmann-Chrismer/p/book/9780367866594`.

[22] L.Pirozzolo. Optimization of bituminous sub-ballast in railways infrastructures under sustainability criteria — Semantic Scholar, 2017. URL `https://www.semanticscholar.org/paper/Optimization-of-bituminous-sub-ballast-in-railways-Pirozzolo/f821534ec67448a725a03c9b0acf0a4db6c8bf36`.

[23] A. Mosavi, R. Benkreif, and A. R. Varkonyi-Koczy. Comparison of Euler-Bernoulli and Timoshenko beam equations for railway system dynamics. *Advances in Intelligent Systems and Computing*, 660:32–40, 2018. ISSN 21945357. doi: 10.1007/978-3-319-67459-9{_}5.

[24] R. Muller. Mitigation Measures for Open Lines against Vibration and Ground-Borne Noise: A Swiss Overview. *Notes on Numerical Fluid Mechanics and Multidisciplinary Design*, page 8, 2008. doi: 10.1007/978-3-540-74893-9{_}37. URL https://www.researchgate.net/publication/328602489_Mitigation_Measures_for_Open_Lines_against_Vibration_and_Ground-Borne_Noise_A_Swiss_Overview.

[25] K. Nguyen, J. M. Goicolea, and F. Galbadón. Comparison of dynamic effects of high-speed traffic load on ballasted track using a simplified two-dimensional and full three-dimensional model. *Proceedings of the Institution of Mechanical Engineers, Part F: Journal of Rail and Rapid Transit*, 228(2):128–142, 2014. ISSN 09544097. doi: 10.1177/0954409712465710.

[26] A. Nordborg. Wheel/rail noise generation due to nonlinear effects and parametric excitation. *The Journal of the Acoustical Society of America*, page 11, 2002. doi: 10.1121/1.1459463. URL https://www.researchgate.net/publication/11367877_Wheelrail_noise_generation_due_to_nonlinear_effects_and_parametric_excitation.

[27] S. Ouakka, O. Verlinden, and G. Kouroussis. Railway ground vibration and mitigation measures: benchmarking of best practices. *Railway Engineering Science*, 30, 2021. doi: 10.1007/s40534-021-00264-9. URL https://doi.org/10.1007/s40534-021-00264-9.

[28] S. Pengajar, P. Fakultas, T. Unlam Banjarmasin, and P. B. Prakoso. The Basic Concepts of ModellingRailway Track Systems usingConventional and Finite Element Methods. *Info Teknik*, 13(1):9, 2012. URL http://www.arema.org/eseries/scriptcontent/custom/e_ar.

[29] N. Persson. *PREDICTING RAILWAY-INDUCED GROUND VIBRATIONS*. PhD thesis, Lund University, 2016. URL www.byggmek.lth.se.

[30] S. K. Railcorp and A. Remennikov. State dependent properties of rail pads. *Faculty of Engineering-Papers*, 11(2):8, 2009. URL https://ro.uow.edu.au/engpapershttps://ro.uow.edu.au/engpapers/494https://ro.uow.edu.au/engpapers/494.

[31] T. Regelverk. Overbygning/Vedlikehold/Skinner – Teknisk regelverk, 2021. URL https://trv.banenor.no/wiki/Overbygning/Vedlikehold/Skinner.

[32] T. Regelverk. Overbygning/Prosjektering/Ballast – Teknisk regelverk, 2022. URL https://trv.banenor.no/wiki/Overbygning/Prosjektering/Ballast#Profiler_p.C3.A5_hardt_underlag.

[33] T. Regelverk. Overbygning/Prosjektering/Ballast – Teknisk regelverk, 2022. URL https://trv.banenor.no/wiki/Overbygning/Prosjektering/Ballast#Krav.

[34] T. Regelverk. Overbygning/Prosjektering/Ballast – Teknisk regelverk, 2022. URL https://trv.banenor.no/wiki/Overbygning/Prosjektering/Ballast#Generelle_krav_til_ballastmatter.

[35] T. Regelverk. Overbygning/Prosjektering/Sporkonstruksjoner – Teknisk regelverk, 2022. URL https://trv.banenor.no/wiki/Overbygning/Prosjektering/Sporkonstruksjoner#Befestigelse.

[36] A. Rodrigues. Applicability of a Three-Layer Model for the Dynamic Analysis of Ballasted Railway Tracks. *Vibration*, 4(1):151–174, 2 2021. doi: 10.3390/vibration4010013.

[37] J. Sarah, F. Hejazi, R. S. Rashid, and N. Ostovar. A Review of Dynamic Analysis in Frequency Domain for Structural Health Monitoring. *IOP Conference Series: Earth and Environmental Science*, 357(1), 11 2019. ISSN 17551315. doi: 10.1088/1755-1315/357/1/012007.

[38] J.-Y. Shih. *Models for vehicle/track/ground interaction in the time domain*. PhD thesis, University of Southhampton, 2017.

[39] J. Y. Shih, D. J. Thompson, and E. Ntotsios. Analysis of resonance effect for a railway track on a layered ground. *Transportation Geotechnics*, 16:51–62, 9 2018. ISSN 22143912. doi: 10.1016/j.trgeo.2018.07.001.

[40] SSB. Flere reiste med tog i 2019 - SSB, 2019. URL https://www.ssb.no/transport-og-reiseliv/artikler-og-publikasjoner/flere-reiste-med-tog-i-2019.

[41] SSB. Flere utsatt for støy ved boligen - SSB, 2021. URL https://www.ssb.no/natur-og-miljo/artikler-og-publikasjoner/flere-utsatt-for-stoy-ved-boligen.

[42] D. Thompson. Railway Noise and Vibration. *Railway Noise and Vibration*, 2009. doi: 10.1016/B978-0-08-045147-3.X0023-0.

[43] E. Uhlig, C. Latal, M. Drrernat Holger Bach, and D.-I. Drtechn. *Effect of grain shape and petrographic composition of railway ballast on the Impact Test*. PhD thesis, Graz University of Technology, 2014.

[44] Unknown. Characterizing elements, 2022. URL https://abaqus-docs.mit.edu/2017/English/SIMACAEGSARefMap/simagsa-c-elmcharacterelm.htm.

[45] Unknown. Understanding Abaqus/CAE modules, 2022. URL https://abaqus-docs.mit.edu/2017/English/SIMACAEGSARefMap/simagsa-c-caebeammodel.htm.

[46] Unknwon. Solid (continuum) elements, 2022. URL https://abaqus-docs.mit.edu/2017/English/SIMACAEELMRefMap/simaelm-c-solidcont.htm.

[47] P. Wang, L. Wang, R. Chen, J. Xu, J. Xu, and M. Gao. Overview and outlook on railway track stiffness measurement. *Journal of Modern Transportation 2016 24:2*, 24(2):89–102, 5 2016. ISSN 2196-0577. doi: 10.1007/S40534-016-0104-8. URL https://link.springer.com/article/10.1007/s40534-016-0104-8.

[48] S. Witt. *The Influence of Under Sleeper Pads on Railway Track Dynamics*. PhD thesis, Linkoping University, 2008.

[49] L. A. Yang, . W. Powrie, and J. A. Priest. Dynamic Stress Analysis of a Ballasted Railway Track Bed during Train Passage. *Geotechnical and geoenvironmental engineering*, 2009. doi: 10.1061/ASCEGT.1943-5606.0000032.

[50] Z. Zhang and B. O. Andrawes. *FINITE ELEMENT ANALYSIS OF RAILWAY TRACK UNDER VEHICLE DYNAMIC IMPACT AND LONGITUDINAL LOADS*. PhD thesis, University of Illinois, 2015. URL https://core.ac.uk/download/pdf/158312233.pdf.

Appendix A Stadler FLIRT 75

A.1 Layout of Stadler FLIRT 75 train

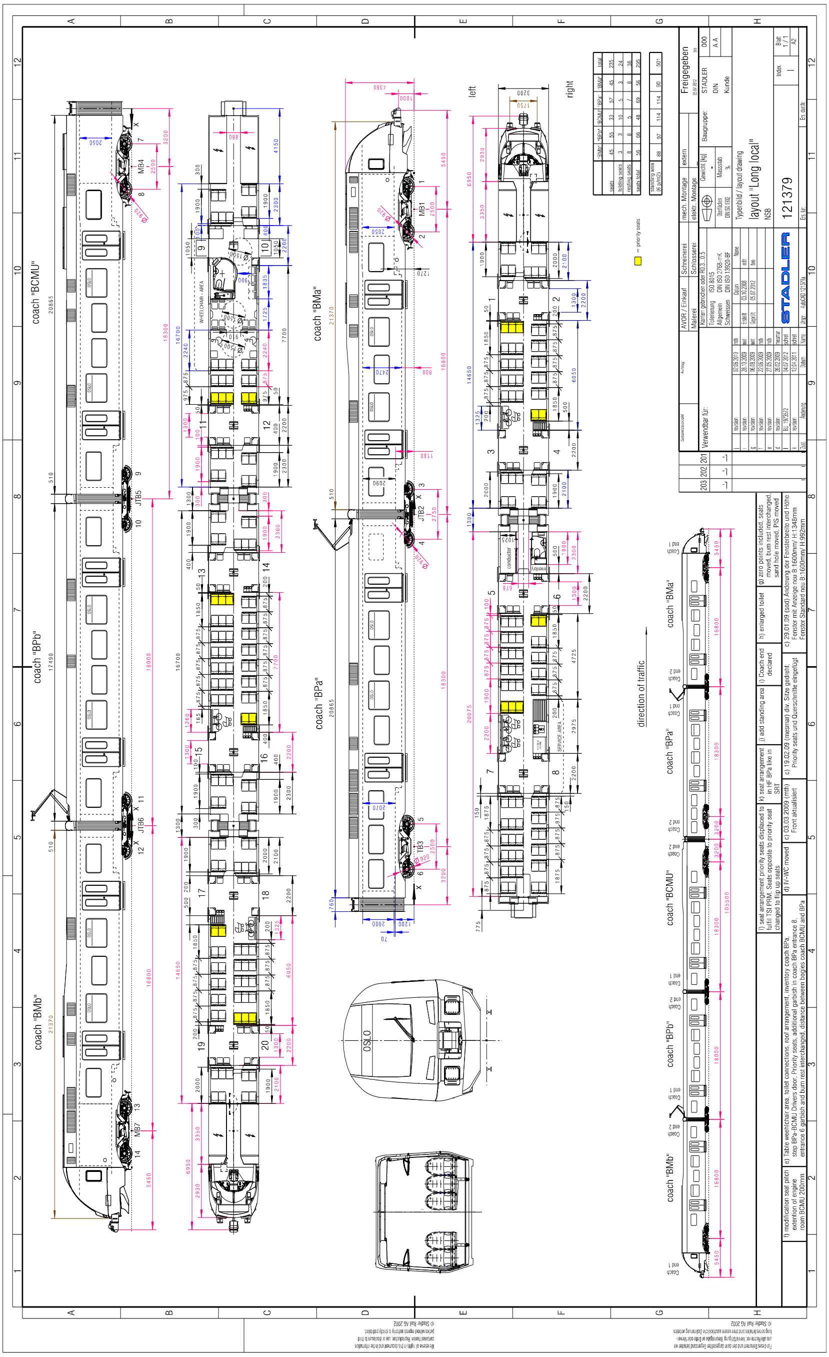
coach "BCMU"
coach "BPb"
coach "BMb"
coach "BMa"
coach "BPa"
left
right
direction of traffic
OSLO
layout "Long local"
NSB
STADLER
121379

A.2 Vehicle Dynamics of Stadler FLIRT 75 train

Tare, inflated air springs, STADLER Flirt

ref: Vehicle Dynamics- Verification Calculation Freigegeben

Bogie	Wheel load on inner Rail		Wheel load on outer Rail		Mean Wheel load		Axel load	
	[T]	[kN]	[T]	[kN]	[T]	[kN]	[T]	[kN]
MB7	9,57	93,9	8,63	84,7	9,10	89,3	18,21	178,6
JTB6	6,91	67,8	6,23	61,1	6,57	64,45	13,14	128,9
JTB5=JTB6?MB4?	6,91	67,8	6,23	61,1	6,57	64,45	13,14	128,9
MB4	8,61	84,5	7,78	76,3	8,20	80,4	16,39	160,8
TB3	6,51	63,9	6,13	60,1	6,32	62	12,64	124
JTB2=JTB6?	6,91	67,8	6,23	61,1	6,57	64,45	13,14	128,9
MB1=MB7?	9,57	93,9	8,63	84,7	9,10	89,3	18,21	178,6

Configuration	Mass total		Mean Load/axel		Max Axel load		Min Axel load	
	[T]	[kN]	[T]	[kN]	[T]	[kN]	[T]	[kN]
Flirt	209,72	2057,40	14,98034	146,9571	18,21	178,60	12,64	124,00

Gross, inflated air springs, STADLER Flirt

ref: Vehicle Dynamics- Verification Calculation Freigegeben

Bogie	Wheel load on inner Rail		Wheel load on outer Rail		Mean Wheel load		Axel load	
	[T]	[kN]	[T]	[kN]	[T]	[kN]	[T]	[kN]
MB7	10,80	105,9	9,67	94,9	10,23	100,4	20,47	200,8
JTB6	9,73	95,5	8,73	85,6	9,23	90,55	18,46	181,1
JTB5=JTB6?MB4?	9,73	95,5	8,73	85,6	9,23	90,55	18,46	181,1
MB4	10,14	99,5	9,16	89,9	9,65	94,7	19,31	189,4
TB3	8,41	82,5	7,89	77,4	8,15	79,95	16,30	159,9
JTB2=JTB6?	9,73	95,5	8,73	85,6	9,23	90,55	18,46	181,1
MB1=MB7?	10,80	105,9	9,67	94,9	10,23	100,4	20,47	200,8

Configuration	Mass total		Mean Load/axel		Max Axel load		Min Axel load	
	[T]	[kN]	[T]	[kN]	[T]	[kN]	[T]	[kN]
Flirt	263,85	2588,40	18,85	184,8857	20,47	200,80	16,30	159,90

Flirt EMU class 75 , type "long local"
Flirt EMU class 74 , type "short regional"
5 coaches: BMb, BPb, BCMU, BPa, BMa; Machine Room in BMb, BCMU, BMa
BMb, BMa : end cars
BPb, BCMU, BPa: middle cars
Motor Bogies: MB7, MB4, MB1
Jakobs trailer bogies: JTB6, JTB5, JTB2

Total number of axel 14

Appendix B Numerical Procedure of 2D Model

This section presents the track design and the mesh convergence study of a 2D model, as depict in Fig. B.1. The 2D model is used as benchmark for the validation of a 3D model.

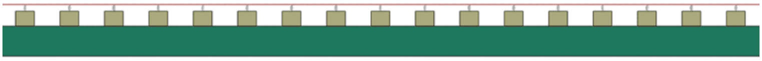

Fig. B.1: Profile of 2D model

B.1 Track Design

The model, shown in Fig. B.1, consists of rail, rail pad, sleepers and ballast. The rails are 40 m long and represented as a wire feature with the I-profile in Abaqus, and is a simplification of the 60E1 rail profile. Further, the rail is connected to the sleepers with spring and dashpots in parallel, which represents the rail pads. These rail pads are fixed to the sleepers with two dofs in the center of the sleeper. Symmetry boundary conditions are applied at each end of the rails, utilizing the ENCASTRE condition offered in Abaqus.

There are 64 sleepers in the model, placed with a sleeper distance of 0.6 m. The profile represents the cross section of a JBV60 sleeper, where the width is equal to 0.25 m and the height is 0.2 m. The sleepers are connected to the ballast with a surface-based tie connection. The ballast is a solid featured layer with a length of 40 m and height of 0.4 m. Since it is assumed that the track is placed in a tunnel and therefore confined to a stiff substructure, displacement boundary conditions are applied in the vertical direction of the ballast. This boundary condition constrains the ballast in the y-direction.

B.2 Mesh Convergence Study

This section presents the results of the mesh convergence study of the 2D model. The model is meshed structurally, and the applied load is a point load corresponding to maximum axle load of a Stadler FLIRT 75 train of 110.4 kN. It is measured as deflection versus number of elements.

From Fig. B.2, the rail show a clear tendency of reaching convergence, resulting in an element size of 0.01 yielding 8000 elements. Two types of elements are studied for the sleeper, and to avoid hour-glassing of the elements the most suitable element type is CPS4I. From Fig. B.3, the CPS4I converges around an element size of 0.015 yielding 221 elements. The ballast layer is studied with three types of elements, namely CPS4, CPS4I and CPS4R. The CPS4 and CPS4I element types showed the same tendency, while CPS4R induced increased deflections due to hour-glassing. Because the CPS4 and CPS4I act similarly, CPS4 is chosen due its lower CPU time of 15.3 seconds vs 22.4 seconds with CPS4I elements. Thus, from Fig. B.4, the chosen CPS4 elements has an element size of 0.02 yielding 81720 elements.

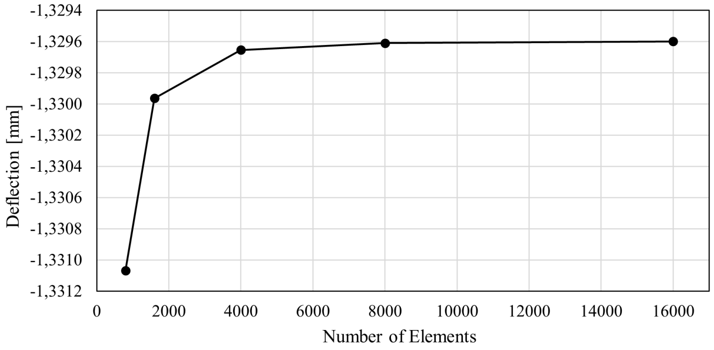

Fig. B.2: Mesh convergence study of rail from 2D model with B21 Timoshenko elements. The B21 elements is chosen due to allowable shear deformation of the beam.

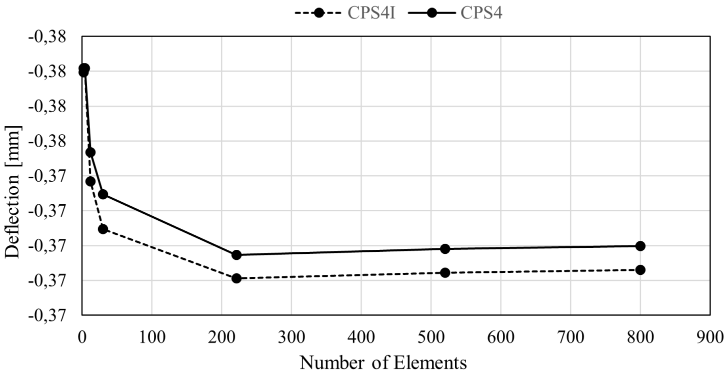

Fig. B.3: Mesh convergence study of sleeper from 2D model with CPS4I and CPS4 elements.

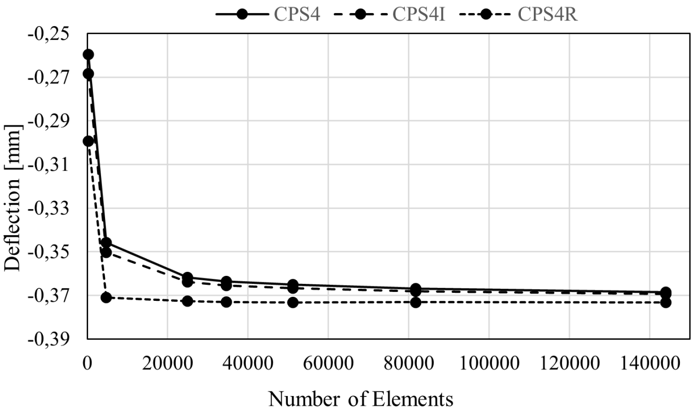

Fig. B.4: Mesh convergence study of ballast from 2D model with CPS4, CPS4I and CPS4R elements.

Appendix C Stress Distribution in the Ballast Layer

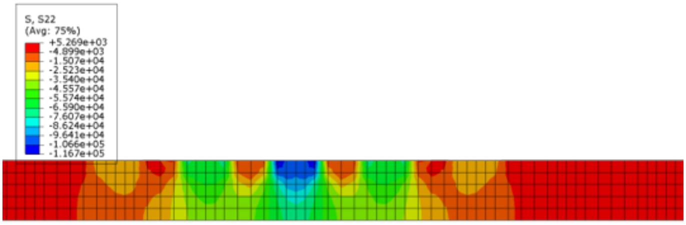

Fig. C.1: Stress distribution of the ballast layer without UBM. The dark blue areas show the highest measured compressive stress (located beneath a sleeper), while the highest measured tensile stress is presented in red areas (between sleepers and further away from the applied load).

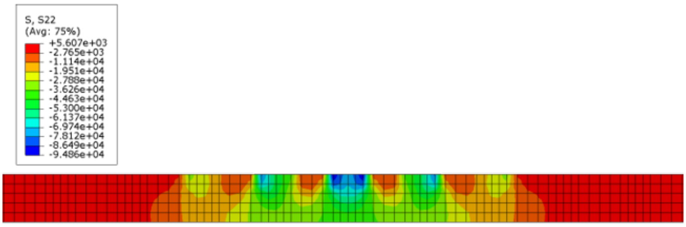

Fig. C.2: Stress distribution of the ballast layer with UBM1.

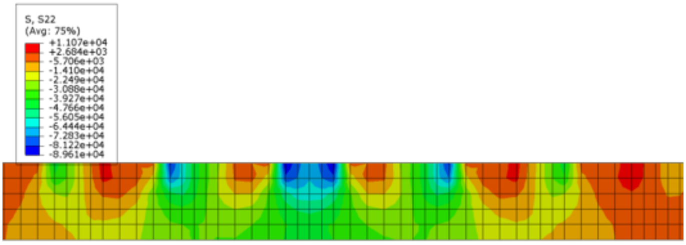

Fig. C.3: Stress distribution of the ballast layer with UBM5.

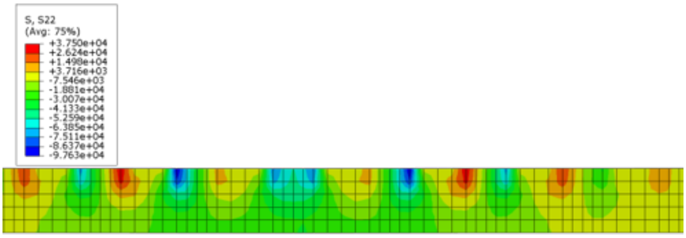

Fig. C.4: Stress distribution of the ballast layer with UBM6.

Appendix D Pressure Distribution in the Ballast Layer

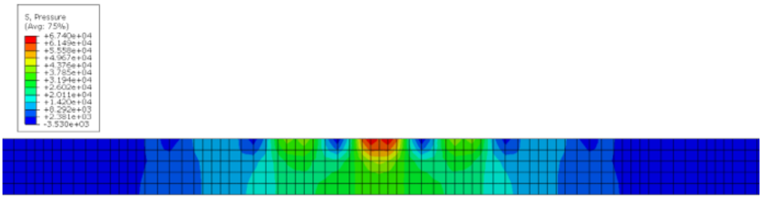

Fig. D.1: Pressure distribution of the ballast layer without UBM. The red areas show the highest measured pressure (located beneath a sleeper), while the lowest measured pressure is presented in blue areas (between sleepers and further away from the applied load).

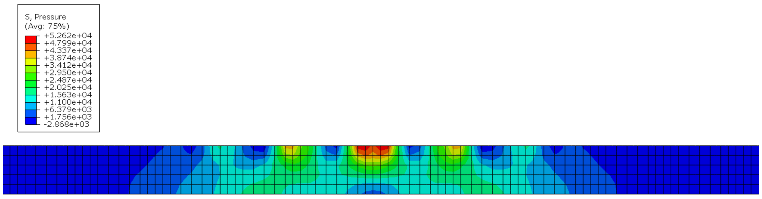

Fig. D.2: Pressure distribution of the ballast layer with UBM1

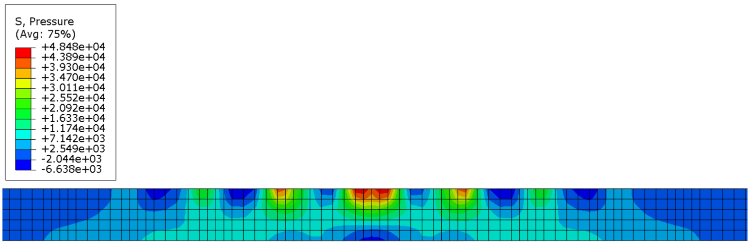

Fig. D.3: Pressure distribution of the ballast layer with UBM5

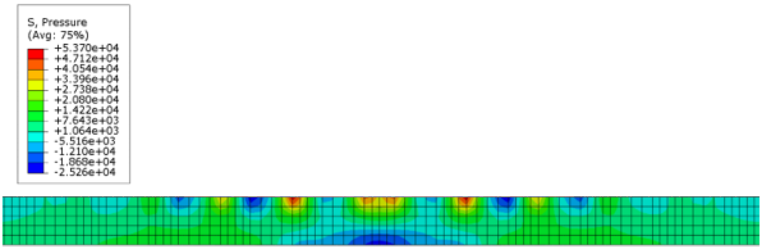

Fig. D.4: Pressure distribution of the ballast layer with UBM6

Appendix E Approach in Abaqus

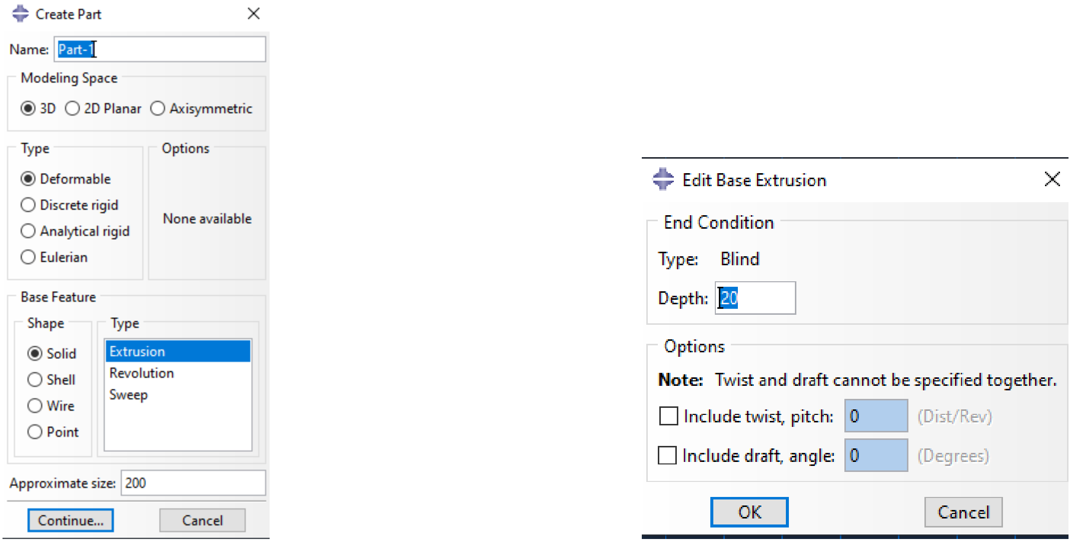

Create Part

Name: Part-1

Modeling Space: ● 3D ○ 2D Planar ○ Axisymmetric

Type: ● Deformable ○ Discrete rigid ○ Analytical rigid ○ Eulerian

Options: None available

Base Feature

Shape: ● Solid ○ Shell ○ Wire ○ Point

Type: Extrusion (selected), Revolution, Sweep

Approximate size: 200

Edit Base Extrusion

End Condition

Type: Blind

Depth: 20

Options

Note: Twist and draft cannot be specified together.

☐ Include twist, pitch: 0 (Dist/Rev)

☐ Include draft, angle: 0 (Degrees)

(a) Creating part. **(b)** Extruding part.

Fig. E.1: Creating Part by choosing modeling space, type of part and shape. Parts can be created through extrusion, revolution or by sweep. Base extrusion is the most common type of base feature, in which you choose the depth of the part.

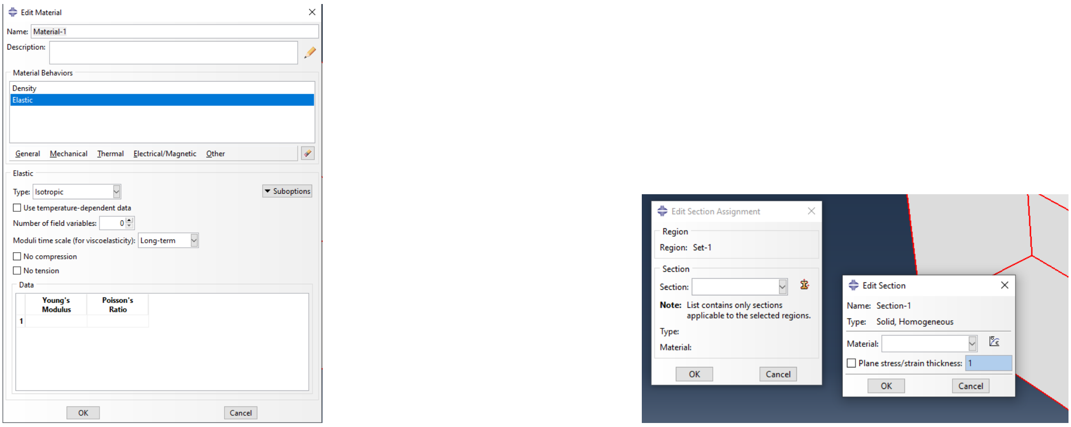

Edit Material

Name: Material-1

Description:

Material Behaviors: Density, Elastic (selected)

Elastic

Type: Isotropic

☐ Use temperature-dependent data

Number of field variables: 0

Moduli time scale (for viscoelasticity): Long-term

☐ No compression

☐ No tension

Data

	Young's Modulus	Poisson's Ratio
1		

Edit Section Assignment

Region

Region: Set-1

Section

Section:

Note: List contains only sections applicable to the selected regions.

Type:

Material:

Edit Section

Name: Section-1

Type: Solid, Homogeneous

Material:

☐ Plane stress/strain thickness: 1

(a) Creating material properties. **(b)** Assign material properties to part.

Fig. E.2: Once a part is created, it is assigned material properties. Abaqus offers a variety of properties to define the behavior of the part.

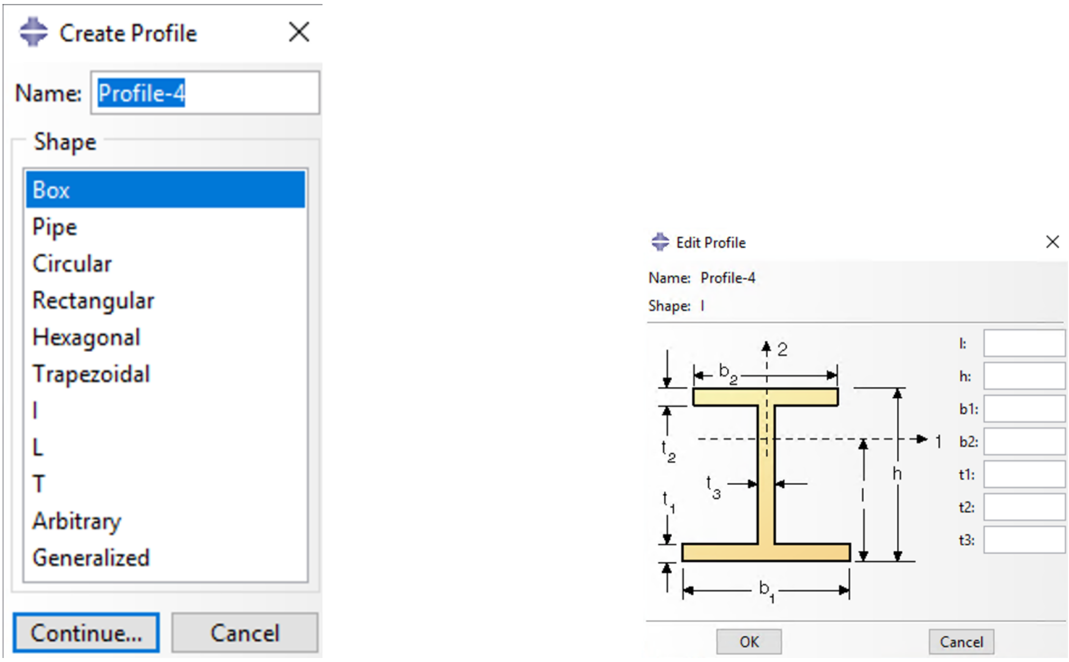

Create Profile

Name: Profile-4

Shape

- Box
- Pipe
- Circular
- Rectangular
- Hexagonal
- Trapezoidal
- I
- L
- T
- Arbitrary
- Generalized

Edit Profile

Name: Profile-4

Shape: I

(a) Creating profile.

(b) Editing profile.

Fig. E.3: If a wire or shell feature is created, it can be assigned a profile in Abaqus. There are various profiles available, such as the I-profile.

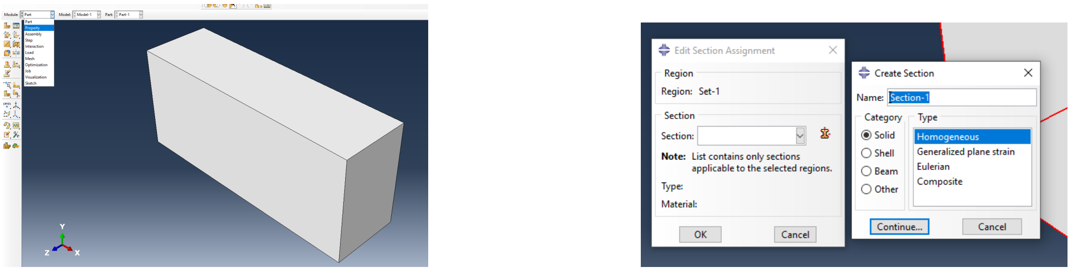

Edit Section Assignment

Region

Region: Set-1

Section

Section:

Note: List contains only sections applicable to the selected regions.

Type:

Material:

Create Section

Name: Section-1

Category

● Solid

○ Shell

○ Beam

○ Other

Type

- Homogeneous
- Generalized plane strain
- Eulerian
- Composite

(a) Property module

(b) Section Assignment

Fig. E.4: In the property module, a section is assigned to the part. It is possible to choose the type of section a part should have based on the available categories. In this module, the a profile and material properties can be assigned to the part.

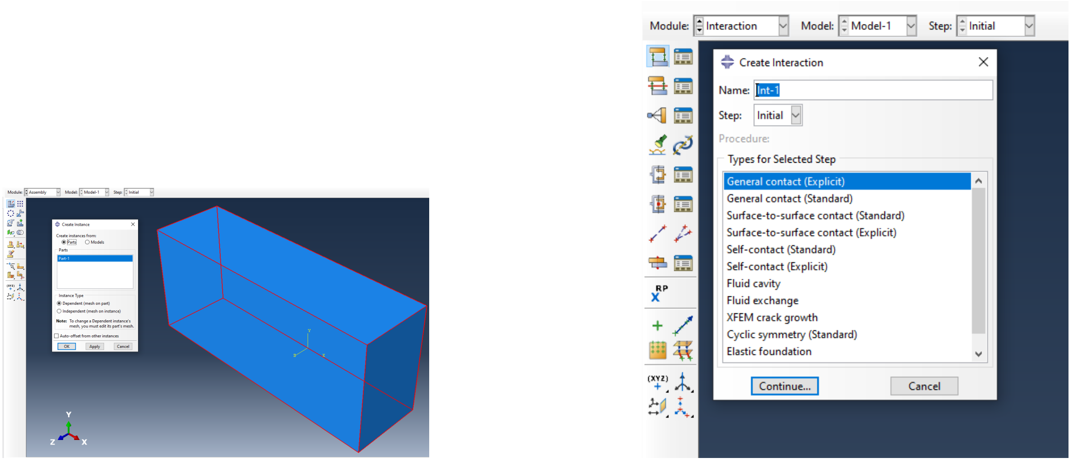
Module: Interaction Model: Model-1 Step: Initial

Create Interaction

Name: Int-1

Step: Initial

Procedure:
Types for Selected Step
General contact (Explicit)
General contact (Standard)
Surface-to-surface contact (Standard)
Surface-to-surface contact (Explicit)
Self-contact (Standard)
Self-contact (Explicit)
Fluid cavity
Fluid exchange
XFEM crack growth
Cyclic symmetry (Standard)
Elastic foundation
Continue...
Cancel
Y
Z
X

(a) Create instance to assembly. **(b)** Create interaction.

Fig. E.5: Various part can be created and assembled as instances in the assembly module. The same part can also be multiplied in this module. After assembly, it is possible to assign various interaction properties between each instance in the assembly in the interaction module.

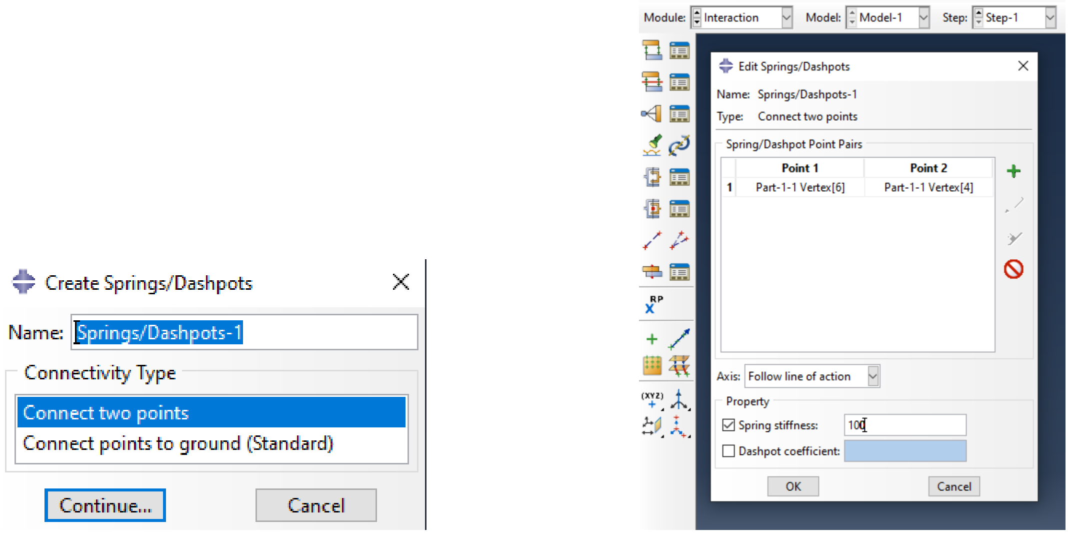
Create Springs/Dashpots

Name: Springs/Dashpots-1

Connectivity Type: Connect two points

Connect two points
Connect points to ground (Standard)
Continue...
Cancel

Module: Interaction Model: Model-1 Step: Step-1

Edit Springs/Dashpots

Name: Springs/Dashpots-1

Type: Connect two points

Spring/Dashpot Point Pairs

	Point 1	Point 2
1	Part-1-1 Vertex[6]	Part-1-1 Vertex[4]

Axis: Follow line of action

Property

☑ Spring stiffness: 100

☐ Dashpot coefficient:

OK
Cancel

(a) Create springs and dashpots. **(b)** Edit spring and dashpots.

Fig. E.6: Abaqus also offers to create springs and dashpots between instances in the assembly. This is done by connecting nodes from each part, and later choose the properties of the spring and dashpot.

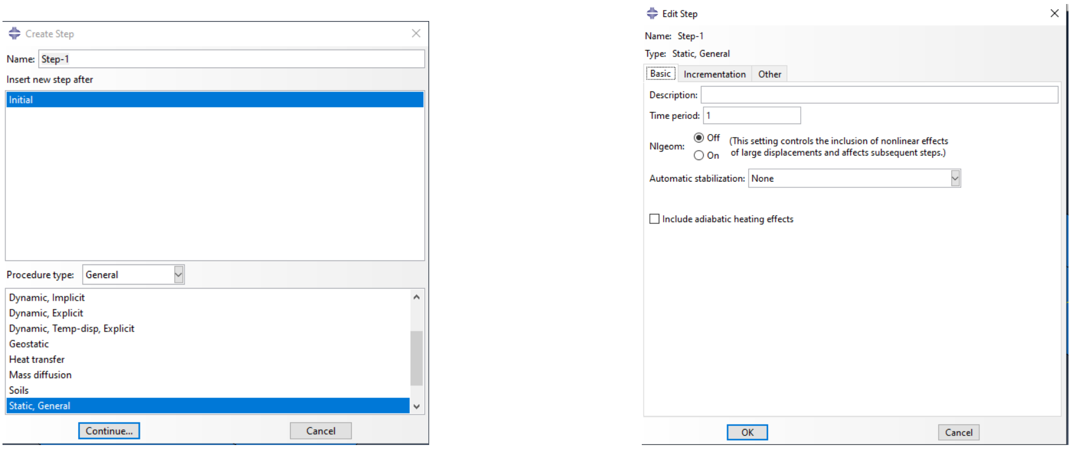
Create Step

Name: Step-1

Insert new step after: Initial

Procedure type: General

Static, General

Edit Step

Name: Step-1

Type: Static, General

Description:

Time period: 1

Nlgeom: ● Off ○ On (This setting controls the inclusion of nonlinear effects of large displacements and affects subsequent steps.)

Automatic stabilization: None

☐ Include adiabatic heating effects

Dynamic, Implicit
Dynamic, Explicit
Dynamic, Temp-disp, Explicit
Geostatic
Heat transfer
Mass diffusion
Soils
Static, General
Continue...
Cancel
Basic
Incrementation
Other
OK
Cancel

(a) Creating step

(b) Edit step basic

Fig. E.7: A step must be created in Abaqus to run various analyses. The step can further be edited by choosing time period and incrementation. This is also where the NGLEOM can be turned on or off based on nonlinear or linear analyses, respectively.

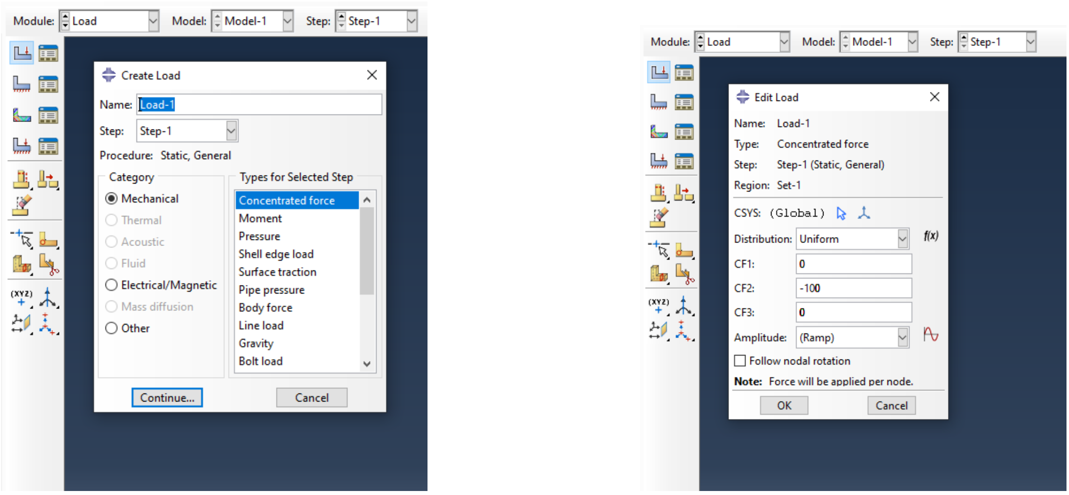
Module: Load Model: Model-1 Step: Step-1

Create Load

Name: Load-1

Step: Step-1

Procedure: Static, General

Category: ● Mechanical

Types for Selected Step: Concentrated force

Edit Load

Name: Load-1

Type: Concentrated force

Step: Step-1 (Static, General)

Region: Set-1

CSYS: (Global)

Distribution: Uniform

CF1: 0

CF2: -100

CF3: 0

Amplitude: (Ramp)

☐ Follow nodal rotation

Note: Force will be applied per node.

Category
Mechanical
Thermal
Acoustic
Fluid
Electrical/Magnetic
Mass diffusion
Other
Concentrated force
Moment
Pressure
Shell edge load
Surface traction
Pipe pressure
Body force
Line load
Gravity
Bolt load
Continue...
Cancel
(XYZ)
f(x)
OK
Cancel

(a) Creating load

(b) Edit Load

Fig. E.8: Abaqus offers various types of loading conditions, which is assigned to the created step. The load can be edited by choosing a custom amplitude and the magnitude of the load.

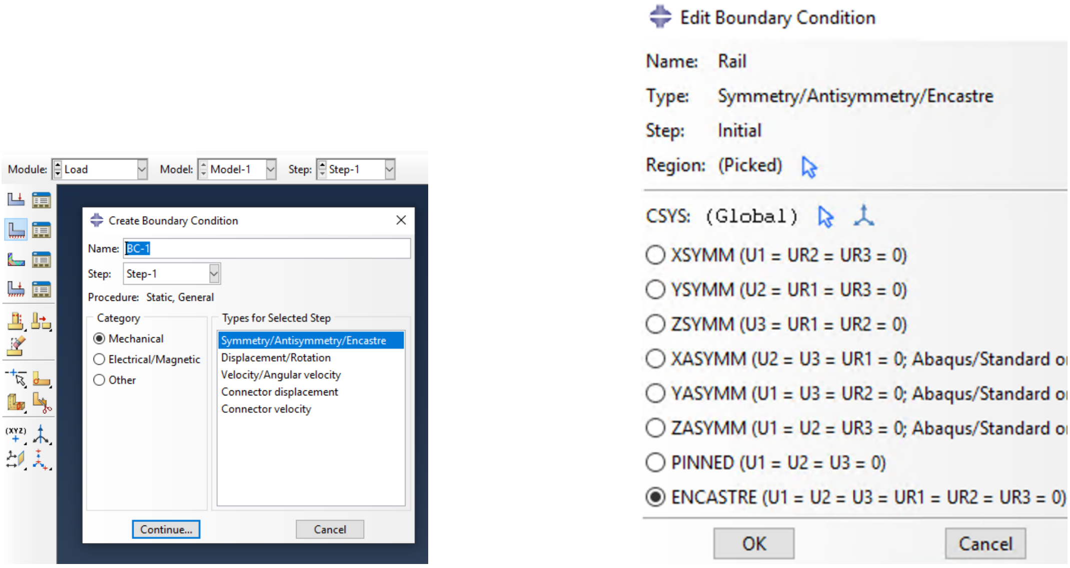

Module: Load Model: Model-1 Step: Step-1

Create Boundary Condition

Name: BC-1

Step: Step-1

Procedure: Static, General

Category: ● Mechanical ○ Electrical/Magnetic ○ Other

Types for Selected Step: Symmetry/Antisymmetry/Encastre (selected), Displacement/Rotation, Velocity/Angular velocity, Connector displacement, Connector velocity

Edit Boundary Condition

Name: Rail

Type: Symmetry/Antisymmetry/Encastre

Step: Initial

Region: (Picked)

CSYS: (Global)

○ XSYMM (U1 = UR2 = UR3 = 0)

○ YSYMM (U2 = UR1 = UR3 = 0)

○ ZSYMM (U3 = UR1 = UR2 = 0)

○ XASYMM (U2 = U3 = UR1 = 0; Abaqus/Standard o

○ YASYMM (U1 = U3 = UR2 = 0; Abaqus/Standard o

○ ZASYMM (U1 = U2 = UR3 = 0; Abaqus/Standard o

○ PINNED (U1 = U2 = U3 = 0)

● ENCASTRE (U1 = U2 = U3 = UR1 = UR2 = UR3 = 0)

(a) Create boundary condition

(b) Edit boundary condition

Fig. E.9: The instances in the assembly can be assigned boundary conditions, which can also vary depending on the selected step. Abaqus offers different categories and types with specified directions.

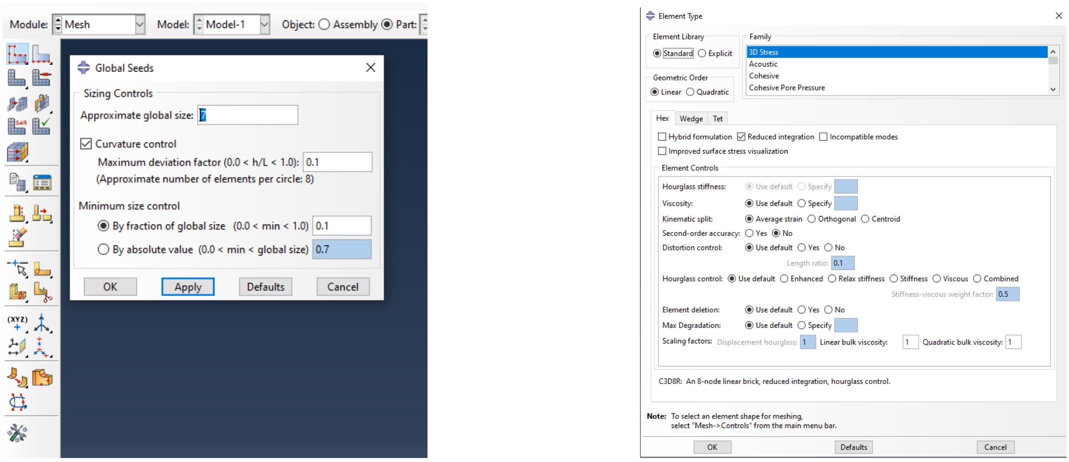

Module: Mesh Model: Model-1 Object: ○ Assembly ● Part:

Global Seeds

Sizing Controls

Approximate global size: 7

☑ Curvature control

Maximum deviation factor (0.0 < h/L < 1.0): 0.1

(Approximate number of elements per circle: 8)

Minimum size control

● By fraction of global size (0.0 < min < 1.0) 0.1

○ By absolute value (0.0 < min < global size) 0.7

Element Type

Element Library: ● Standard ○ Explicit

Geometric Order: ● Linear ○ Quadratic

Family: 3D Stress (selected), Acoustic, Cohesive, Cohesive Pore Pressure

Hex | Wedge | Tet

☐ Hybrid formulation ☑ Reduced integration ☐ Incompatible modes

☐ Improved surface stress visualization

Element Controls

Hourglass stiffness: ● Use default ○ Specify

Viscosity: ● Use default ○ Specify

Kinematic split: ● Average strain ○ Orthogonal ○ Centroid

Second-order accuracy: ○ Yes ● No

Distortion control: ● Use default ○ Yes ○ No

Length ratio: 0.1

Hourglass control: ● Use default ○ Enhanced ○ Relax stiffness ○ Stiffness ○ Viscous ○ Combined

Stiffness-viscous weight factor: 0.5

Element deletion: ● Use default ○ Yes ○ No

Max Degradation: ● Use default ○ Specify

Scaling factors: Displacement hourglass: 1 Linear bulk viscosity: 1 Quadratic bulk viscosity: 1

C3D8R: An 8-node linear brick, reduced integration, hourglass control.

Note: To select an element shape for meshing,
select "Mesh->Controls" from the main menu bar.

(a) Creating Mesh seeding

(b) Mesh Element Type

Fig. E.10: The whole assembly must be meshed before running the analyses, which is done in the mesh module. Global or local seeds can be assigned to each instance, and the element type is chosen based on the family. It can further by specified to have hexahedral, tetrahedral or wedge shaped elements.

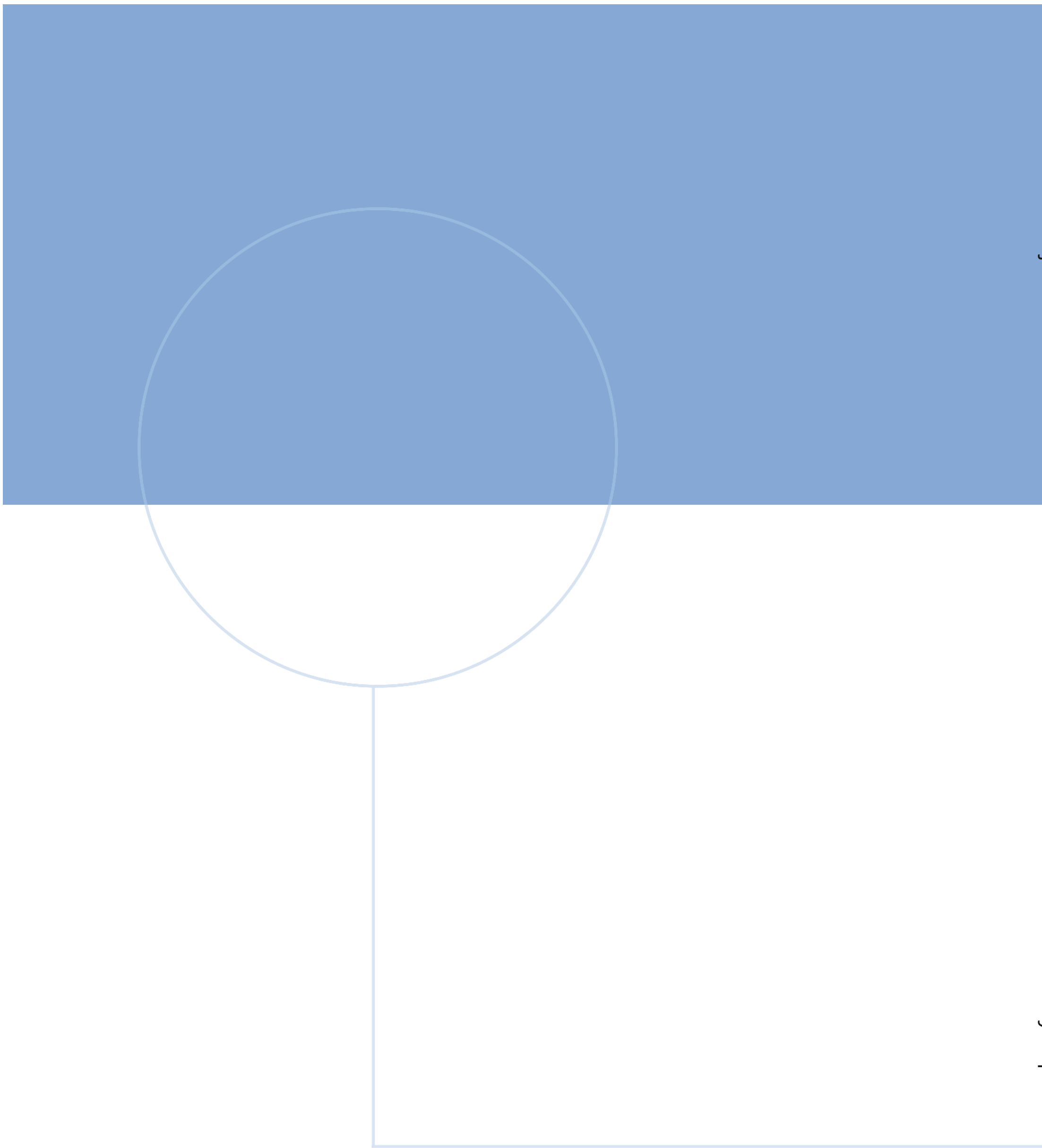

Karoline Kjøle Olsen

The Influence of Under Ballast Mats on Railway Superstructure

NTNU
Norwegian University of
Science and Technology